University of Insubria

PhD program in Chemical and Environmental Sciences

PhD thesis:

Physical and chemical aspects of the interaction of molecules with external surface and structural cavities of nanomaterials

Candidate: Marco Fabbiani

Tutor: Prof. Ettore Fois

Coordinator: Prof. Norberto Masciocchi

XXX cycle

2014 - 2017

Index

Introduction

The research work carried out during this PhD project has been aimed to the investigation of molecular surface events relevant for the catalytic formation, in mild conditions, of amide/peptide bonds from non-activated reagents adsorbed on nanomaterials. The formation of C-N bonds is among the topics of high interest in modern research in chemistry, addressing issues ranging from fine to prebiotic chemistry.

The implementation of this project required the selection of both catalyst and reactants.
As for the nanomaterials, the criteria of choice were simplicity, availability and low cost for possible future applications and, on the other hand, reasonable representativeness of minerals possibly present on the early Earth, and active as catalyst towards adsorbed organic molecules. On this basis the following nanoparticles of silica and titania are selected as well as a zeolite of the ZSM-10 type, with a MOZ framework. This latter material was intended as a porous host for future studies of the high pressure induced oligomerization of amino acids. This part of the work belongs to a very recent project, and then the work carried out in this respect in this PhD thesis is focused on the synthesis of zeolite particles with proper framework features.

The choice of reactants was driven, on one hand, on the suitability to be studied in depth by both experimental methods and theoretical modelling, and on the other hand, by the possibility to adsorb them on surfaces of nanomaterials from the vapour phase, i.e. in highly controlled conditions. Thus, the simplest carboxylic acid, HCOOH was selected, as well as two simple primary amines (methylamine and 1-pentanamine). One of the surface reaction investigated was the oligomerization of amino acids on the nanomaterials and for this glycine, alanine, histidine, serine were selected because of the possibility to adsorb them on catalyst via a chemical vapour deposition method.

In summary, in Chapter One, the study targeting the elucidation of the mechanism of the amide bond formation between non-activated carboxylic acids and amines at the surface of amorphous silica is reported. The results prepare the ground to address the occurrence of this reaction and of the oligomerization of amino acids (glycine and alanine) at the surface of α-quartz sub-micrometric particles (Chapter Two). The study of the C-N bond formation at the surface of titania nanoparticles is the object of Chapters Three to Five. In particular, Chapter Three is devoted to the investigation the structural requirements of sites expose at the surface of titania nanoparticles in order they can act as catalytic sites towards amino acid

oligomerization. In Chapter Four, insights on basic aspects of the interaction of formic acid and methylamine with the 101 anatase titania surface are presented. The possibility to prepare Ser-His dipeptides starting from non-activated amino acids by using titania nanoparticle as catalyst and the possible hydrolytic activity of the obtained peptides is the object of Chapter Five.

Finally, in Chapter Six, challenges, successes and problems still to be solved for and effective synthesis of large ZSM-10 particles, required for multi-techniques investigations, including single crystal X-ray diffraction.

Chapter One

Amide bond formation on silica

The mechanism of the amide bond formation between non-activated carboxylic acids and amines catalysed by the surface of silica is elucidated by combining spectroscopic measurements and quantum chemical simulations. Results suggest, for the first time, a plausible explanation of the catalytic role of silica in the reaction. Both experiment and theory identify very weakly interacting SiOH surface group pairs (*ca*. 5 Å apart) as key specific sites for hosting simultaneously ionic and neutral pairs of the reactants. An atomistic interpretation of the experiments indicates that this coexistence is crucial for the occurrence of the reaction, since the components of neutral pair are those undergoing the amidation reaction while the ionic pair directly participates in the final dehydration step. A kinetic model has been worked out indicating that, according to the calculated free energy barriers, the silica-catalysed amide formation is actually fast. Calculations, moreover, allow the identification of a metastable zwitterionic intermediate, similarly to that found in simulations for the peptide bond formation in the ribosome, in which one SiOH group and the ionic pair play the same role as that played by a sugar OH and a water molecule in the biological system

Motivations and challenges of this study

Formation of amides by condensation of amines and carboxylic acids is a subject of paramount interest from both industrial and fundamental perspectives. [1] In industry, the amide bond (AB) formation is a key reaction for pharmaceutical companies, by the adoption of powerful activating agents in the current synthetic routes. Unfortunately, they are both expensive and environmentally unfriendly with toxic/corrosive by-products and large quantities of waste. Thus, developing clean and low cost synthetic strategies with good atom economy is highly pursued. [2] Nevertheless, understanding the AB formation is also of fundamental importance, as it regulates the condensation of amino acids for the peptide synthesis, with profound implications in prebiotic chemistry and origin of life theories. Among the sequence of the organization events leading to the emergence of life, the peptide bond formation is still a not-well understood step, which is critical in the formation of the first biopolymers. Its complexity is partly because in highly diluted aqueous solutions, the reaction is thermodynamically disfavoured and the kinetics very slow, with reaction times of the order of several centuries. In

his seminal work, British biophysicist Bernal [3] proposed that mineral surfaces could have played a key role favouring the reaction, as they present proper surface sites that can adsorb and concentrate amino acids, as well as lower the activation barrier. More recently, Smith [4] suggested that minerals might have scavenged organic species for catalytic assembly into specific polymers protected from prompt hydrolysis and photochemical destruction. Along the same line, Orgel [5] proposed the "polymerization on the rocks" model, stating that oligomers can be elongated by repeated condensation cycles on the mineral surfaces and that the affinity of a surface for an oligomer increases with its length up to present an almost irreversible adsorption.

Based on these proposals, intensive investigations of the amide/peptide bond formation on mineral surfaces from experimental (*e.g.*, [6-8]) and computational (*e.g.*, [9-11]) viewpoints have been done and reviewed. [12-16] However, no full consensus in fundamental understanding on this topic has been reached because of, among other reasons, the diversity of the systems considered (namely, different amino acids and different minerals) and, from an experimental viewpoint, the diversity of the reaction procedures, so that results from different sources can hardly be compared. For instance, several spectroscopic studies carried out by Lambert and co-workers [17-19] indicate that glycine adsorbs, from an aqueous solution, on amorphous silica as a zwitterion and reacts at 160 °C to give diketopiperazine (DKP), the cyclic dimer product. In contrast, IR measurements of Martra et al., [8] envisaging surface adsorption from gas-phase reactants, identified formation of long oligomers from successive glycine feedings on amorphous silica at mild temperature. Obviously, rationalization of these results would provide relevant hints on the role of mineral surfaces in the amide/peptide bond formation, but this can also be a daunting task since, just for the limited case of silica surfaces, they present a sheer variety of structures and pre-reaction treatments.

Within this context, an interesting hypothesis to overcome the "water problem" (i.e., in water solution the reaction is disfavoured) is that based on fluctuating environments on the prebiotic Earth. That is, daily fluctuations of temperature and seasonal fluctuations of humidity, which readily occurs under natural conditions, could have led to cycles of drying and rewetting so that, condensation reactions become possible during the drying cycle of a wetting/drying cycle. Experimental evidences support this theory. Lahav et al. [6] showed that systems consisting of clay, water, and amino acids subjected to cyclic variations in temperature and water content produced long oligopeptides in higher yields. Moreover, they also demonstrated that water variations are more important than temperature fluctuations suggesting that the occurrence of drying is crucial. Along this line,

Muller and Schulze-Makuch showed that macroscopic cycles, including drying, might drive a chemical reaction that would be endergonic in isolation. [20]
The aim of the work is to provide a deep understanding of the AB formation mechanism on silica surfaces and determining the actual role of the surfaces in the process, focusing on molecular phenomena possibly occurring during the drying step of wetting/drying cycles. This has been done by synergistically combining IR spectroscopy measurements with quantum chemical calculations. Here, to avoid the progressive polymerization of glycine and to focus only on the specific AB condensation reaction, in the experiments, glycine is replaced by formic acid and methylamine or 1-pentanamine. Here, AEROSIL®OX50, a highly pure pyrogenic amorphous SiO_2 powder, was used. Silica of the AEROSIL® type were used in several studies on the abiotic polymerisation of amino acids. [8, 13, 19] In particular, related to the formation of a nucleoside (adenosine monophosphate) and one of its molecular precursor under prebiotic conditions. [21] AEROSIL®OX50 was selected for the purpose of this work because of its specific surface area (SSA) of *ca*. 50 m^2/g. This SSA is, on one side, high enough to obtain clearly detectable IR signals of surface species, while on the other side, low enough to be unaffected by calcination up to 973 K (*vide infra*). Thus, the removal of surface silanols without changes of the texture of material is attained.

Evolution of surface silanol population along step-wise thermal treatments

A key point of the experimental work was the setup of proper thermal treatment conditions, which allow a selective, progressive removal of distinct families of silanols (SiOH) differing in strength of mutual interactions because of the different inter-silanol distance. Furthermore, thermally treated silica samples should not have surface strained siloxane bridges. Such bridges are known to be reactive with amine and carboxylic acids, as well as H_2O molecules, [22] all of them being species involved in our reaction of interest. These targets were successfully attained by calcination in static air at 723 K and then at 973 K (details on the heating rate and duration of isothermal treatments are available in the Methods section). As anticipated above, the SSA remained unchanged, even after calcination at the highest temperature (see Table 1).

Table 1. Specific surface area (SSA_{BET}) of silica samples in the pristine form and after calcination in air at 723 and 973 K. The accuracy of the measurement is *ca* ± 5%.

Sample	SSA_{BET} ($m^2\ g^{-1}$)
Pristine	47 ± 3
Calcined in air at 723 K	47 ± 3
Calcined in air at 973 K	49 ± 3

For the sake of completeness, we also assessed the invariance of both XRD pattern and Raman spectrum (see Figure 1).

Through IR spectroscopy in a controlled atmosphere the effect of the thermal treatments on surface silanols is monitored. Evidence of the irreversibility of the removal of silanols towards subsequent contact with water is depicted in Figure 2. The νOH spectrum of pristine, thermally untreated silica outgassed at beam temperature (hereafter b.t.) appears composed by (Figure 2A, curve a) a narrow peak at 3747 cm^{-1} due to "isolated" silanols (*i.e.*, not involved in any inter-silanol interaction), and by a complex and broad absorption, asymmetric over the low frequency side, due to interacting surface silanols and intraglobular Si-OH (*vide infra)*. [23] The pattern in the 2100-1500 range is due to combination (1995 and 1870 cm^{-1}) and overtone (1630 cm^{-1}) modes of the silica bulk network, [23] and was used to normalise the spectra of different samples with respect to the same silica amount. A H/D isotopic exchange was carried out by replicating D_2O vapour (20 mbar) admission /outgassing steps until invariance of the spectra (Figure 2A, curve b).

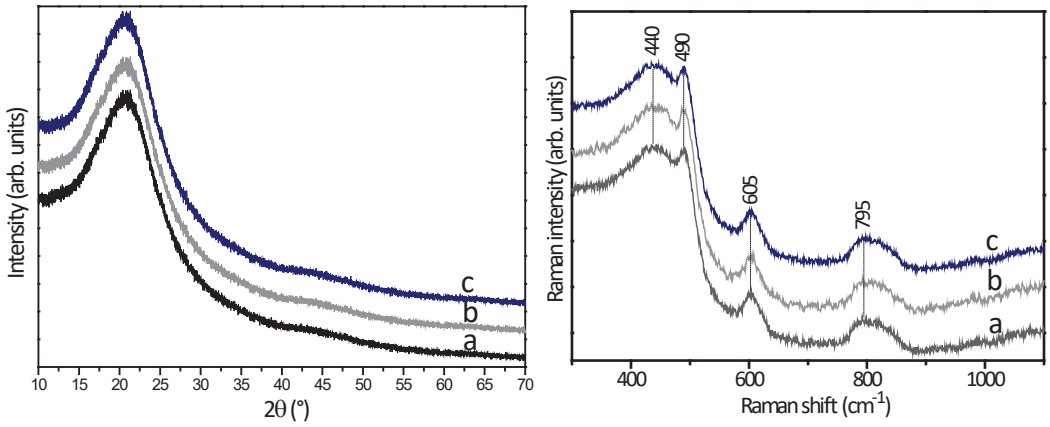

Figure 1. XRD patterns (left panel) and Raman spectra (right panel) of silica samples: a) in the pristine form; b) calcined at 723 K; c) calcined at 973 K

In Figure 1, the XRD patterns and Raman spectra of the SiO_2 powder in the pristine form (curves a) and calcined at 723 and 973 K (curves b and c. respectively) are typical of amorphous silica [24]. Moreover, no significant changes occurred in both type of data in dependence on the thermal treatment, indicating that calcination did not affect the bulk structure of silica nanoparticles.

Table 1. Assignment of the Raman signals for SiO_2.

Raman shift (cm^{-1})	Assignment [25]
440	δSi-O-Si
490	breathing vibration mode of 4 member rings
605	breathing vibration mode of 3 member rings
795	longitudinal and transverse silica network vibrations

Typically, 5 cycles ensured a full exchange. Surface silanols, now in the Si-OD form, produced the νOD pattern in the 2800-2100 cm^{-1} range, whereas the νOH pattern in the 3750-3000 cm^{-1} range monitors the presence of intra-globular Si-OH, which are not accessible to H/D exchange. [23] Noteworthy, evidence of the complete desorption of water molecules from the silica surface by outgassing at b.t. is provided by absence of changes in the 1700-1600 cm^{-1}, where the δH_2O signal, if present, should disappear in favour of the downshifted δD_2O one. As expected, a D/H isotopic back exchange by contact with 20 mbar of H_2O vapour fully restored the initial spectrum of the pristine silica sample outgassed at b.t. (Figure 2A, curve c).

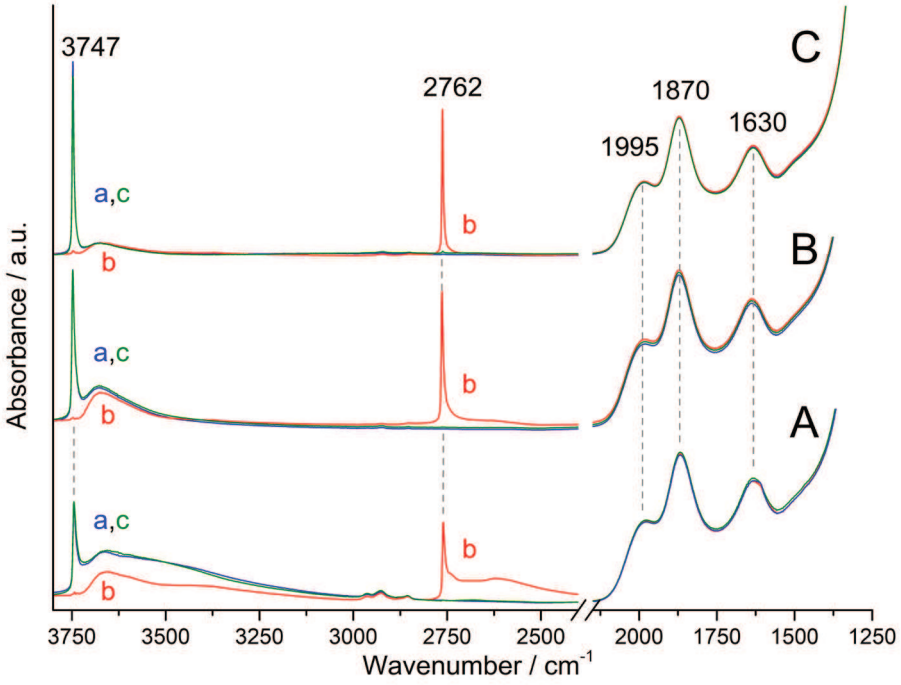

Figure 2. IR spectra of SiO_2 samples: A) in pristine form; B) calcined at 723 K; C) calcined at 973 K. In each section: a) sample outgassed at b.t.; b) after isotopic H/D exchange by admission (20 mbar)/outgassing at b.t. of D_2O vapour; c) after isotopic D/H back exchange, by admission (20 mbar)/outgassing at b.t. of H_2O vapour.

Equivalent sets of spectra were acquired for silica samples calcined at 723 K (Figure 2B) and at 973 K (Figure 2C). In the following, the effect of thermal treatments on surface silanols is described. It is worth mentioning that also for these cases the final contact with H_2O vapour and subsequent outgassing restored the spectra obtained after the initial outgassing at b.t (curves a and c in Figure 2B and C), thus witnessing for the absence of reactive surface strained siloxane bridges. Moreover, the H/D exchange reveals that thermal treatment also promoted the condensation between intra-globular silanols (curves b in Figure 2B and C).

For each sample, the subtraction of the νOH pattern of intra-globular silanols (curves b) from that obtained after initial outgassing at b.t (curves a) allows to obtain the νOH spectral profile due to surface Si-OH only. The results are shown in Figure 3A. For the pristine SiO_2 (curve a), the νOH pattern of surface silanols is constituted by: i) the narrow peak at 3747 cm^{-1} due to isolated SiOH, asymmetric on the low frequency side, ii) a shoulder at 3720 cm^{-1} (SiOH terminating chains of interacting

silanols), iii) an ill resolved sub-band at 3665 cm^{-1} (weakly H-bonded silanols), and iv) a broad component with maximum at 3530 cm^{-1} (asymmetric down to 3000 cm^{-1}) due to H-bonded SiOH. [23] ν(OH) signals below 3735 cm^{-1} were almost depleted by thermal treatment at 723 K (Figure 3A, curve b), monitoring the removal of the overwhelming part of H-bonded silanols. This depletion is accompanied by an increase in intensity of the peak at 3747 cm^{-1}, still asymmetric on the low frequency side, due to the additional contribution of silanols that remained isolated after removal of their interacting partner(s). By increasing the temperature treatment up to 973 K, condensation of silanols absorbing below *ca.* 3730 cm^{-1} appeared completed, and the peak at 3747 cm^{-1} becomes narrower and more symmetric and intense (for the same reason indicated above). A clearer and more detailed view of the evolution of the surface silanols population, as monitored through the ν(OH) pattern, is provided by the difference between the spectra of the silica before and after each step of the thermal treatment (Figure 3B). The correctness and effectiveness of this spectral subtraction is guaranteed by the possibility to normalise the original spectra with respect to the mass of silica and the constancy on the SSA. The difference between the spectra of the sample calcined at 723 K and the pristine one (Figure 3B, curve b-a) results in a broad negative band, with the high frequency onset at 3735 cm^{-1}, constituted by the overlapping of several components, located at lower frequency as the strength of inter-silanols interaction (likely of the H-bond type) increases. The difference between the spectra of samples calcined at 973 or at 723 K (Figure 3B, curve c-b) provides evidence that the increase of the calcination temperature mainly results in the removal of very weakly interacting silanols, characterized by a νOH of 3742 cm^{-1} (minimum of the negative part of the difference spectrum). In both difference spectra, the sharp peak at 3747 cm^{-1} is due to the newly formed isolated silanols. The much larger integrated intensity of the negative band in curve b-a with respect to the negative part of curve c-b does not correspond to the ratio of amounts of silanols removed by calcining at a different temperature. The same occurs for the positive sharp peak.

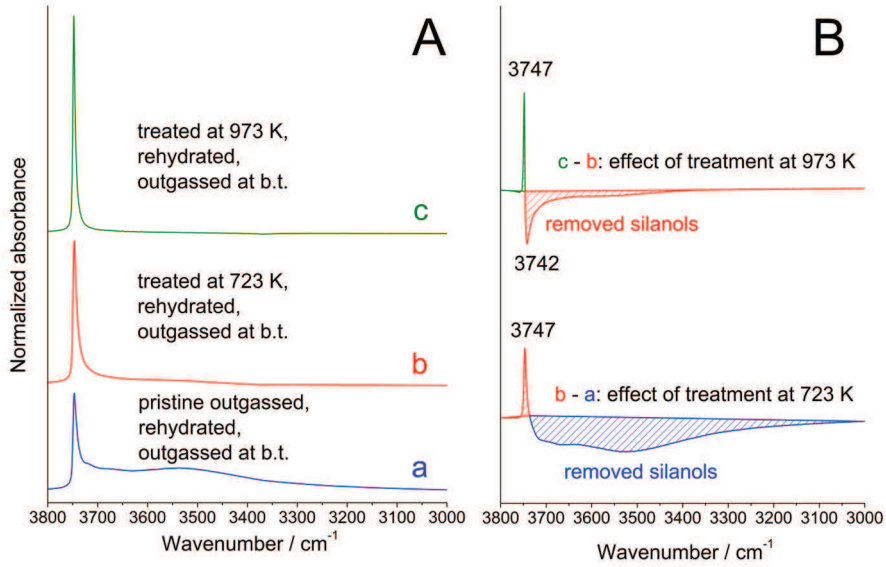

Figure 3. IR spectra of SiO_2 samples with different surface SiOH populations (spectra collected after outgassing at b.t.). Data in section A are the result of the subtraction of the νOH pattern due to intraglobular silanols (inaccessible to reactants; curves b in Fig. 1) from the total νOH pattern (surface + intraglobular; curves a in Fig. 1). a) pristine SiO_2; b) after calcination at 723 K; c) after calcination at 973 K. The differences between pairs of spectra in panel A are depicted in panel B, showing the decrease and increase in intensity of νOH components due to surface Si-OH removed (negative signals) or affected by a change in intersilanol interaction (positive signal) as a consequence of the thermal treatments. Curve b-a) effect calcination at 732 K. Curve c-b) effect of the subsequent calcination at 973 K.

In fact, the integrated intensity of OH stretching absorption increases linearly as the νOH decreases, with a factor of ≈ 4 passing from H-bonded silanols absorbing at *ca.* 3530 cm^{-1} to very weakly interacting and isolated silanols absorbing in the 3730-3750 cm^{-1} range. [26]

Interaction of reactants with the silica surface

Samples of thermally untreated silica were contacted in separated experiments with methylamine (MA) and formic acid (FA) vapours. Both molecules appeared to be reversibly adsorbed under outgassing at b.t. are reported in Figure 4. Here, MA and FA were dosed on samples until disappearance of the peak at 3747 cm^{-1} due to isolated silanols (curve b). The coincidence between spectra obtained after initial outgassing (curves a) and after outgassing of molecules (curve c) admitted on the silica samples indicated that the interaction between MA or FA and the SiO_2 surface was fully reversible in the given conditions.

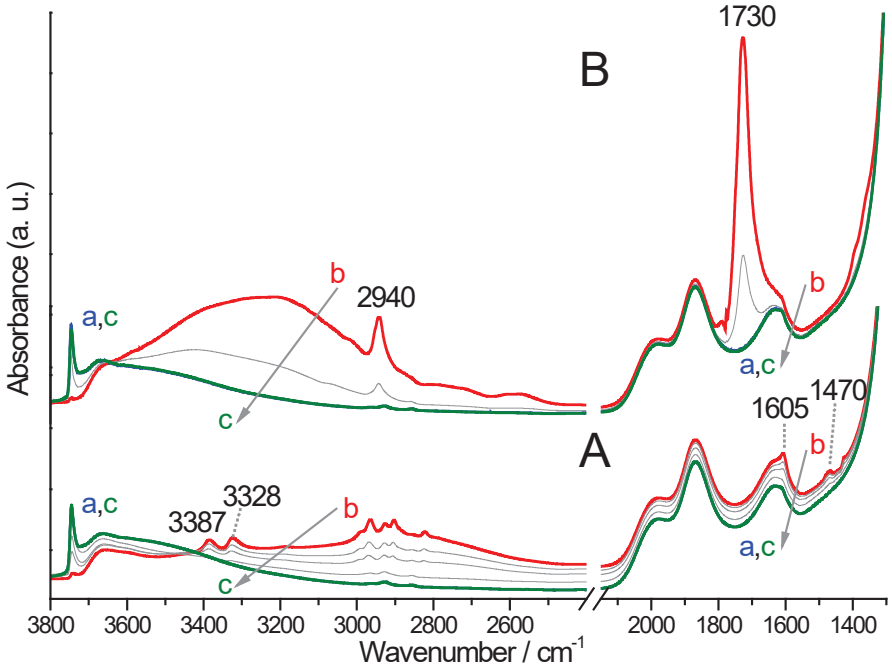

Figure 4. Infrared spectra of pristine silica samples outgassed at b.t. and then contacted with methylamine (MA) (Section A) or formic acid (FA) (Section B). Spectra in both sections are as follows: a) sample outgassed at b.t.; b) in contact with MA or FA; c) after subsequent outgassing until invariance of spectra, grey curves show intermediates steps of outgassing.

The assignment of the bands due adsorbed MA (section A) and FA (section B) is reported in the Table 2. As expected, the adsorption of FA occurred in the molecular form, as indicated by the presence of the νC=O signal.

These results were considered representative of the adsorptive behaviour towards these molecules also of thermally treated SiO_2 samples, carrying at their surface fractions of the silanol population present on the pristine silica (and without the additional presence of reactive strained siloxane bridges, as commented above).

Table 2. Assignment of the bands due to adsorbed MA and FA on SiO_2.

Adsorbed methylamine		Adsorbed formic acid	
position (cm^{-1})	assignment	position (cm^{-1})	assignment
3387	$\nu_{asym}NH_2$	3600-2600*	ν_{OH} (H-bonded)
3320	$\nu_{sym}NH_2$	2940	νCH
3000-2800	-CH_3 stretching	1730	νC=O
1605	δNH_2		
1470	$\delta_{asym}CH_3$		

* band overlapped to the ν_{OH} absorption due to H-bonded surface silanols

Thus, the AB reaction between MA and FA was carried out by dosing MA at a small pressure on SiO_2 samples and then admitting FA vapours in the IR cell, used also as a batch reactor. This sequence of admission; *i.e.*, "MA then FA", was preferred with respect to the reverse one because of the similarity with the reaction procedure used with 1-pentanamine (*vide infra*). The effect of the sequential admission of reactants on the thermally untreated SiO_2 samples, as monitored by IR spectroscopy, is displayed in Figure 5. As mentioned, MA was dosed first in an amount low enough to prevent the occupancy of all surface silanols by amine molecules. This ensures to have adsorption sites available for the interaction with FA. Since the OH stretching frequency of silanols is downshifted as a consequence of the interaction with adsorbates, it was possible to achieve this coverage condition by targeting a partial decrease in intensity of the νOH pattern of the surface silanols when admitting MA (curves a and b). This decrease is accompanied by the appearance of a broad adsorption spread over the 3300-2400 cm^{-1} range, indicating that SiOH behaves as a donor of a strong H-bond towards adsorbed amine molecules, which produce signals at 3387 and 3328 cm^{-1} (asym and sym νNH_2, respectively), 3000-2900 cm^{-1} (-CH_3 stretchings), 1605 cm^{-1} (δNH_2) and 1470 cm^{-1} (asym δCH_3). [27]
Increasing amounts of FA were then admitted on the silica sample in contact with MA, until depletion of the νNH_2 stretching signals (curves b→g). This resulted in a further decrease in intensity of the νOH pattern of unperturbed surface silanols. Moreover, it lead to an increase in intensity of the broad absorption of Si-OH involved in strong H-bonding and in the appearance of bands due to formate species at 2815 cm^{-1} (νCH) and 1575 cm^{-1} (asym νCOO^-), [28] and to methyl ammonium at *ca*. 3300 cm^{-1} (–NH_3^+ stretchings) and 1620 cm^{-1} (mainly asym δNH_3^+, since the sym δNH_3^+ is likely contributing to the low frequency side of the asym νCOO^- band). [27]

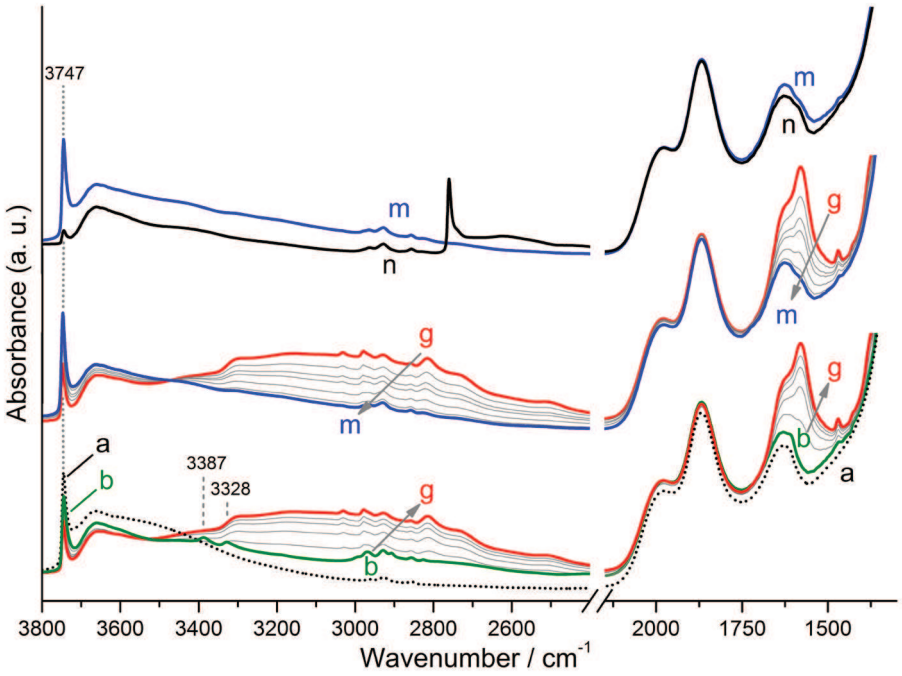

Figure 5. Infrared spectra of pristine SiO_2 outgassed at b.t. and subsequently contacted with methylamine (MA) and formic acid (FA): a) dotted black line, sample outgassed at b.t.; b) after admission of MA until having the intensity of the peak at 3747 cm^{-1}, due to isolated silanols; b→g) after admission of FA until depletion of νNH_2 signals at 3387 and 3328 cm^{-1} (grey curves show intermediate amounts of FA); g→m) after subsequent outgassing at b.t. until invariance of spectra (grey curves show intermediates steps of outgassing); n) after D_2O admission (20 mbar)-outgassing at b.t. until spectral invariance.

Noteworthy, the asym δCH_3 signal of MA molecules also increases in intensity, monitoring an additional adsorption of amine molecules. As indicated above, the IR cell is used as a batch reactor, with the inlet for reactants on the top and the sample at the bottom as indicated in Methods section.

To allow the second reactant to enter in the cell, FA vapour is dosed at a slightly higher pressure with respect to the already present MA. Apparently, the inter-diffusion of the two vapours within the cell is not instantaneously homogeneous, and the admission of FA results also in some compression of MA vapour towards the sample. The reaction mixture is then outgassed until invariance of spectra: the signals related to adsorbed formates and methyl ammonium strongly decrease in intensity, and the original νOH profile of surface silanols is largely restored (curves g→m). Amide molecules, if formed, should produce a $\nu(C=O)$ band in the 1700-1600 cm^{-1} range, where also the asym δNH_3^+ signal of methyl ammonium possibly remained adsorbed and the δH_2O signal of water molecules resulting from

amidation falls. Thus, the $-NH_3^+$ and H_2O spectral contributions are downshifted by an H/D exchange carried out by admission/outgassing at b.t. of D_2O. It is anticipated that the difference between the obtained spectrum (curve n) and that of the bare silica sample initially outgassed at b.t. (curve a) is calculated in order to better recognise bands due to reaction products that remained adsorbed on the silica surface. The sequential adsorption of MA and FA, with final H/D exchange, is carried out also on silica samples thermally treated at 723 and 973 K as reported in Figure 6 and Figure 7, respectively.

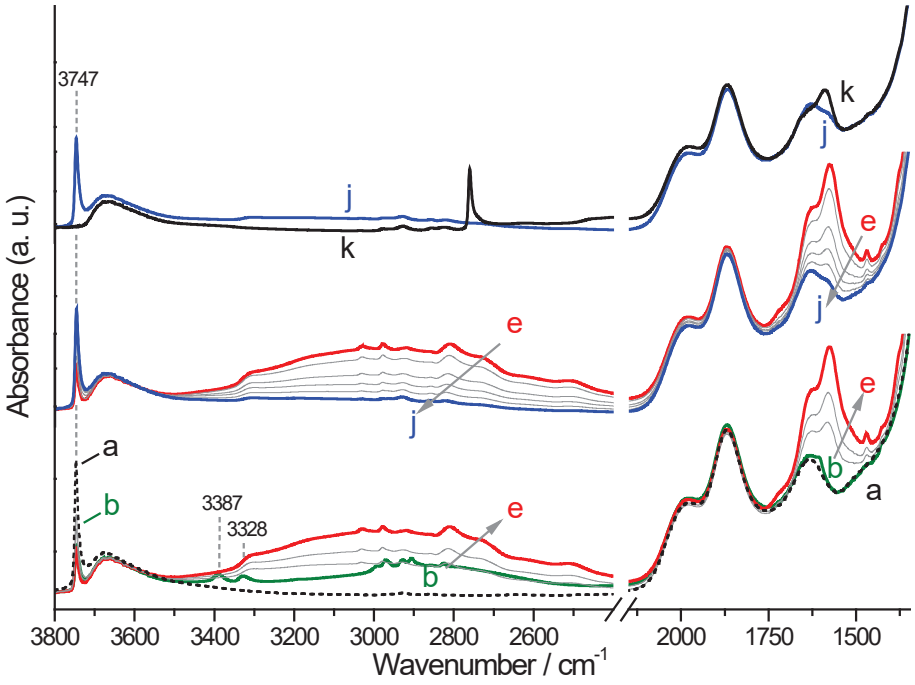

Figure 6. Infrared spectra of amorphous silica sample treated at 723 K in air, then outgassed at b.t. and subsequently contacted with methylamine (MA) and formic acid (FA): a) dotted black line, sample outgassed at b.t.; b) after admission of MA until halving the intensity of the peak at 3747 cm^{-1}, due to isolated silanols; c-e) after admission of FA until depletion of νNH_2 signals at 3387 and 3328 cm^{-1}; f-j) after subsequent outgassing at b.t. until invariance of spectra; k) after D_2O admission (20 mbar)/outgassing at b.t. until invariance of spectra.

MA and FA are considered as reactants for AB formation because of the possibility to simplify quantum chemical calculations aimed to provide an atomistic interpretation of experiments (see below). Nevertheless, the expected product of their condensation reaction, methylformamide, was found to be poorly stable against hydrolysis (as from HR-MS analysis of an aqueous solution of N-MFA, see Figure A1 panel A in the Appendix).

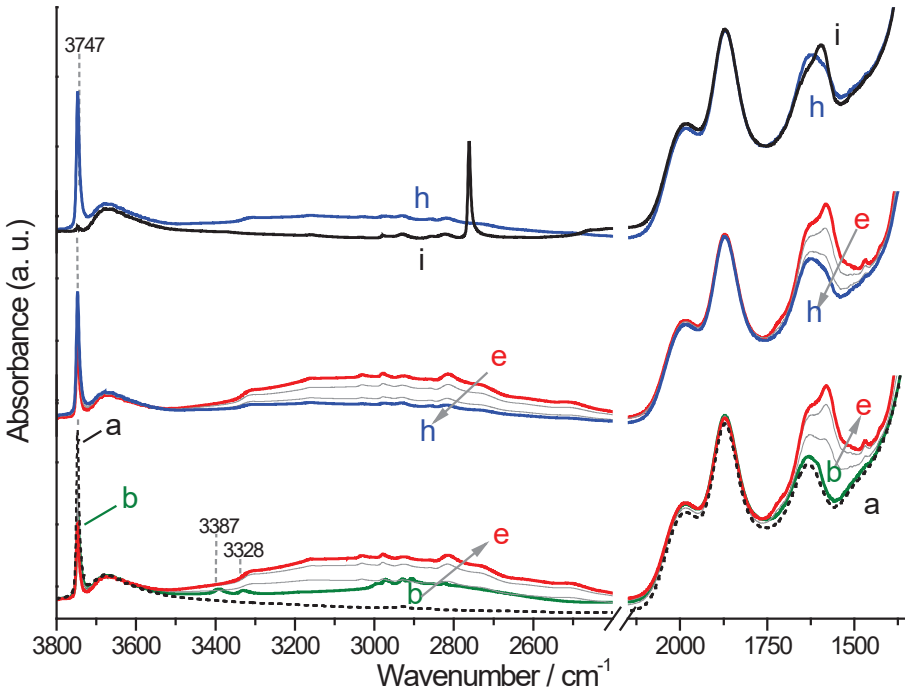

Figure 7. Infrared spectra of amorphous silica sample treated at 973 K in air, then outgassed at b.t. and subsequently contacted with methylamine (MA) and formic acid (FA): a) dotted black line, sample outgassed at b.t.; b) after admission of MA until halving the intensity of the peak at 3747 cm^{-1}, due to isolated silanols; c-e) after admission of FA until depletion of νNH_2 signals at 3387 and 3328 cm^{-1}; f-h) after subsequent outgassing at b.t. until invariance of spectra; i) after D_2O admission (20 mbar)/outgassing at b.t. until invariance of spectra.

Thus, the final step of the experimental procedure described above, requiring the contact with D_2O of the species remained on the silica surface, could result also in a partial hydrolysis of methyl formamide possibly formed by reaction between adsorbed MA and FA. For this reason, 1-pentanamine (PA), with a longer alkyl chain likely protecting the amide-derivative from hydrolysis (see Figure A1 panel B in the Appendix) is used. Moreover, the larger contributions of dispersive interactions between PA and the silica surface results in the resistance to outgassing at b.t. of a non- negligible fraction of adsorbed PA molecules (Figure 8). The assignment of the bands due adsorbed 1-pentanamine is reported in Table 3, based on Colthup et al. [27]

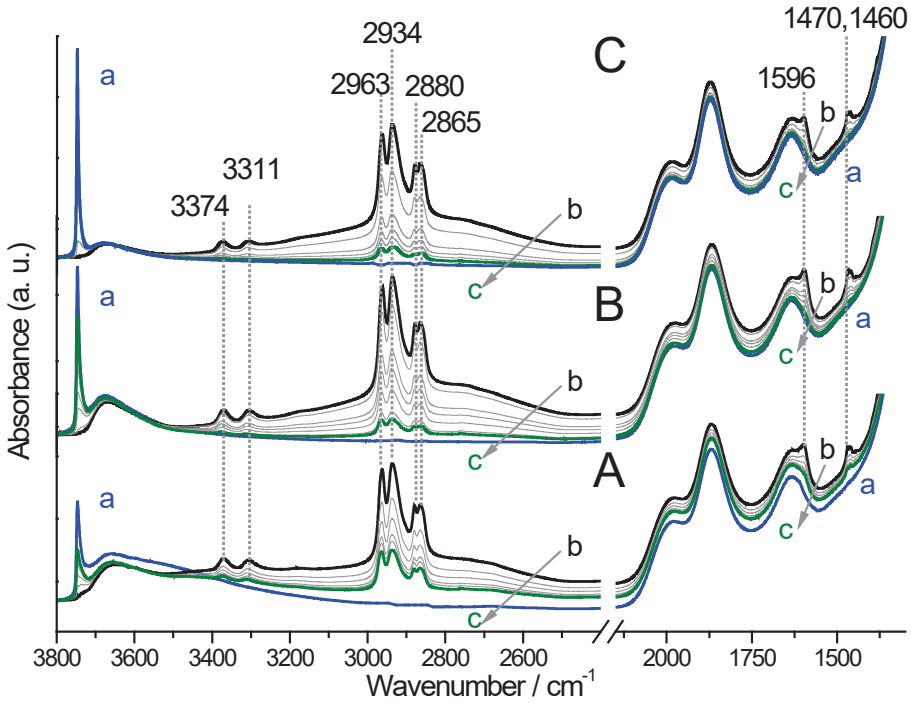

Figure 8. Infrared spectra of silica samples in the pristine form (Section A), after thermal treatment at 723 K (Section B), and after thermal treatment at 973 K (Section C): a) after outgassing at b.t.; b) in contact with 40 mbar 1-pentanamine vapor; c) progressive outgassing at b.t. until invariance of spectra (attained after ca. 1 h).

Table 3. Assignment of the bands due to adsorbed PA on SiO_2.

Adsorbed 1-pentanamine	
position (cm^{-1})	assignment
3374	$\nu_{asym}NH_2$
3311	$\nu_{sym}NH_2$
2968	$\nu_{asym}CH_3$
2934	$\nu_{asym}CH_2$
2880	$\nu_{sym}CH_3$
2865	$\nu_{sym}CH_2$
1605	δNH_2
1470	$\delta_{asym}CH_3$
1460	δCH_2

This allowed the admission of FA vapours on samples where PA was exclusively present in the adsorbed form without any amine in vapour phase. The same operative sequence as the MA+FA reaction was used, and the IR spectra obtained when adsorbing PA and then FA on thermally untreated silica are shown in Figure 9. The overall spectral evolution almost reproduces what was obtained for the MA+FA case (see Figure 5), with additional signals in the 3000-2800 cm^{-1} range due to νCH_2 modes of the methylene groups of PA.

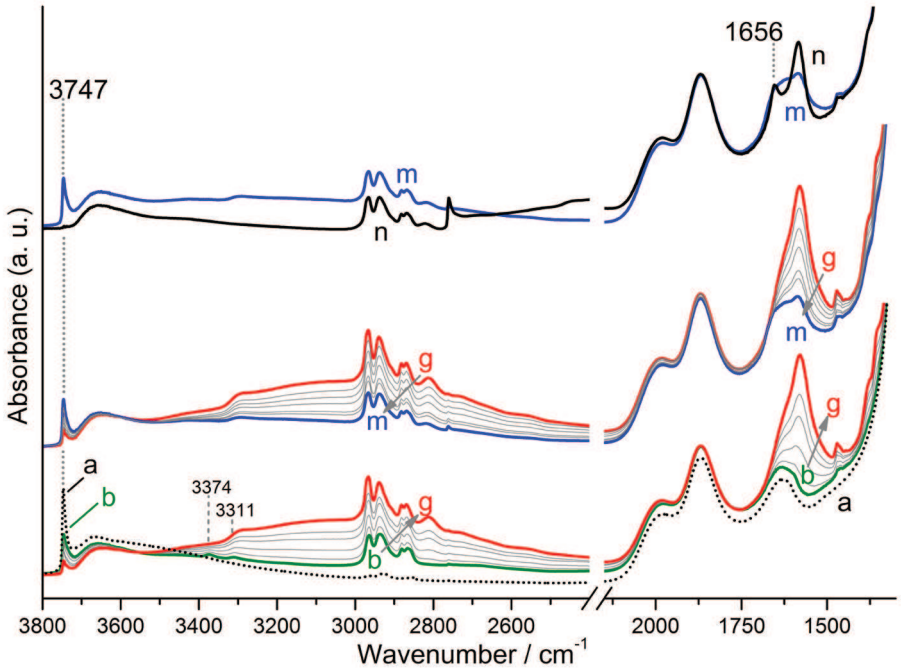

Figure 9. Infrared spectra of pristine SiO_2 outgassed at b.t. and subsequently contacted with 1-pentanamine (PA) and formic acid (FA): a) dotted black line, sample outgassed at b.t.; b) after admission of PA until having the intensity of the peak at 3747 cm^{-1}, due to isolated silanols; b→g) after admission of FA until depletion of νNH_2 signals at 3374 and 3311 cm^{-1}, grey curves show intermediate amounts of FA; g→m) after subsequent outgassing at b.t. until invariance of spectra (grey curves show intermediates steps of outgassing); n) after D_2O admission (20 mbar)/outgassing at b.t. until spectral invariance.

Noteworthy, a band at 1656 cm^{-1} is clearly detected after the final H/D exchange by contact with D_2O (curve n), assignable to the $\nu C{=}O$ of amide molecules, in this case expected to be N-pentylformamide. As for the previous case, IR data collected along

equivalent experiments on silica samples calcined at 723 K and 973 K are reported in Figure 10 and Figure 11.

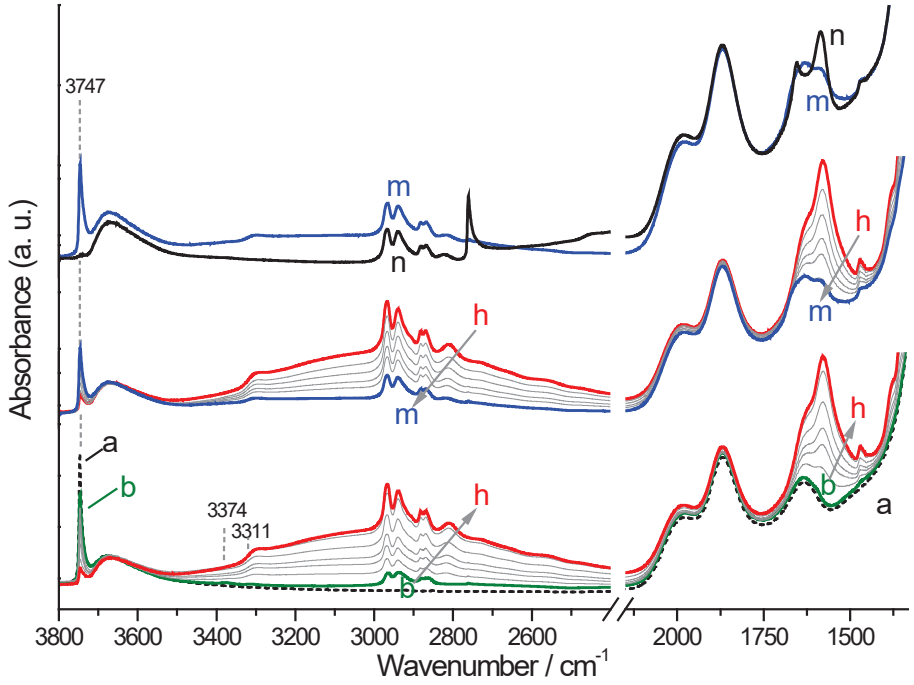

Figure 10. Infrared spectra of amorphous silica sample treated at 723 K in air, then outgassed at b.t. and subsequently contacted with 1-pentanamine (PA) and formic acid (FA): a) dotted black line, sample outgassed at b.t.; b) after admission of PA until halving the intensity of the peak at 3747 cm^{-1}, due to isolated silanols; b→h) after admission of FA until depletion of νNH_2 signals at 3374 and 3311 cm^{-1}; h→m) after subsequent outgassing at b.t. until invariance of spectra; n) after D_2O admission (20 mbar)/outgassing at b.t. until invariance of spectra.

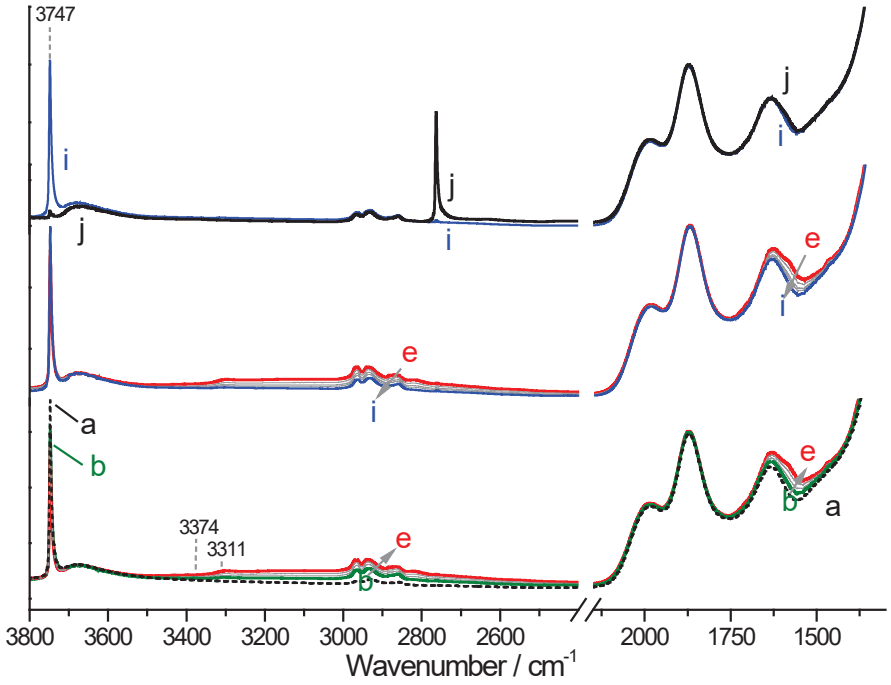

Figure 11. Infrared spectra of amorphous silica sample treated at 973 K in air, then outgassed at b.t. and subsequently contacted with 1-pentanamine (PA) and formic acid (FA): a) dotted black line, sample outgassed at b.t.; b) after admission of PA until halving the intensity of the peak at 3747 cm^{-1}, due to isolated silanols; b → e) after admission of FA until depletion of νNH_2 signals at 3374 and 3311 cm^{-1}; e → i) after subsequent outgassing at b.t. until invariance of spectra; j) after D_2O admission (20 mbar)/outgassing at b.t. until invariance of spectra.

Reaction between amines and formic acid: a comparative analysis of the role of surface hydroxylation

For the sake of clarity and brevity, a synoptic view of the spectral features due to species remaining on the surface of pristine and calcined silica samples after the sequential contact with MA/PA and FA, and the final H/D exchange is depicted in Figure 12, focusing on the range relevant for the νC=O band of amide species. Data resulting from both the MA+FA and PA+FA sets of experiments (panel A and B, respectively) show an equivalent trend: a ν(C=O) band at 1665/1656 cm^{-1} assignable to methylformamide/pentylformamide present when the catalyst is silica in the pristine form (curves a) and calcined at 723 K (curves b), whereas only traces of these signals appear for experiments carried out on silica calcined at 973 K (curves c). The resistance of pentylformamide towards hydrolysis allowed to confirm its

formation by HR-MS analysis of the washing aqueous solution of samples contacted with PA and FA (Figure 12 inset: m/z = 116.1069, and Figure A1 panel B in the Appendix for complete HR-MS spectra). This collection of data clearly indicates that amidation between MA/PA and FA occurred on silica only in the presence of silanols responsible of the 3742 cm^{-1} peak, no longer present after calcination at 973 K (see Figure 3B). Furthermore, formation of ionic pairs from adsorbed PA and FA (as monitored through the $\nu_{asym}COO^-$ signal at 1584 cm^{-1} in panel B) also seems to depend on the presence of silanols characterised by the νOH at 3742 cm^{-1}. This was not the case of the MA+FA reaction (panel A, band at 1582-1589 cm^{-1}), where adsorbed amine molecules were in equilibrium with molecules in vapour phase, and these latter underwent salification with incoming FA, irrespective of the hydroxylation state of the silica surface.

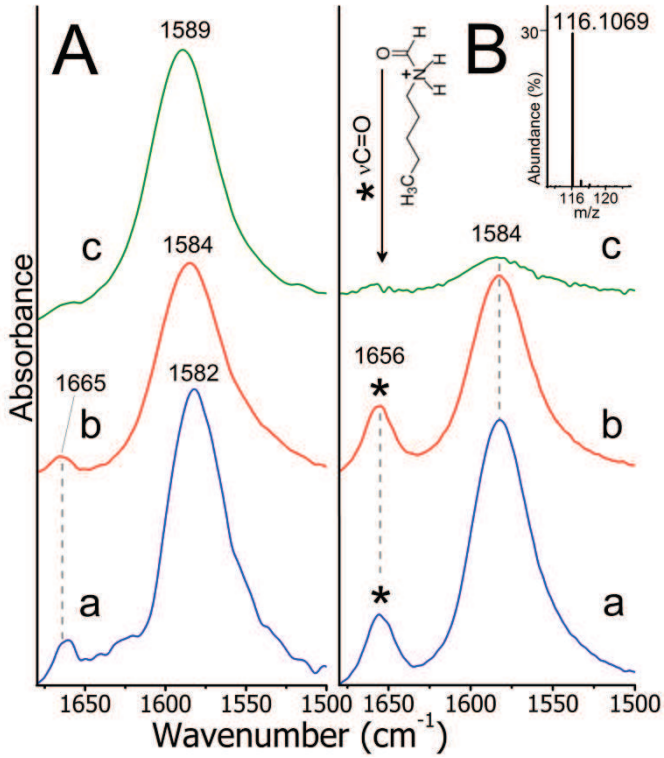

Figure 12. IR spectra, in the 1700-1500 cm^{-1} range, of species left adsorbed on the surface of SiO_2 samples after the sequential contact with MA + FA (panel A) or PA + FA (panel B): a) pristine SiO_2; b) SiO_2 calcined at 723 K; c) SiO_2 calcined at 973 K. The curves are the result of the difference between the last and the first spectra in Figure 5, Figure 6 and Figure 7 (MA + FA reaction), and Figure 9, Figure 10 and Figure 11 (PA+FA reaction).

Rationalization of experimental results by means of quantum chemical calculations

These experimental findings pose a fundamental question: why the presence of the specific SiOH peaked at 3742 cm^{-1} is mandatory for the occurrence of AB formation? Answering this question will indeed shed some light into the role of the silica surface in the reaction. To this end, quantum chemical calculations are used as they can provide an atomistic interpretation of the experiments. This part of the work was carried out in collaboration with the group of Prof. Ugliengo of the Department of Chemistry of the University of Torino. Calculations adopt a cluster approach within the ONIOM2[B3LYP/6-311++G(d,p):MNDO] method for optimization and frequency calculations and refining the energetics with single-point energy calculations at full B3LYP-D3/6-311++G(d,p) level. Further computational details are shown in the Methods section. The silica cluster model (shown in Figure 14A) presents two very weakly interacting SiOH groups, with a H···O and a O···O intersilanol distances of about 4.9 and 5.5 Å, respectively, as imposed by the rigidity of the model. It is worth noting that the four-Si-membered ring hosting the silanol pair did not play any specific role in the catalysis, as it simply derives from the edingtonite mineral adopted to define the cluster model (see Computational details). Calculated ν(OH) frequencies (Figure 13 and Table 4) are 3746 and 3751 cm^{-1} (using a scaling factor of 0.959 [29]); i.e., exactly mimicking the frequency shift of 5 cm^{-1} of the experimental 3742 and 3747 cm^{-1} bands.

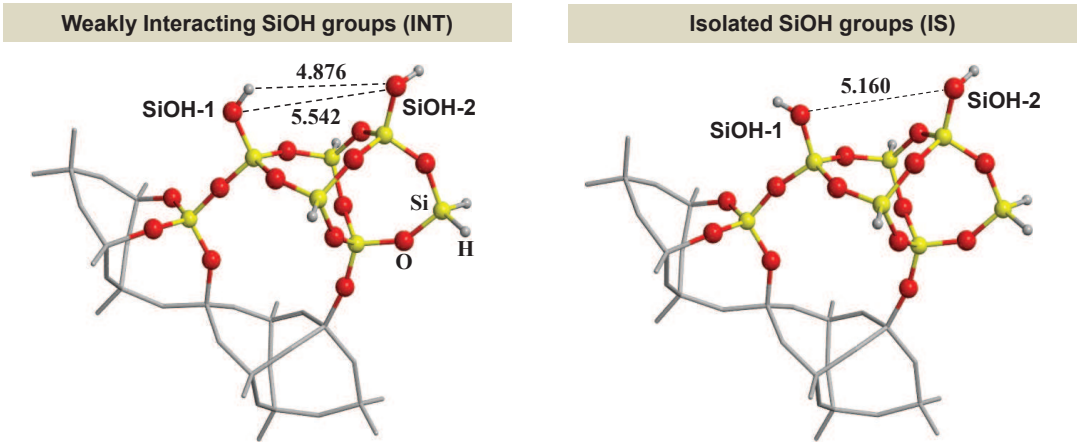

Figure 13. ONIOM2-optimized cluster models for the silica surface when the SiOH pairs are weakly interacting (INT) and do not interact (IS). Distances are in Å. Energetic and vibration information is provided in Table 5.

Rotation of the SiOH groups to avoid the weak through-space interaction equalizes the ν(OH) values, as expected (3751 and 3752 cm^{-1}).

Table 4. Absolute energies (in Hartrees) of the compounds involved in Figure 13: ONIOM2[B3LYP/6-311++G(d,p):MNDO] potential energies (E_{ONIOM2}), single-point potential energies at the B3LYP-D3/6-311++G(d,p)//ONIOM2 level, ($E_{B3LYP-D3}$); zero-point energy (ZPE) correction; and thermal correction to free energy at 298 K (G298). Relative energies (in kcal mol^{-1}) between INT and IS: relative potential energies ($\Delta E_{B3LYP-D3}$), including ZPE corrections (ΔU_0), and relative free energies at 298 K (ΔG_{298}). Calculated and scaled frequencies (in cm^{-1}) for the O-H stretching vibrational mode of the SiOH groups (scaling factor of 0.959).

		INT	IS
E_{ONIOM2}		-3165.014191	-3165.014395
$E_{B3LYP-D3}$		-7041.170498	-7041.170052
ZPE corrections		0.310190	0.310047
Correction to G_{298}		0.227813	0.227777
ΔE		0.00	0.28
ΔU_0		0.00	0.19
ΔG_{298}		0.00	0.26
Calculated	SiOH-1	3907	3912
frequencies	SiOH-2	3912	3913
Scaled frequencies	SiOH-1	3746	3751
	SiOH-2	3751	3752

These results indicate that the model reported in Figure 14A does account quantitatively for the measured spectroscopic features on the real silica sample outgassed at 723 K. The adopted cluster model exhibits H atoms to cap the Si dangling bonds. In the real material, exposed surface tetrahedra exhibit OH groups as termination, which renders the material hydrophilic to various degrees. To check for the dependence of the results upon H or OH termination, some calculations are repeated for cluster terminated by OH groups.

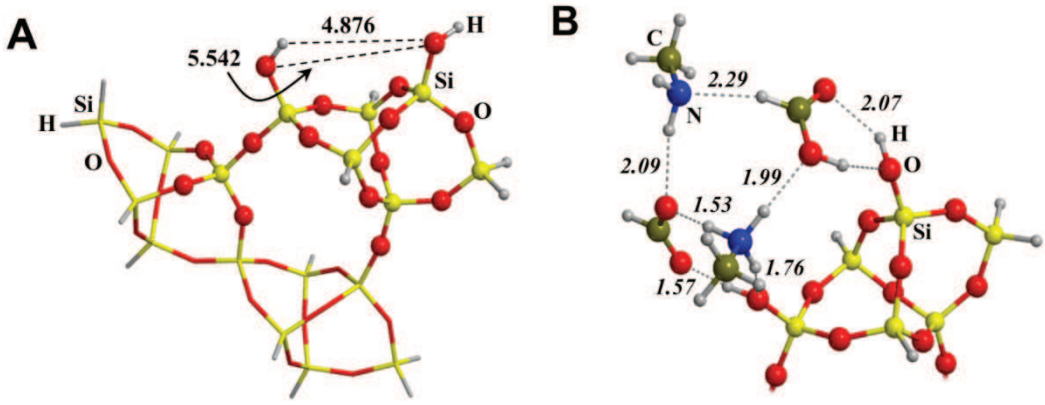

Figure 14. A) cluster model for the SiO_2 surface, where atoms in balls belong to the high-level zone and in sticks to the low-level zone in the ONIOM2 calculations. B) Pre-reactants structure for AB formation, presenting ionic and neutral forms of the FA/MA pair. Only the reactive part is presented. Bond distances are in Å.

The optimized structural parameters of this cluster model are very similar to those in the H-saturated one, with the H···O and a O···O inter-silanol distances of about 5.0 and 5.6 Å (Figure 15). The calculated ν(OH) frequencies of 3745 and 3750 cm^{-1} (using the 0.959 scaling factor), are very close to those for the H-saturated cluster with the same frequency shift of 5 cm^{-1} (Table 5). In conclusion, details of the H-terminated cluster model adopted in this work are indistinguishable from the OH-terminated one.

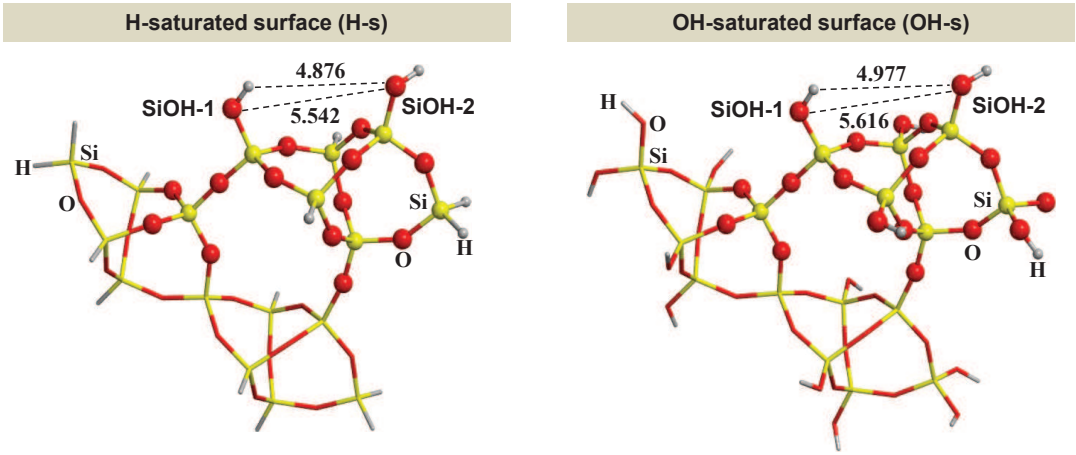

Figure 15. ONIOM2-optimized cluster models for the silica surface when the Si dangling bonds were saturated by H atoms (H-s) or by OH groups (OH-s). Distances are in Å. Vibration information is provided in Table 6.

As mentioned above, to simplify the calculations, FA and MA are adopted as reactants to give methylformamide (MFA).

Table 5. ONIOM2[B3LYP/6-311++G(d,p):MNDO]-calculated and scaled frequencies (in cm^{-1}) for the O-H stretching vibrational mode of the SiOH groups (scaling factor of 0.959).

		H-s	OH-s
Calculated	SiOH-1	3907	3909
frequencies	SiOH-2	3912	3914
Scaled frequencies	SiOH-1	3746	3745
	SiOH-2	3751	3750

Experimentally, salification is observed, meaning that $CH_3NH_3^+$ and $HCOO^-$ are present, as well as CH_3-$(CH_2)_4$-NH_3^+ and $HCOO^-$ for the PA+FA case. However, in contrast with neutral FA and MA, these ionic species are not reactive towards AB formation. Thus, a suitable initial state is that shown in Figure 14B, in which two FA and two MA interact with the silica sites, with one FA/MA pair in ionic form and the other as neutral pair. Remarkably, the same system in which all pairs appear as ionic species is less stable (by about 5 kcal mol^{-1}) than the structure of Figure 14B due to a missing favourable interaction involving one SiOH group (Figure 16 and Table 6).

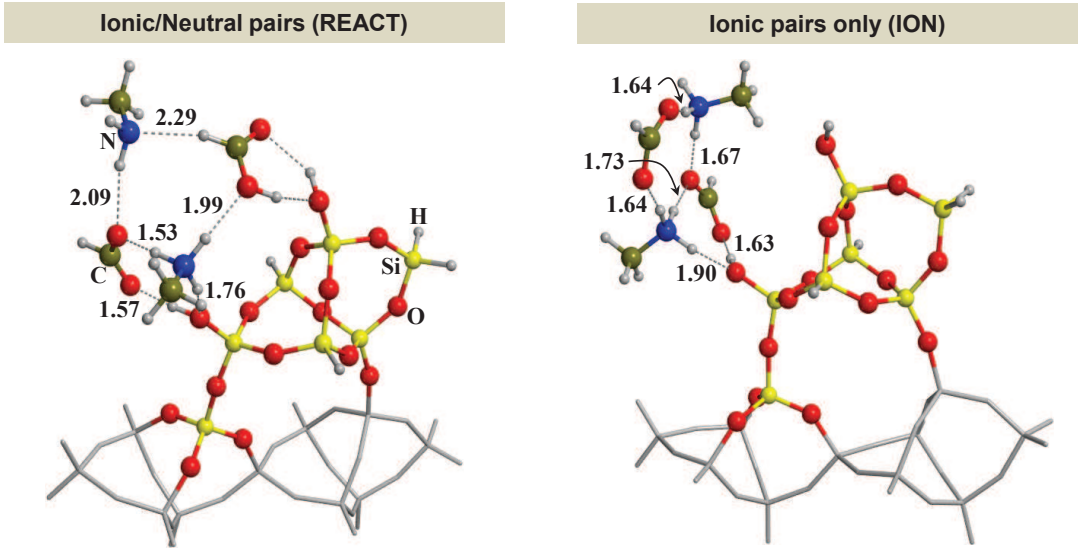

Figure 16. ONIOM2-optimized systems (H-bond distances in Å) with 2 formic acids (FA) and 2 methylamines (MA) on the silica surface model. One system presents one FA/MA pair in the ionic state and the other in the neutral state (REACT). The other presents two FA/MA pairs in the ionic state (ION). Energetic information is provided in Table 6.

Table 6. Absolute energies (in Hartrees) of the compounds involved in Figure 16: ONIOM2[B3LYP/6-311++G(d,p):MNDO] potential energies (E_{ONIOM2}), single-point potential energies at the B3LYP-D3/6-311++G(d,p)//ONIOM2 level, ($E_{B3LYP-D3}$); zero-point energy (ZPE) correction; and thermal correction to free energy at 298 K (G298). Relative energies (in kcal mol^{-1}) between REACT and ION: relative potential energies ($\Delta E_{B3LYP-D3}$), including ZPE corrections (ΔU_0), and relative free energies at 298 K (ΔG_{298}).

	REACT	ION
E_{ONIOM2}	-3736.526868	-3736.520856
$E_{B3LYP-D3}$	-7612.709486	-7612.703444
ZPE corrections	0.515262	0.515498
Correction to G_{298}	0.407964	0.410183
ΔE	0.00	3.79
ΔU_0	0.00	3.94
ΔG_{298}	0.00	5.18

Figure 17A shows the proposed mechanism for the AB formation. The neutral forms of MA and FA of the initial state (REACT) react through a C-N coupling (TS1) to form the metastable $CH_3NH_2(+)CHOHO(-)$ zwitterionic species (INT). The calculated free energy barrier at 298 K ($\Delta G^{\neq}_{298}$) of this coupling is 17.1 kcal mol^{-1}, with INT at 14.9 kcal mol^{-1} with respect to REACT. The second step involves the dehydration and final formation of MFA. It takes place by two simultaneous processes (TS2): i) a proton transfer from $CH_3NH_3^+$ to the OH group of INT to release H_2O; and ii) a proton transfer from the NH_2 moiety of the metastable species to the deprotonated HCOO-. This step has an intrinsic $\Delta G^{\neq}_{298}$ of 23.0 kcal mol^{-1} and the overall process is favourable by -11.7 kcal mol^{-1} (see PROD-n). Interestingly, the initial ionic FA/MA pair transforms into a neutral pair after AB condensation (see PROD-n). An interesting point is to assess whether this neutral pair can be converted back to the ion pair, restoring its catalytic power for a new condensation cycle. This process is shown in Figure 17B: FA transfers its proton to MA, which moreover is assisted by the H_2O molecule resulting from the AB condensation. The calculated intrinsic $\Delta G^{\neq}_{298}$ is very low (1.2 kcal mol^{-1}, TS3) and the final state is more stable by 1.1 kcal mol^{-1} (PROD-i).

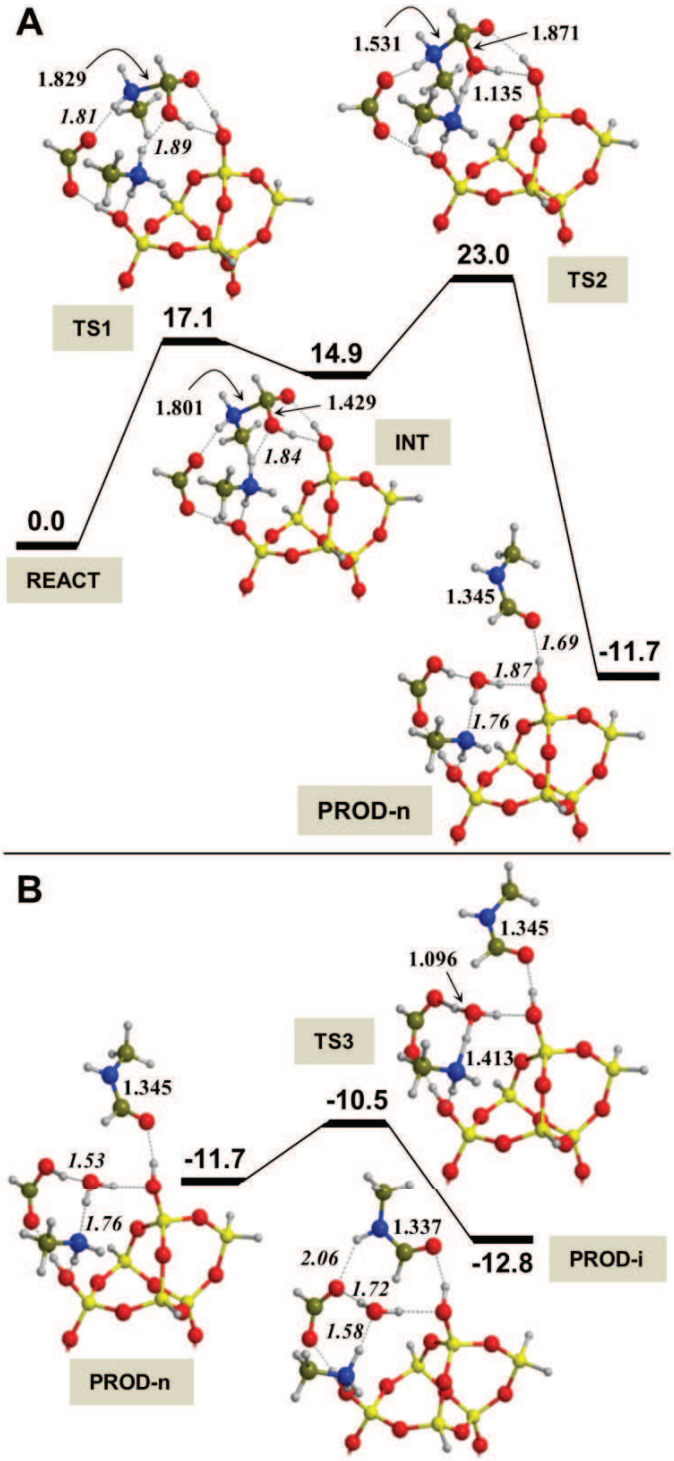

Figure 17. Free energy profiles at 298 K (in kcal mol^{-1}) for the AB formation mechanism (A) and the restoring of the ionic FA/MA pair. Bond distances are in Å.

The proposed mechanism clearly shows that silica surface functionalities catalyse the AB formation, as the uncatalyzed gas-phase AB process proceeds in a concerted way with a huge kinetic barrier of $\Delta G^{\neq}_{298}$ = 44 kcal mol^{-1} (Figure 18 and Table 7). The key point is the presence of the spatially specific SiOH surface sites, allowing the coexistence of FA/MA pairs in their ionic and neutral states. The FA/MA ion pair actively participates in the AB formation between the FA/MA neutral pair, particularly in the dehydration step, in which the acidity of $CH_3NH_3^+$ lowers the energy barrier for the H_2O elimination. Remarkably, the removal of one silanol group from our model cluster leads to the transformation of the neutral FA/MA pair into its ionic form, which is stabilized by the interaction with the other FA/MA ion pair (see Figure 19) *de facto* preventing the nucleophilic step essential for the AB formation. Thus, the presence of only isolated surface SiOH does not provide a suitable scenario for the AB formation, in full agreement with the spectroscopic evidence provided by Figure 12A, B, curves c. Moreover, the interaction of the neutral FA with both SiOH and the $CH_3NH_3^+$ species activates the C atom of the C=O group towards the nucleophilic attack, as shown by the formation of the metastable $CH_3NH_2(+)CHOHO(-)$ species.

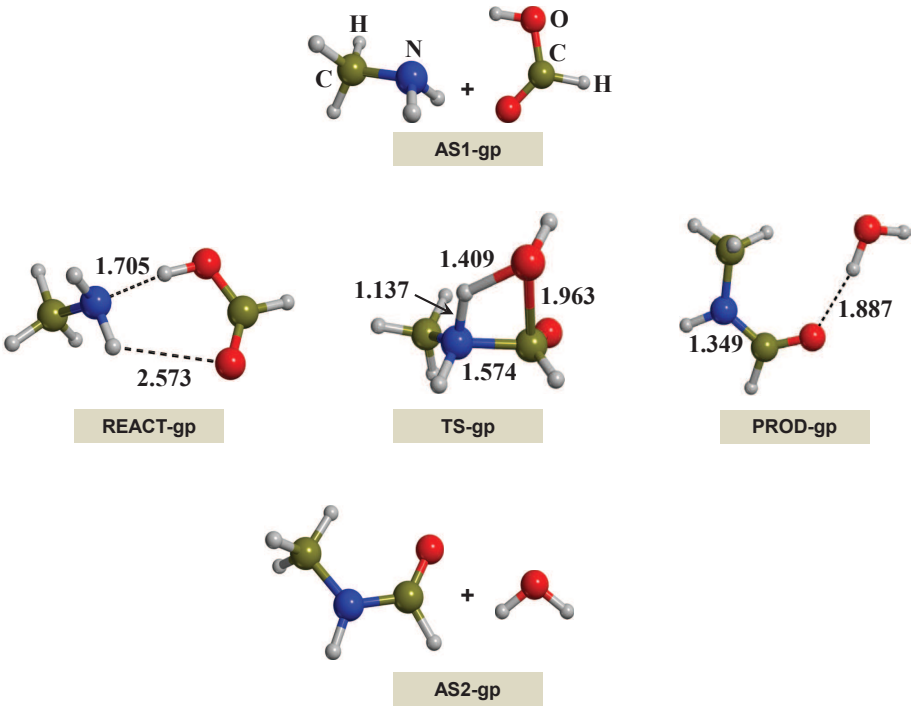

Figure 18. B3LYP-D3/6-311++G(d,p)-optimized geometries of the stationary points involved in the uncatalyzed gas-phase reaction of amide bond formation between formic acid and methylamine. Bond distances in Å. Energetic information is provided in Table 7.

Table 7. Absolute energies (in Hartrees) of the compounds involved in Figure 18: B3LYP/6-311++G(d,p) potential energies (E_{B3LYP}), single-point potential energies at the B3LYP-D3/6-311++G(d,p)//B3LYP/6-311++G(d,p) level, ($E_{B3LYP-D3}$); zero-point energy (ZPE) correction; and thermal correction to free energy at 298 K (G298). Relative energies (in kcal mol^{-1}) of the stationary points, taking as 0 energy reference AS1-gp: relative potential energies ($\Delta E_{B3LYP-D3}$), including ZPE corrections (ΔU_0), and relative free energies at 298 K (ΔG_{298}).

	AS1-gp	REACT-gp	TS-gp	PROD-gp	AS2-gp
E_{B3LYP}	-285.7216589	-285.7415248	-285.6628826	-285.742283	-285.7310966
$E_{B3LYP-D3}$	-285.7239602	-285.7474656	-285.6703375	-285.7484664	-285.7345787
ZPE corrections	0.097477	0.100062	0.096242	0.098240	0.095118
Correction to G_{298}	0.050465	0.067686	0.066682	0.064589	0.048174
ΔE	0.00	-14.75	33.65	-15.38	-6.66
ΔU_0	0.00	-13.13	32.87	-14.90	-8.14
ΔG_{298}	0.00	-3.94	43.83	-6.51	-8.10

Remarkably, formation of this kind of metastable intermediates was also identified in simulations on the peptide bond formation in the ribosome, [30] which induces a lowering of the energy barriers compared to the uncatalyzed processes. The stabilization of these metastable species, in our case, is due to the interaction with one silica SiOH group and the FA/MA ion pair adsorbed on the other SiOH, whereas in the ribosome a sugar OH functionality and a water molecule play this role.

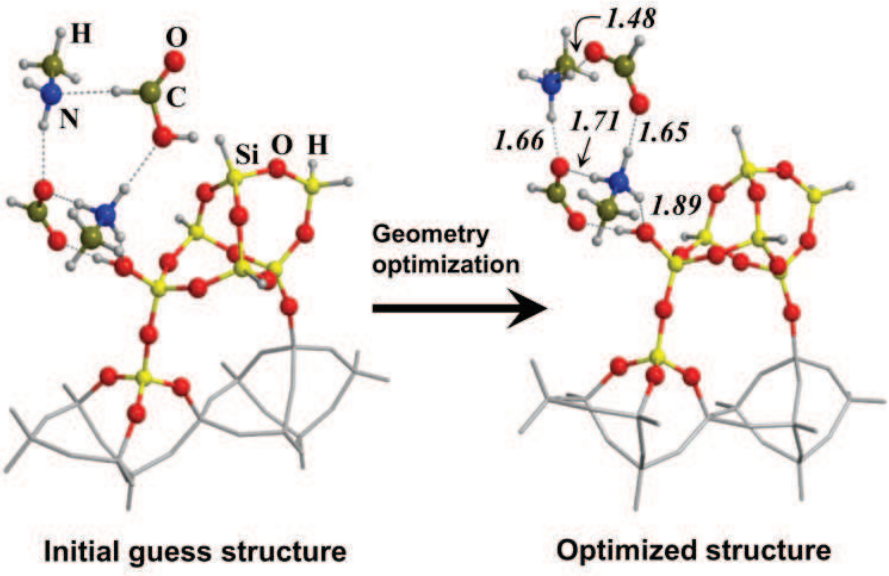

Figure 19. ONIOM2-optimized geometry (H-bond distances in Å) of a system with two formic acids and two methylamines on a silica surface model with only one SiOH group. The initial guess structure is REACT in which one SiOH group was removed.

Kinetic rate estimates for the silica-catalysed AB formation

A simple kinetic model is worked out for the AB reaction based on the computed potential energy surface as shown in Figure 17A. Considering that the reaction is monitored under the thermal effect of the infrared beam, (assumed to increase the temperature from 298 K up to 323 K), the relative free energy values of Figure 17A at 323 K are recalculated.

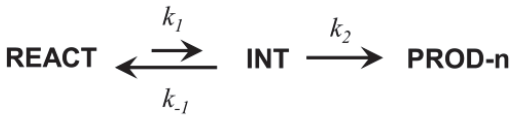

$$\frac{d[\mathbf{PROD-n}]}{dt} = k[\mathbf{REACT}] = K \times k_2[\mathbf{REACT}]$$

$$\left(K = \frac{k_1}{k_{-1}}\right)$$

Scheme 1. Kinetic model adopted to derive rate constants and kinetic information for the AB formation.

New values are: 11.5, 9.6, 18.5 and -7.8 kcal mol^{-1} for TS1, INT, TS2 and PROD-n, (assuming REACT as the zero energy reference). Scheme 1 describes a kinetic model, envisaging a pre-equilibrium step. By using data from the DFT calculations is possible to arrive at $k_1 = 5.2\times10^{4}$ s^{-1}, $k_{-1} = 1.6\times10^{11}$ s^{-1}, $k_2 = 9.9\times10^{6}$ s^{-1}, $K = 3.2\times10^{-7}$ and k = 3.2 s^{-1} resulting in a half-life time of $\tau_{1/2}$ = 0.1 s. The reaction is, therefore, reasonably fast. A possible comparison is with the dissolution rate of amorphous silica (our sample) in water, whose kinetic constant was reported experimentally to be 1.33×10^{-5} mol m^{-2} s^{-1}, [31] which is five order of magnitude smaller than k value. Comparison between experiment and computed kinetic constants is very delicate. However, the theoretical work of Pelmenschikov et al. [32] on dissolution of silica was in very good agreement with the experimental value giving confidence to the present comparison.

Conclusions

This work focuses on the amide bond formation between amines and carboxylic acids occurring on silica surfaces by combining IR measurements and quantum chemical calculations based on established accurate model chemistry. IR results indicate that AB formation occurs only if specific weakly interacting SiOH pairs are present. The amount of these pairs depends on the "thermal history" of the material. In the present case, we adopted a pyrogenic silica with an initial low silanol density (*ca*. 1.5 OH nm^{-2}). We proved that thermal treatment at 973 K almost depletes the active pairs. Quantum chemical calculations provided the atomistic model for this SiOH pairs, which in turn are responsible of the coexistence of amine/carboxylic acid pairs in their neutral and ionic forms. This coexistence is the key point for the occurrence of the reaction, as the neutral pair is the reacting one while the ion pair acts as catalyst for the dehydration step. Moreover, the interaction of the neutral pair with both surface SiOH and the ion pair stabilizes a metastable intermediate species, inferring a significant decrease of the overall energetics compared to the uncatalyzed gas-phase process. Such an intermediate stabilization resembles that found in simulations for the peptide bond formation operated by the ribosome, in which one surface SiOH group and the ionic pair play the role of a sugar OH and a water molecule in the biological system. A kinetic model based on the DFT free energy barriers indicates that our silica-catalysed mechanistic proposal for the AB formation is reasonably fast.

Experimental Details

The commercial silica powder AEROSIL® OX50 (by EVONIK; SiO_2 content ≥99.8 wt%, as from www.aerosil.com) was used as catalyst. Formic acid, 1-pentanamine and D_2O (99.90% D) were high-purity Sigma-Aldrich products. The vapours of these chemicals, as well as those of Milli-Q water (Millipore system), were admitted onto the samples in the IR cell after several freeze-pump-thaw cycles. Pure gas N-methylamine was purchased from PRAXAIR (UCAR).

The thermal treatments of the samples were carried out in a muffle furnace. SiO_2 powder was pressed in form of self-supporting pellets which were introduced in the furnace and ramped for 30 min up to 723 K and kept at this temperature for 2.5 hours. Samples were then left to cool down to room temperature (required time *ca*. 5 hours). A set of so treated pellets was then ramped for 30 min up to 973 K, again kept at this temperature for 2.5 hours, and left to cool down to room temperature (required time *ca*. 9 hours).

Volumetric measurements of the specific surface area (N_2 adsorption at 77 K; BET method) were carried out on pieces obtained by manual crushing in mortar pellets of the pristine silica or resulting from the thermal treatments. The instrument used was an ASAP2020 by Micromeritics. Before measurements, samples were outgassed overnight at room temperature (residual pressure: 10^{-4} mbar).

For IR spectroscopic measurements, pellets of the pristine silica or resulting from the thermal treatments described above were placed in a traditional IR cell equipped with CaF_2 windows and a valve for connection to vacuum lines (residual pressure $1.0 \cdot 10^{-5}$ mbar) allowing adsorption/desorption experiments to be carried out in situ. The spectra were collected with a Bruker VECTOR22 instrument (La-DTGS detector) at beam temperature (*ca*. 323 K) with a resolution of 4 cm^{-1}, by accumulating 100 scans, to attain a good signal-to-noise ratio.

After experiments involving the contact of both reactants (amines and formic acid) with the samples, pellets were removed from the cell, manually ground in an agate mortar and suspended in 0.5 mL of Milli-Q water. Suspensions were shaken for 15 min by a Vortex mixer and then centrifuged for 10 min at 10k rpm. After removal of the supernatant, the solid was treated a second time with the same volume of water. The two aliquots of the aqueous solutions were then mixed, and analyzed by high-resolution mass spectrometry.

High-resolution mass spectrometry analyses of the washing solutions were performed using an LTQ Orbitrap mass spectrometer (Thermo Scientific) equipped with an atmospheric pressure interface and an electrospray ionization (ESI) source.

The source voltage was set to 4.48 kV. The heated capillary temperature was maintained at 538 K. The tuning parameters adopted for the ESI source were: capillary voltage 0.02 V, tube lens 24.77 V; for ions optics: multipole 0 offset −4.28 V, lens 0 voltage −4.36 V, multipole 0 offset −4.28 V, lens 1 voltage −13.69 V, gate lens voltage −8.84 V, multipole 1 offset −18.69 V, front lens voltage −5.09 V. Mass accuracy of recorded ions (vs calculated) was ± 1 mmu (without internal calibration). Samples, added of 100 μL of a 0.1 M HCOOH aqueous solution, were delivered directly to the mass spectrometer via a Hamilton microliter syringe at constant flow (10 μl min^{-1}).

Computational Details

Calculations were run on a cluster model to simulate a silanol-containing amorphous silica surface (shown in Fig. 1). The cluster was derived from a secondary building unit of the crystalline all-silica edingtonite structure to ensure sufficient rigidity in the models during geometry optimization as envisaged by the presence of four-Si-membered rings in the framework.

All molecular calculations were performed using the Gaussian 09 program. [33] To increase the speed of the calculations, the structures of the reactants, transition states, and products were optimized using the ONIOM2[B3LYP/6-311++G-(d,p):MNDO] [34-37] method (see Fig. 2A). For consistency, reactant molecules were included in the high-level zone of the ONIOM2 calculations. The reaction energetics were refined by performing full B3LYP-D3/6-311++G(d,p) single-point energy calculations on the optimized ONIOM2 stationary points, with dispersion interactions taken into account by including the Grimme's D3 correction term. [38] Structures were characterized by the analytical calculation of the harmonic frequencies as minima (reactants and products) and saddle points (transition states). Free energies were computed including enthalpy and entropy contributions obtained at the ONIOM2 level to the B3LYP-D3/6-311++G(d,p)//ONIOM2 energies resulting from the standard rigid-rotor/harmonic-oscillator treatment. [39]

Calculations based on crystalline models of α-quartz surfaces were performed using the periodic ab initio CRYSTAL14 code [40] For these calculations, we used the B3LYP density functional method and the all electron Gaussian 6-311G(d,p) standard basis set.

References

[1] Pattabiraman V. R. and Bode J. W. *Nature* **2011** (480) 471-479.
[2] Constable D. J. C., Dunn P. J., Hayler J. D., Humphrey G. R., Leazer J. J. L., Linderman R. J., Lorenz K., Manley J., Pearlman B. A., Wells A., Zaks A. and Zhang T. Y. *Green Chem.* **2007** (9) 411-420.
[3] Bernal J. D. *Proc. Phys. Soc., London, Sect. B* **1949** (62) 597-618.
[4] Smith J. V. *Proc. Natl. Acad. Sci. USA* **1998** (95) 3370-3375.
[5] Orgel L. E. *Origins Life Evol. Biospheres* **1998** (28) 227-234.
[6] Lahav N., White D. and Chang S. *Science* **1978** (201) 67-69.
[7] Ferris J. P., Hill A. R., Liu R. and Orgel L. E. *Nature* **1996** (381) 59-61.
[8] Martra G., Deiana C., Sakhno Y., Barberis I., Fabbiani M., Pazzi M. and Vincenti M. *Angew. Chem. Int. Ed.* **2014** (53) 4671-4674.
[9] Rimola A., Sodupe M. and Ugliengo P. *J. Am. Chem. Soc.* **2007** (129) 8333-8344.
[10] Schreiner E., Nair N. N., Wittekindt C. and Marx D. *J. Am. Chem. Soc.* **2011** (133) 8216-8226.
[11] Phuakkong O., Bobuatong K., Pantu P., Boekfa B., Probst M. and Limtrakul J. *ChemPhysChem* **2011** (12) 2160-2168.
[12] Zaia M. D. A. *Amino Acids* **2004** (27) 113-118.
[13] Lambert J.-F. *Origins Life Evol. Biospheres* **2008** (38) 211-242.
[14] Román-Leshkov Y. and Davis M. E. *ACS Catal.* **2011** (1) 1566-1580.
[15] Rimola A., Costa D., Sodupe M., Lambert J.-F. and Ugliengo P. *Chem. Rev.* **2013** (113) 4216-4313.
[16] Mitchell A. R. *Pept. Sci.* **2008** (90) 175-184.
[17] Meng M., Stievano L. and Lambert J.-F. *Langmuir* **2004** (20) 914-923.
[18] Lopes I. n., Piao L., Stievano L. and Lambert J.-F. o. *J. Phys. Chem. C* **2009** (113) 18163-18172.
[19] Lambert J.-F., Jaber M., Georgelin T. and Stievano L. *Phys. Chem. Chem. Phys.* **2013** (15) 13371-13380.
[20] Muller A. W. J. and Schulze-Makuch D. *Phys. A* **2006** (362) 369-381.
[21] Akouche M., Jaber M., Maurel M.-C., Lambert J.-F. and Georgelin T. *Angew. Chem. Int. Ed.* **2017** (56) 7920-7923.
[22] Rimola A., Ugliengo P. and Sodupe M. *Comput. Theor. Chem.* **2015** (1074) 168-177.
[23] Morrow B. A. and Gay I. D. in The Surface Properties of Silicas, A. P. Legrand Eds. **1998** (John Wiley & Sons Ltd, Chichester).
[24] Mukherjee G. D., Vaidya S. N. and Sugandhi V. *Phys. Rev. Lett.* **2001** (87) 4.
[25] Alessi A., Agnello S., Buscarino G. and Gelardi F. M. *Journal of Raman Spectroscopy* **2013** (44) 810-816.
[26] Carteret C. *J. Phys. Chem. C* **2009** (113) 13300-13308.

[27] Colthup N. B., Daly L. H. and Wiberley S. E. *Introduction to Infrared and Raman Spectroscopy* **1975** (Academic Press, New York).
[28] Nakamoto K. *Infrared and Raman Spectra of Inorganic and Coordination Compounds* **1986** (John Wiley & Sons, New York).
[29] Tosoni S., Pascale F., Ugliengo P., Orlando R., Saunders V. R. and Dovesi R. *Mol. Phys.* **2005** (103) 2549-2558.
[30] Świderek K., Marti S., Tuñón I., Moliner V. and Bertran J. *J. Am. Chem. Soc.* **2015** (137) 12024-12034.
[31] Icenhower J. P. and Dove P. M. *Geochim. Cosmochim. Acta* **2000** (64) 4193-4203.
[32] Pelmenschikov A., Strandh H., Pettersson L. G. M. and Leszczynski J. *J. Phys. Chem. B* **2000** (104) 5779-5783.
[33] Frisch M. J., Trucks G. W., Schlegel H. B., Scuseria G. E., Robb M. A., Cheeseman J. R., Scalmani G., Barone V., Mennucci B., Petersson G. A., Nakatsuji H., Caricato M., Li X., Hratchian H. P., Izmaylov A. F., Bloino J., Zheng G., Sonnenberg J. L., Hada M., Ehara M., Toyota K., Fukuda R., Hasegawa J., Ishida M., Nakajima T., Honda Y., Kitao O., Nakai H., Vreven T., J. A. Montgomery J., Peralta J. E., Ogliaro F., Bearpark M., Heyd J. J., Brothers E., Kudin K. N., Staroverov V. N., Keith T., Kobayashi R., Normand J., Raghavachari K., Rendell A., Burant J. C., Iyengar S. S., Tomasi J., Cossi M., Rega N., Millam J. M., Klene M., Knox J. E., Cross J. B., Bakken V., Adamo C., Jaramillo J., Gomperts R., Stratmann R. E., Yazyev O., Austin A. J., Cammi R., Pomelli C., Ochterski J. W., Martin R. L., Morokuma K., Zakrzewski V. G., Voth G. A., Salvador P., Dannenberg J. J., Dapprich S., Daniels A. D., Farkas O., Foresman J. B., Ortiz J. V., Cioslowski J. and Fox D. J. *Gaussian 09* **2013**.
[34] Becke A. D. *J. Chem. Phys.* **1993** (98) 5648-5652.
[35] Dewar M. J. S. and Thiel W. *J. Am. Chem. Soc.* **1977** (99) 4899-4907.
[36] Lee C., Yang W. and Parr R. G. *Phys. Rev. B* **1988** (37) 785-789.
[37] Vreven T. and Morokuma K. *J. Comput. Chem.* **2000** (21) 1419-1432.
[38] Grimme S., Ehrlich S. and Goerigk L. *J. Comput. Chem.* **2011** (32) 1456-1465.
[39] McQuarrie D. *Statistical Mechanics* **1986** (Harper and Row, New York).
[40] Dovesi R., Orlando R., Erba A., Zicovich-Wilson C. M., Civalleri B., Casassa S., Maschio L., Ferrabone M., De La Pierre M., D'Arco P., Noël Y., Causà M., Rérat M. and Kirtman B. *Int. J. Quantum Chem.* **2014** (114) 1287-1317.

Appendix

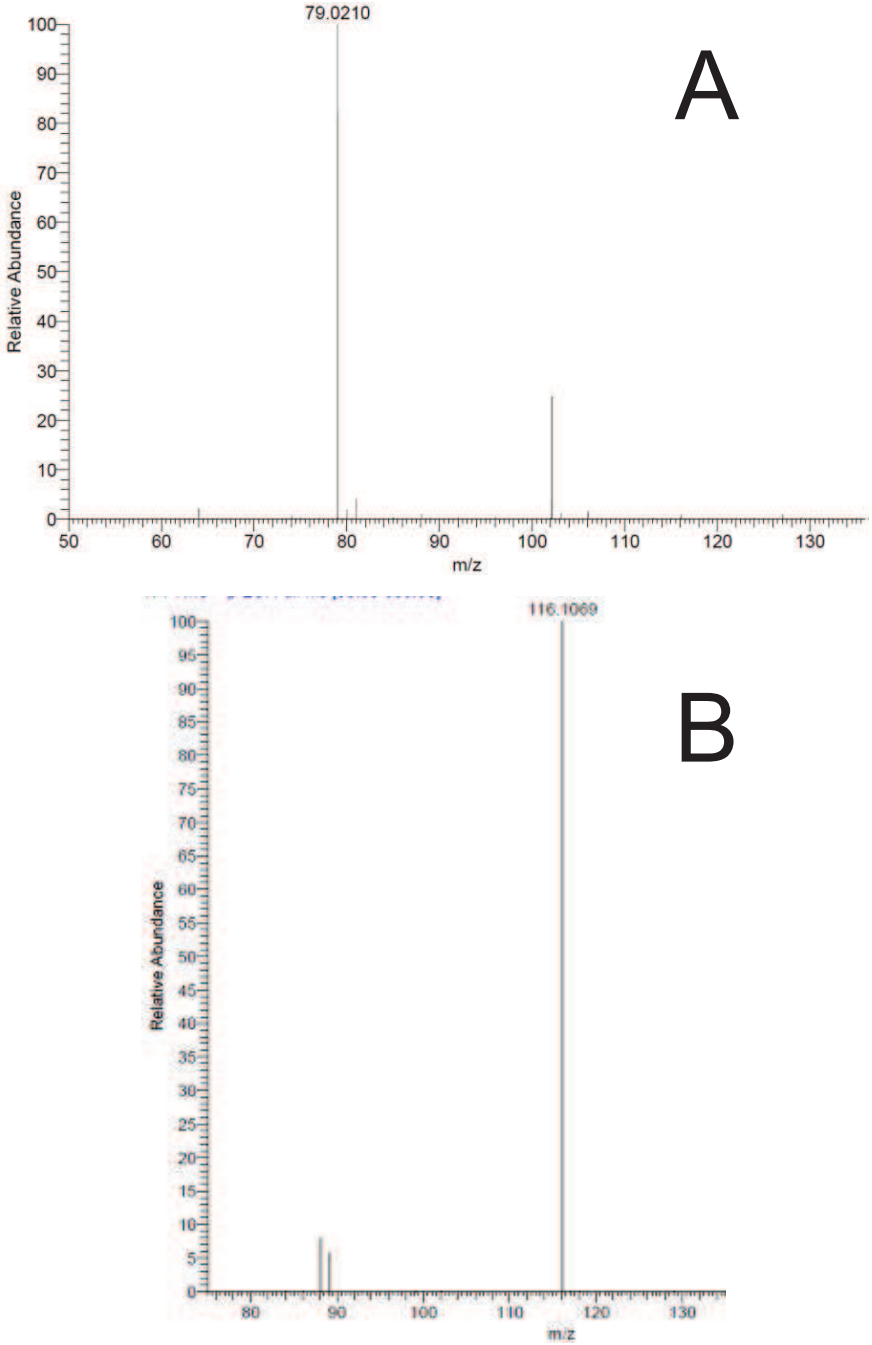

Figure A1. HR-MS spectra (50/75 - 140 m/z) of aqueous solution (5 ppm) of: A) methylformamide (mass expected at 60.0443 m/z); B) N-pentylformamide.

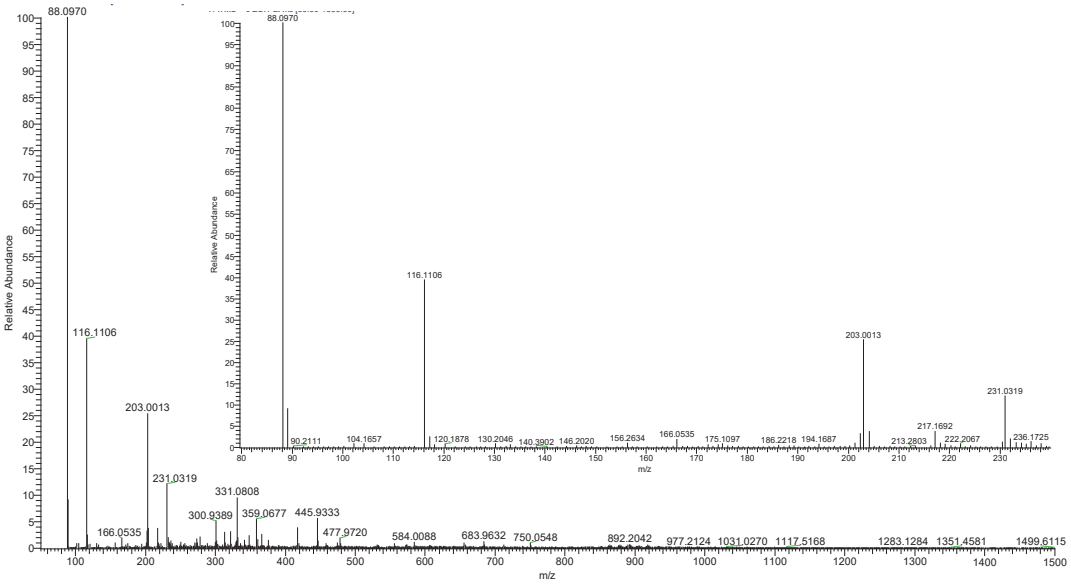

Figure A2. HR-MS spectrum (50 – 1500 m/z) of the aqueous solution resulting from washing a silica sample treated at 723 K and then contacted in the infrared cell with 1-pentanamine and formic acid vapors. Inset: zoom view of the 50 – 280 m/z range.

Signals at m/z values 88.0970 and 116.1106 are due to 1-pentanamine (PA) and N-pentylformamide (PFA), respectively (both protonated, because of the experimental conditions). Signals at m/z values 203.0013 and 231.0319 are due to PA+PFA and PFA+PFA single-charge adducts, respectively.

Chapter Two

Amide and peptide bond formation on the surface of α-quartz

From amorphous silica to α-quartz: relevance in prebiotic chemistry. A computational approach

While the results obtained on amorphous silica are fully valid for technological applications, it is hard to put them in the prebiotic context due to the absence of amorphous silica as natural material. In nature silica is present in its crystalline polymorphs, mainly α-quartz or β-cristobalite. [1, 2] The question is, therefore, whether the presence of the specific silanol pair responsible of the stabilization of the ion/neutral reactive species is exclusive of a specifically treated amorphous silica material. To shed some light into this aspect, in this chapter, the occurrence of specific surface SiOH pairs is studied at the α-quartz hydroxylated (010) surface, one of the most common crystal faces of α-quartz. This surface has a surface OH density of 7.4 OH nm^{-2} and has been exhaustively characterized theoretically. [3] Due to the high degree of hydroxylation, most of the silanol groups are H-bonded so that the pristine surface does not exhibit the specific SiOH non-interacting pairs (see "pristine surface" of Figure 1A). However, mutually interacting silanol groups can undergo condensation reactions yielding the formation of siloxane groups; *i.e.*, SiOH + SiOH → Si-O-Si + H_2O, a process quite common on such a highly hydroxylated surface. Hence, "defects" are created in the silanol population of an ideally perfect crystalline surface. Also in this case, a condensation process is identified, giving rise to the two isolated pairs (see Figure 1A). Optimizations are carried out at B3LYP/6-311G(d,p) level with the CRYSTAL14 program [4] the surface upon condensation of these silanol groups. The resulting surface (see "condensed surface" of Figure 1A and B) exhibits the specific SiOH pair with H···O and O···O inter-silanol distances (about 5.0 and 5.6 Å, respectively), very close to those for the cluster model adopted here. Moreover, the calculated ν(OH) frequencies for the SiOH pair are 3737 and 3733 cm^{-1}, with a frequency difference almost coincident with that recorded experimentally (i.e., 5 cm^{-1}). Additionally, to determine if the condensed α-quartz surface can host the ion/neutral reaction species, we have optimized the REACT structure to assess its structural stability. The optimized structure (see REACT-analogue of Figure 1B) shows a structure exhibiting the same H-bond patterns as those computed for the cluster model.

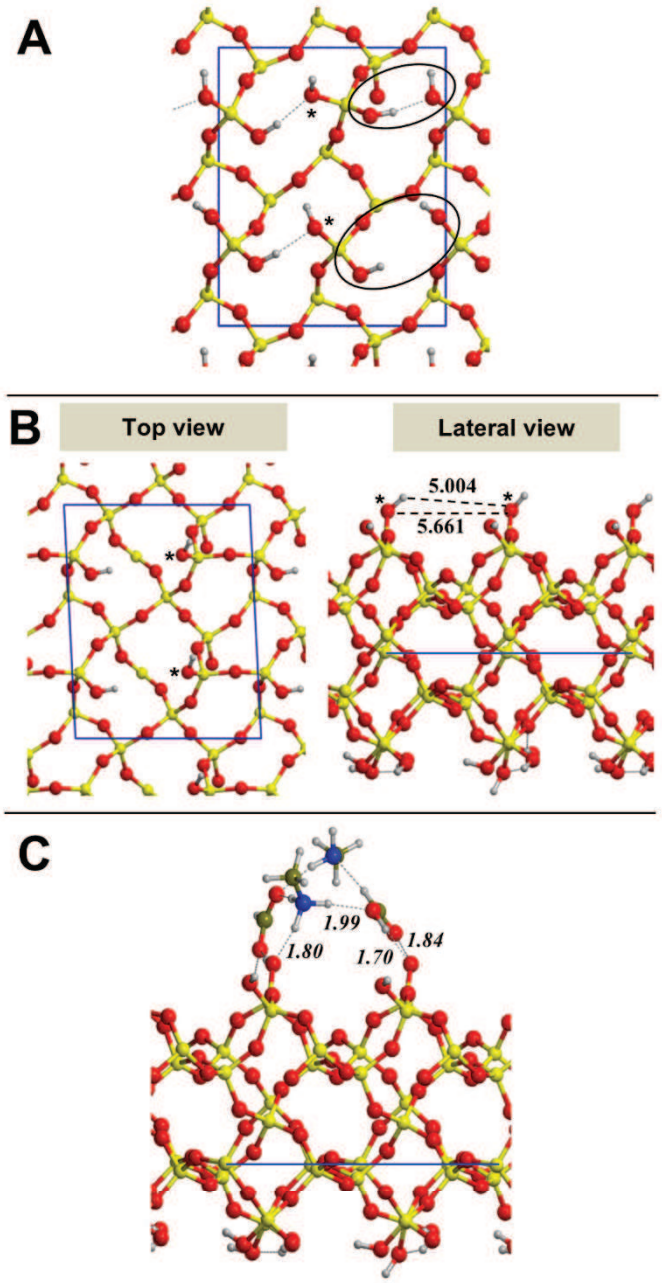

Figure 1. A) Top view of the crystalline (010) α-quartz surface in its pristine and condensed forms. The SiOH groups labelled by asterisk are those constituting the specific SiOH pair while the insets show the silanols to condensate and the resulting siloxane groups. B) Lateral view of the optimized geometry of the condensed (010) α-quartz surface (above), and optimized structure of the pre-reactant complex for AB formation (that is, the REACT-analogue) on the condensed (010) α-quartz surface, presenting the ionic and neutral forms of the FA/MA pairs (below). Bond distances are in Å. Unit cell borders are highlighted in blue.

In view of these results, we argue that other common silica forms with moderate degree of surface hydroxylation can exhibit similar catalytic activity towards the AB formation to that proved by our amorphous silica sample. This last result points out that the presence of the specific SiOH group pairs is not exclusive of the silica sample employed, but they can also be present in natural common forms of silica polymorphs present in early Earth, so that they may have behaved as a cradle for the prebiotic amide bond formation.

Oligomerization of glycine on α-quartz. An experimental approach

The reaction of amide bond formation just discussed prepares the ground to address the reaction of amino acids with quartz materials. Here, another tile is added to the mosaic of prebiotic chemistry, in terms of investigation of the reactivity of glycine adsorbed from the vapour phase on the surface of α-quartz particles with sub micrometric size. Gly was among the products of the Miller experiment, which examined the production of amino acids under possible primitive Earth conditions, [5] and it has been considered a reference molecule in a large number of experimental and theoretical investigations regarding the adsorption of amino acids onto mineral matter. [6-8]

The material: sub-micrometric particles of α-quartz

The employed material is a sub-micrometric α-quartz (hereafter αQz) which has been synthesized and characterized using the method established by Pastero et al. [9]. Briefly, sodium metasilicate is dissolved in deionized water under continuous stirring to obtain a 25 % w/w solution, then HNO_3 is added drop by drop until a pH value around 10 – 11 and the gel starts to form. The crystallization is carried out in a sealed autoclave at 210 °C for 120 hours, then filtered and purified with water and dried at 60 °C. The final material is a white powder exposing a specific surface area of 5.8 m^2/g (BET, Kr at 77 K). The XRD pattern of the obtained powder shown in Figure 2 fully correspond to that expected for α-quartz (JCPDS standard pattern number 46-1045). The diffraction peaks are indexed on the basis of the structure data of Kihara et al. [10]

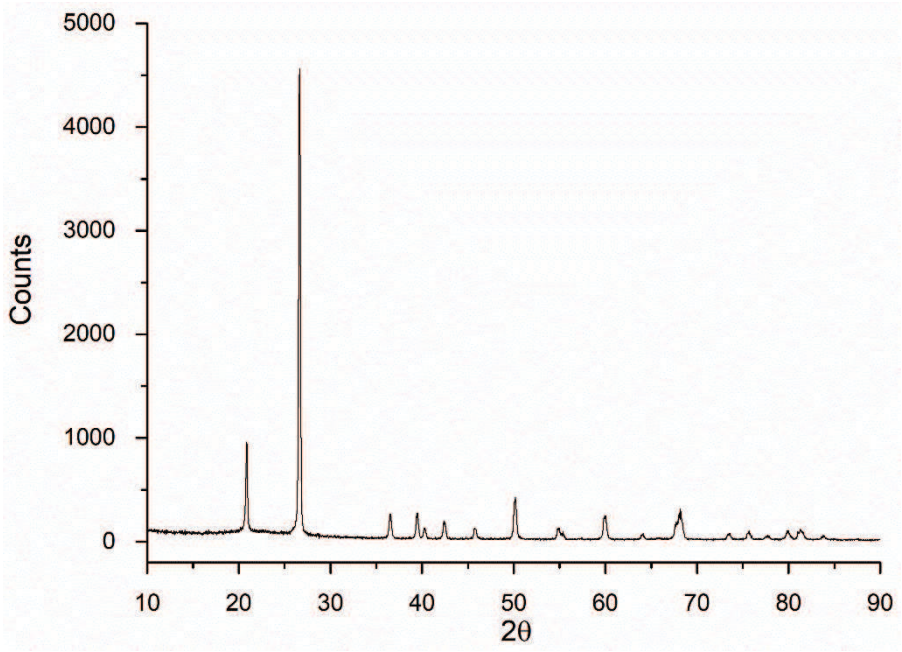

Figure 2. XRD pattern of the α-quartz powder produced.

Moreover, morphological and dimensional aspects of the quartz particles were inspected by field emission scanning electron microscopy. Figure 3 shows a representative image of the sample that appears constituted by primary particles of ca. 500 nm in size on average. The agglomeration of these particles is not representative of the actual state of the material because it can simply result from the deposition of the powder on the sample holder. Nevertheless, the fact that the powder is actually constituted by particles with size corresponding to that of primary particles observed in SEM images was obtained by dynamic light scattering (DLS) measurements providing a hydrodynamic diameter of ca. 450 nm. The particle size measured by both SEM and DLS is fully consistent with the measured SSA.

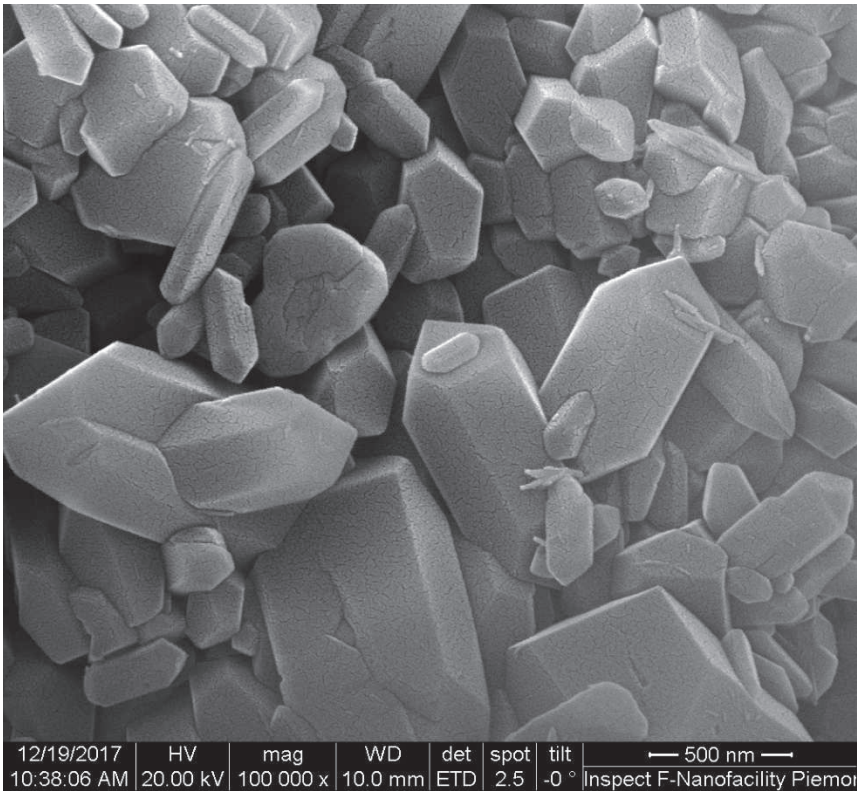

Figure 3. FE-SEM image representative of the αQz powder produced.

Glycine adsorption on silicas by chemical vapour deposition

Adopting the same concept of the previous study, where acids and amines are adsorbed from vapour phase on the surface of silica, here the chemical vapour deposition is employed. This procedure was developed by Martra et al. [11] in a work on the adsorption of glycine (Gly) on amorphous silica. Briefly, the amino acid and the oxide pellets are placed close to each other within a section of an infrared cell, acting as a reactor, and heated up in static vacuum to the sublimation temperature of the amino acid. A liquid nitrogen trap is present during the whole sublimation process in order to remove generated water from the system. Typical sublimation steps can last from 20 to 60 minutes and can be repeated until the amino acid pellet is consumed. Here, Gly sublimations are carried out at 403 K. Once sublimation process is complete, the samples are removed from the cell, manually ground in an agate mortar and suspended in 0.5 mL of Milli-Q water (Millipore system). The suspension is shaken for 15 min by a Vortex mixer and then centrifuged for 5 min at 10k rpm. After removal of the supernatant, the solid is

treated a second time with the same volume of water. The two aliquots of the aqueous solutions are then mixed, and analyzed by electrospray ionization mass spectrometry (ESI-MS). These experimental sequence was repeated on three different samples of the α-quartz powder produced.

Analysis of the products of the glycine-silicas interaction

Differing from the case of amorphous silica, α-quartz particles were not transparent to the IR radiation, thus it has not been possible to monitor the possible formation of reaction products on the surface of these particles, by *in situ* infrared spectroscopy. So, the only analytical technique able to provide information on the reaction products was the mass spectrometry of washing solutions.

For the sake of completeness the results obtained by adsorbing Gly vapours on α-quartz and the commercial pyrogenic silica Aerosil OX 50, object of the previous Gly on silica studies, [11] are here compared in Figure 4. The m/z pattern reported for the washing solutions of α-quartz contacted with Gly is the average of the results obtained for three different samples (HRMS data are reported in Figure A1 in the Appendix).

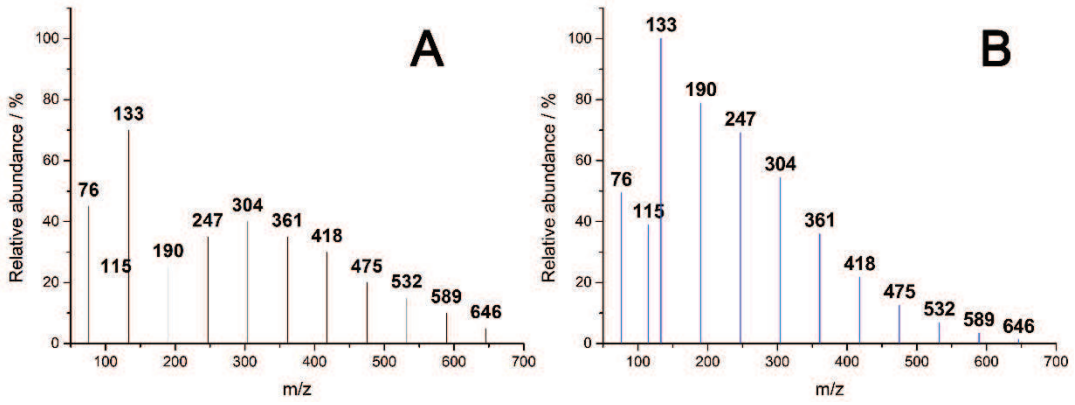

Figure 4. ESI-MS spectra of solutions resulting from washing (with pure water) of AOX50 (panel A) and αQz (panel B) contacted with Gly vapours for 30 minutes. Numbers on the bars are the *m*/*z* values of (-Gly-)$_n$ peptides.

The relevant insight provided by this comparison is the equivalent capability of both amorphous and crystalline silica surfaces of catalyse the formation of Gly oligopeptides long up to 11 terms. On one hand, this result reinforces the correctness of using amorphous silica particles as model materials for the study of

the interaction of amino acids with oxides mineral surfaces. On the other hand, it stimulate the prosecution of the study of the interaction/reaction of amino acids on α-quartz sub-micrometric particles, resulting in the production of polypeptides in amounts large enough to be detected. In this respect, efforts will be done in setting up experimental conditions allowing to record infrared spectra of molecules of polypeptides still at the surface of the α-quartz particles, targeting in particular their behaviour in dependence of the subsequent surface hydration. When applied in the case of Gly on amorphous silica, this method allowed to monitor the occurrence of interesting self-assembling phenomena among poly-glycine chains. [11] In the two m/z pattern relevant differences in the elative intensity of the signals due to peptides with different length are present. In the case of Gly on amorphous silica (panel A) the distribution is peaked on the 5-mer, whilst for Gly on α-quartz the most abundant peptide is the linear dimer. This differences could be due to the different morphology of the two types of surfaces but it cannot be excluded that other physical phenomena like diffusion of the amino acid vapour within the self-supporting pellet of the two types of silica could have played a role.

Beyond the simplest amino acid: alanine adsorption on amorphous and crystalline silicas

The success of the oligomerization of Gly on α-quartz particles encourages the extension of the investigation to the interaction of amorphous and crystalline silica particles with another amino acids. As in the recent study by Greenwald et al., [12] where the formation of long poly-alanines was attained by treating a solution of the amino acid with an excess of carbonyl sulphide, Ala was selected for this investigation for it is the simplest chiral amino acids and thus probably the most likely present in the prebiotic era. The experimental procedure was the same that in the case of the Gly/silica interaction, except that the temperature required for the sublimation of Ala is 443 K.

In Figure 5, a comparison between the m/z pattern of washing solutions containing the products of the reaction of alanine adsorbed on the amorphous pyrogenic silica Aerosil OX 50 (panel A) and on α-quartz sub micrometric particles (panel B) is reported. It can be observed that also for this amino acid, long oligopeptides up to 10-mers were produced. Such length is comparable to the 15-mer of the poly-alanine chains obtained by Greenwald et al. [12] by treating a solution of Ala with COS. Thus, the results obtained by CVD absorption of Ala on silica indicated that also the

polymerization of Ala on minerals could have contributed to the formation of long oligopeptides of these amino acids in prebiotic conditions.

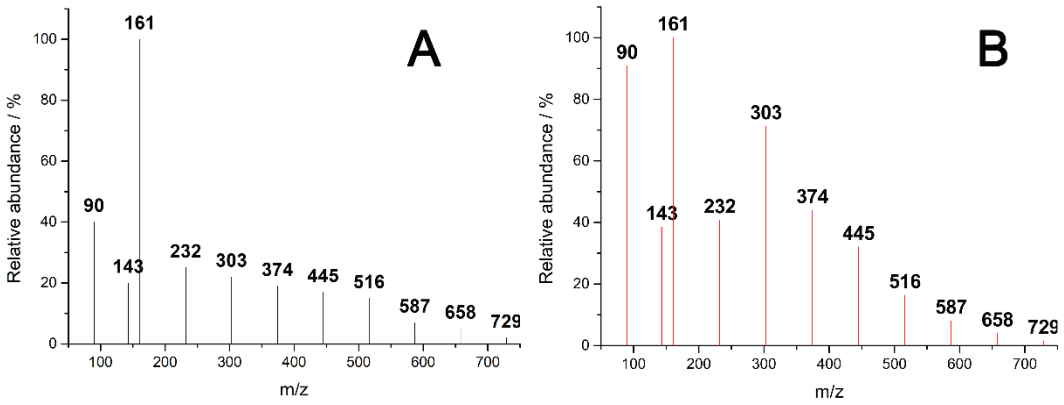

Figure 5. ESI-MS spectra of solutions resulting from washing (with pure water) of AOX50 (panel A) and αQz (panel B) contacted with Ala vapours for 30 minutes. Numbers on the bars are the *m*/*z* values of (-Ala-)$_n$ peptides.

The next step of this investigation will be the production of poly-Ala on the surface of amorphous and crystalline silica starting from L-Ala or D-Ala, in amounts large enough to allow the separation of the different oligomers and the analysis of the solution by CD-UV spectroscopy in order to investigate their chiral features. The final target is the investigation of the possible effect of amorphous and crystalline surfaces on the stereochemistry of the peptides produced.

Conclusions

The results collected in this chapter showed that the particular silanol pair, active toward the amide bond formation, found on amorphous silica surface, is a feature that can be also found on crystalline quartz. Here, the amidation reaction between methylamine and formic acid can occur as modelled. From the experimental point of view, an α-quartz material was employed to study the formation of peptides of Gly and Ala via the gas phase adsorption of non-activated amino acids. The results show the formation of homo-peptides up to 10 units long, where the chiral properties of Ala allow further investigations on the chirality of the surface processes concerning the peptide bond formation promoted by silica silanols.

Experimental Details

Sublimation of amino acids

The cell with the treated SiO_2 is transferred into a nitrogen filled glovebox for the introduction of the amino acids. The amino acids powders are compressed as well into self-supported pellets (ca. 150 mg) and moved close to the SiO_2 pellet. The cell is then connected to a vacuum line for the subsequent sublimation process where the SiO_2/amino acid system is outgassed. The sublimation process is the same already described by Martra et al. [16] in their SI for the glycine amino acid. Briefly, the amino acid and the oxide pellets are placed close to each other within a section of the infrared cell, acting as a reactor, and heated up in static vacuum to the sublimation temperature of the amino acid. A liquid nitrogen trap is present during the whole sublimation process in order to remove generated water from the system. Typical sublimation steps can last from 20 to 60 minutes and can be repeated until the amino acid pellet is consumed.

Products extraction and Mass Spectrometry analysis

At the end of the spectroscopic measurements, the samples were removed from the cell, manually ground in an agate mortar and suspended in 0.5 mL of Milli-Q water (Millipore system). The suspension was shaken for 15 min by a Vortex mixer and then centrifuged for 5 min at 10k rpm. After removal of the supernatant, the solid was treated a second time with the same volume of water. The two aliquots of the aqueous solutions were then mixed, and analyzed by high-resolution mass spectrometry.

High-resolution mass spectrometry analyses of the washing solutions were performed using an LTQ Orbitrap mass spectrometer (Thermo Scientific) equipped with an atmospheric pressure interface and an electrospray ionization (ESI) source. The source voltage was set to 4.48 kV. The heated capillary temperature was maintained at 538 K. The tuning parameters adopted for the ESI source were: capillary voltage 0.02 V, tube lens 24,77 V; for ions optics: multipole 0 offset −4.28 V, lens 0 voltage −4.36 V, multipole 0 offset −4.28 V, lens 1 voltage −13.69 V, gate lens voltage −8.84 V, multipole 1 offset −18.69 V, front lens voltage −5.09 V. Mass accuracy of recorded ions (vs calculated) was ± 1 mmu (without internal calibration). Samples, added of 100 μL of a 0.1 M HCOOH aqueous solution, were delivered directly to the mass spectrometer via a Hamilton microliter syringe at constant flow (10 μL/min).

References

[1] Rudnick R. L. and Gao S. *Composition of the Continental Crust* in Treatise on Geochemistry, K. K. Turekian Eds. **2003** (Pergamon, Oxford).
[2] Hystad G., Downs R. T., Hazen R. M. and Golden J. J. *Math. Geosci.* **2017** (49) 179-194.
[3] Musso F., Sodupe M., Corno M. and Ugliengo P. *J. Phys. Chem. C* **2009** (113) 17876-17884.
[4] Dovesi R., Orlando R., Erba A., Zicovich-Wilson C. M., Civalleri B., Casassa S., Maschio L., Ferrabone M., De La Pierre M., D'Arco P., Noël Y., Causà M., Rérat M. and Kirtman B. *Int. J. Quantum Chem.* **2014** (114) 1287-1317.
[5] Miller S. L. *Science* **1953** (117) 528-529.
[6] Lambert J.-F. *Origins Life Evol. Biospheres* **2008** (38) 211-242.
[7] Rimola A., Costa D., Sodupe M., Lambert J.-F. and Ugliengo P. *Chem. Rev.* **2013** (113) 4216-4313.
[8] Lambert J.-F., Stievano L., Lopes I., Gharsallah M. and Piao L. *Planetary and Space Science* **2009** (57) 460-467.
[9] Pastero L., Turci F., Leinardi R., Pavan C. and Monopoli M. *Cryst. Growth Des.* **2016** (16) 2394-2403.
[10] Kihara K. *European Journal of Mineralogy* **1990** (2) 63-77.
[11] Martra G., Deiana C., Sakhno Y., Barberis I., Fabbiani M., Pazzi M. and Vincenti M. *Angew. Chem. Int. Ed.* **2014** (53) 4671-4674.
[12] Greenwald J., Friedmann M. P. and Riek R. *Angew. Chem. Int. Ed.* **2016** (55) 11609-11613.

Appendix

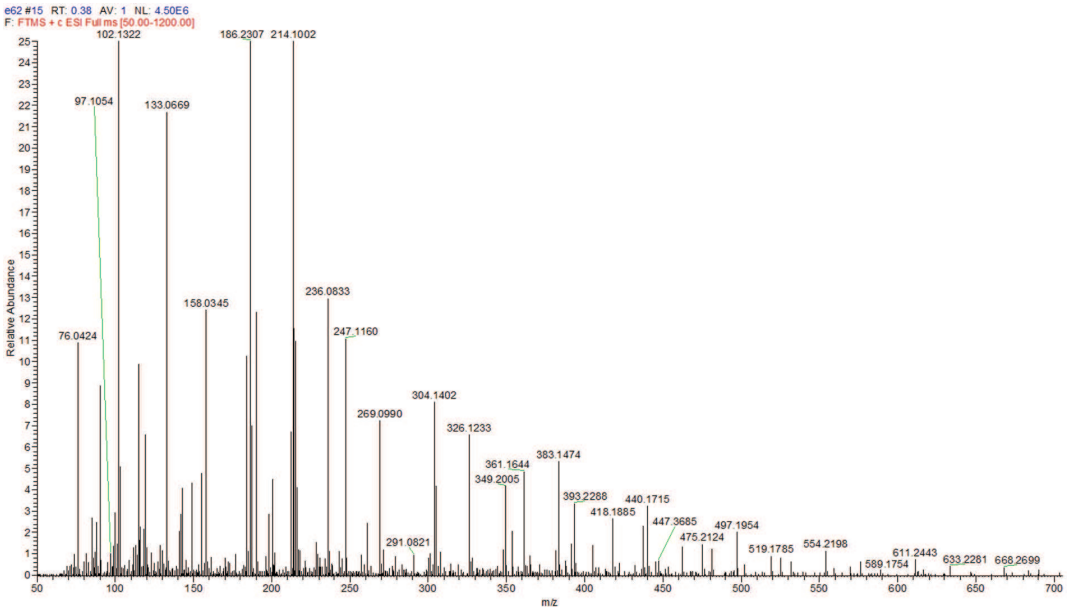

Figure A1. HR-MS spectrum (50 – 700 m/z) of the aqueous solution resulting from washing an α-quartz sample contacted with Gly vapours for 30 minutes.

Chapter Three

Abiotic formation of oligopeptides on TiO_2 nanoparticles

The oligomerization of non-activated amino acids catalyzed by nanostrucrured mineral oxide surfaces holds promises as a sustainable route for the industrial production of polypeptides. To analyze the influence of the surface type on the catalytic process, via a mild Chemical Vapor Deposition approach, the oligomerization of Glycine is performed on two samples of TiO_2 nanoparticles characterized by different relative amounts of defective surface terminations. Based on infrared spectroscopy and mass spectrometry data, the formation of peptide bonds on titania nanoparticles does not require highly energetic surface terminations, but can also occur on the most abundant and thermodynamically most stable {101} facets of nanosized anatase.

Amino acids vs. surface

The formation of peptides in mild conditions from non-activated amino acids is an intriguing chemical process potentially providing fundamental insight on the formation of the first biomolecules in abiotic conditions. [1, 2] Additionally, this type of reactions is a relevant proof-of-principle when investigating innovative sustainable routes for the production of peptides and polypeptides of interest in fine chemistry. [3, 4] The thermal condensation of non-activated amino acids was found to be effective under non catalytic anhydrous conditions by using trifunctional amino acids crystals mixtures. [5] When considering a possible influence of the mineral surfaces, Bernal's hypothesis accounts for the potential role of prebiotic surfaces to concentrate and catalyse the amino acids condensation. [6] In this respect, the interaction of both activated and non-activated amino acids with the surface of various solids have been studied [2, 7, 8] and oxide materials received particular attention. [8-12] Independently on the nature of the catalyst, a common difficulty still remains in the production of long oligopeptides when using non-activated amino acids, typically resulting in the production of short oligomers limited to 6 units. [13, 14] However, in 2014 Martra et al. successfully developed an efficient chemical vapour deposition method to obtain at mild conditions (433 K) homopeptides long up to 16 units from non-activated glycine (Gly) when sublimated on amorphous silica and titania. [15] These oxides were used in the form of nanoparticles, thus exposing a specific surface area (SSA) high enough to allow the process to proceed effectively. Nevertheless, nanosizing not only increases the

surface/bulk atom ratio, but also the proportion of surface atoms on low energy facets and those on more energetic facets and on edges and corners. Noticeably, surface sites in these three last locations are the most chemically active, because of their peculiar electronic and coordinative state. [16, 17] This would imply a limited number of surface catalytic active sites, which could be beneficial for selectivity, but detrimental for conversion. In the case of the formation of polypeptides in prebiotic conditions, this aspect could represent an additional factor decreasing the probability of the occurrence of the reaction of interest at the surface of minerals. On the other hand, also the technological exploitation of peptide synthesis catalysed by oxide nanoparticles could benefit by the absence of constraints dealing with the presence of peculiar surface sites.

The scientific motivation of this part was actually to address such a question, namely - Are minority sites at oxides surfaces required for the peptide bond formation? A general answer would require the investigation of different types of oxides nanomaterials, covering the whole spectrum of chemical bonding in solids ranging from fully ionic to fully covalent. As a first contribution to answering the question above, we tested the oligomerization of Gly on two types of TiO_2 nanoparticles (hence a semiconducting material with an ionic-covalent bond character) selected based on their different relative amount of {101} facets, the most thermodynamically stable [18] and more defective surface terminations.

Titania surface characterization

Shape-controlled TiO_2 nanoparticles lab-prepared by hydrothermal synthesis (100% anatase, SSA_{BET} ~ 42 $m^2\ g^{-1}$, hereafter TiO_2 HT) [19] and commercial TiO_2 P25 (by Evonik, ~80 % anatase and ~20 % rutile w/w, purity ≥ 99.5 wt%, SSA_{BET} ~ 50 $m^2\ g^{-1}$) were used. Previous investigations demonstrated that the rutile phase account only for ca. 7 % of the SSA of TiO_2 P25. [20] Representative HR-TEM high magnification images of the borders of the two types of nanoparticles are shown in Figure 1. In both cases, {101} lattice fringes are present, running parallel to the main borders which in the case of TiO_2 P25 appear heavily stepped (panel A), whereas for TiO_2 HT are quite flat and regular. These features can be extended to {101} facets: because of the 2D projection character of TEM, and the extremely short wavelength of the electron beam used for imaging (microscope Jeol 3010 operated at 300 kV), borders parallel to lattice fringes due to a crystallographic planes family correspond to the profile of facets terminated by those planes. Although informative, TEM inspection cannot easily provide insight on all types of surface terminations and their relative

abundance, thus the surface features of the two types of TiO_2 nanoparticles are investigated by IR spectroscopy of adsorbed CO (Figure 2), being this molecule a highly sensitive probe to the coordinative state of surface Ti^{4+} ions. [19, 21] Before CO adsorption, titania nanoparticles were outgassed under high dynamic vacuum (residual pressure: $1 \cdot 10^{-5}$ mbar) and re-oxidized at the same temperature by contact with O_2 at 10 mbar in order to obtain an highly de-hydroxylated and fully dehydrated surface. [22]

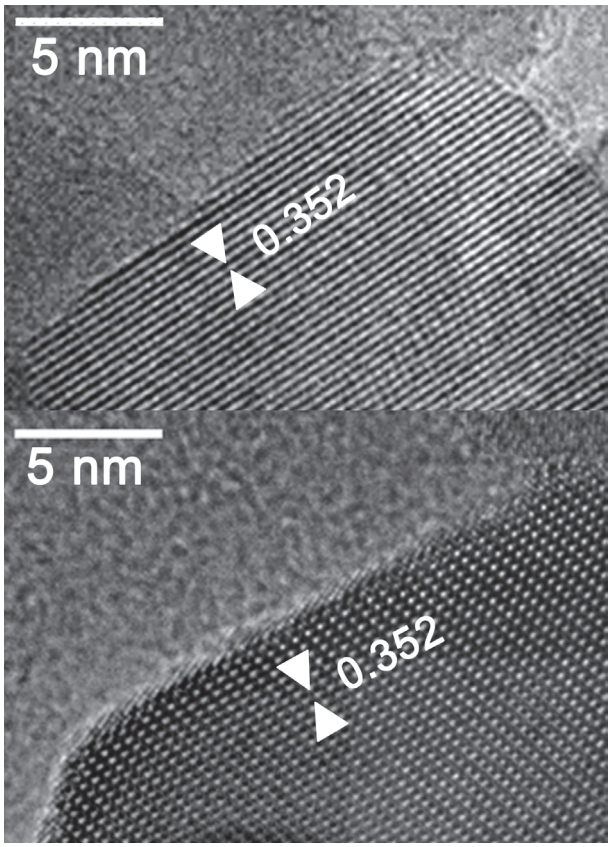

Figure 1. HR-TEM images of TiO_2 P25 (panel A) and TiO_2 HT (panel B); original magnifications: x500 k and x800 k respectively. The interfringes distance of 0.352 nm corresponds to the distance between {101} crystal planes in anatase TiO_2 (ICDD 00-021-1272).

The spectrum of CO at 45 mbar is dominated by the peak at 2179 cm^{-1} for TiO_2 P25 (panel A) and 2178 cm^{-1} for TiO_2 HT (panel B) typical of these probe molecules adsorbed on {101} TiO_2 anatase surfaces, where Ti^{4+} ions are pentacoordinated. [20] The progressive up-shift of these signals by decreasing the CO coverage is due to the fading away of adsorbate-adsorbate interactions. [21] Moreover, in the case of

TiO_2 P25 also a heavy shoulder at 2183 cm^{-1}, due to the presence of CO on {110} TiO_2 anatase surfaces exposing tetracoordinated Ti^{4+} sites, [19] is present, as well as a very weak band at 2206-2208 cm^{-1}, indicating the presence of a few highly coordinatively unsaturated Ti^{4+} sites , generally called "α sites". [23, 24] The additional weak band at 2212 cm^{-1}, more sensitive to CO outgassing, is due to the combination of the internal stretching mode and a frustrated translational mode of CO molecules adsorbed on {101} surfaces. [25]

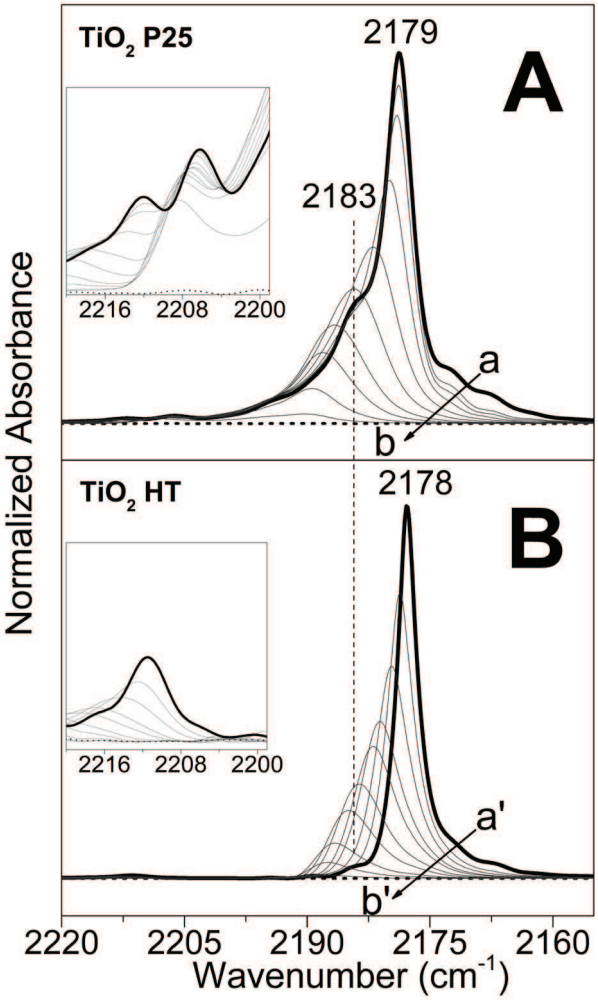

Figure 2. FT-IR spectra, in the νCO region, of TiO_2 P25 (panel A) and TiO_2 HT (panel B) outgassed and re-oxidized at 873 K and contacted at 100 K with decreasing CO pressures (from 45 mbar to complete outgassing; lettering in the sense of decreasing coverages). Spectra are reported in Absorbance, after having subtracted the spectra of titania nanoparticles before CO admission as a background.

Conversely, the spectra of CO adsorbed on TiO_2 HT appear definitely simpler, the main band due to CO on {101} facets being accompanied by a very weak signal due to CO on {110} terminations, while the component produced by CO on α sites is not detectable. Hence, these findings confirm and further underline that there is a significant difference in the surface structure of the two types of titania nanopowders: TiO_2 HT nanoparticles are overwhelmingly terminated by the most stable, highly regular {101} facets exposing pentacoordinated Ti^{4+} sites and two and three fold coordinated oxygen atoms, whereas TiO_2 P25 nanoparticles are also terminated by {110} surfaces, exposing tetracoordinated Ti^{4+} sites and two fold coordinated oxygen atoms, [26] and by a not negligible amount of α sites characterized by Ti^{4+} centres with a stronger Lewis acidity. [23, 24]

Amino Acid Sublimation

In summary, IR spectroscopy of adsorbed CO indicated that TiO_2 HT nanoparticles are overwhelmingly terminated by {101} surfaces, that, as observed by HR-TEM, [25] are the facets of highly regular truncated bipyramid nanoparticles, ca. 60 nm in length and ca. 30 nm wide. The large prevalence of {101} terminations revealed by IR spectra of adsorbed CO also for TiO_2 P25, and the similar specific surface area with respect to TiO_2 HT, allow to depict also these nanoparticles as truncated bipyramids similar in size to the previous ones, but exposing a significant extent of {110} facets at the intersection of {101} ones at the middle plan of bipyramids. IR spectroscopy in controlled atmosphere was also used to investigate the fate of Gly molecules adsorbed on titania nanoparticles from the vapour phase, using the protocol set up in a previous work. [15] Curves a in Figure 3 are the spectra of bare TiO_2 P25 and TiO_2 HT (panel A and B, respectively) outgassed at 433 K in order to dehydrate the nanoparticles. After such treatment, only the typical pattern due to surface OH groups is present in the 3800-3500 cm^{-1} range of the spectrum of TiO_2 P25, [26, 27] whilst for TiO_2 HT this pattern is accompanied by an intense narrow peak at 2345 cm^{-1} and a series of signals in the 1600-1250 cm^{-1} range, due to CO_2 molecules and carboxylates/carbonates species remained entrapped in the inner closed cavities formed in the bulk of nanoparticles during the synthesis. [20] When increasing amounts of Gly are adsorbed from the vapor phase on nanoparticles of both types, a typical pattern of polypeptides appears, with νNH amide bands in the 3500-3000 cm^{-1} and amide I and amide II signals at ca. 1670 cm^{-1} and 1560 cm^{-1},

respectively (curves b-c). In addition, the νCH_2 signals progressively grow in the 3000-2800 cm^{-1} range.

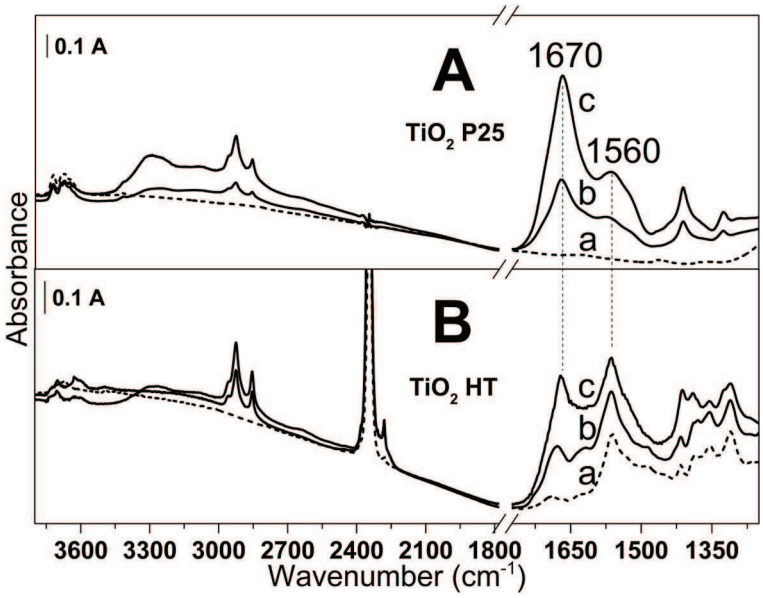

Figure 3. FT-IR spectra resulting from Gly adsorption from vapour phase on TiO_2 P25 (panel A) and TiO_2 HT (panel B). Curves a: TiO_2 nanoparticles dehydrated by outgassing at 433 K; curves from b to c: after contact with increasing doses of Gly vapours produced by sublimation at 433 K.

The Gly coverage was limited to ca. 60 % of Ti^{4+} surface sites, in order to avoid possible reactions among amino acid molecules not in interaction with the surfaces of nanoparticles. The coverage was monitored by exploiting a competitive assay with CO_2 dosed at room temperature as probe molecule of Ti^{4+} surface sites [15] (data not shown). Thus, both TiO_2 P25 and TiO_2 HT nanoparticles appeared able to catalyse the condensation among adsorbed amino acids. Noteworthy, a possible catalytic role of rutile nanoparticles in TiO_2 P25 appears not to be relevant, because of the appreciable reactivity already exhibited by pure anatase TiO_2 HT nanoparticles. The relevant but qualitative evidence of the equivalence in reactivity towards amino acids of the TiO_2 nanoparticles differing in surface texture was extended by determining the length of peptides species produced. To this aim, titania samples reacted with Gly are washed with water and the resulting solutions are analysed by HR-MS. Again, very similar results are obtained for Gly on TiO_2 P25 and TiO_2 HT (Figure 4): in both cases, oligomers long up to 16 units are detected with an overall m/z distribution peaked in correspondence of the Gly 4-mer (m/z = 247).

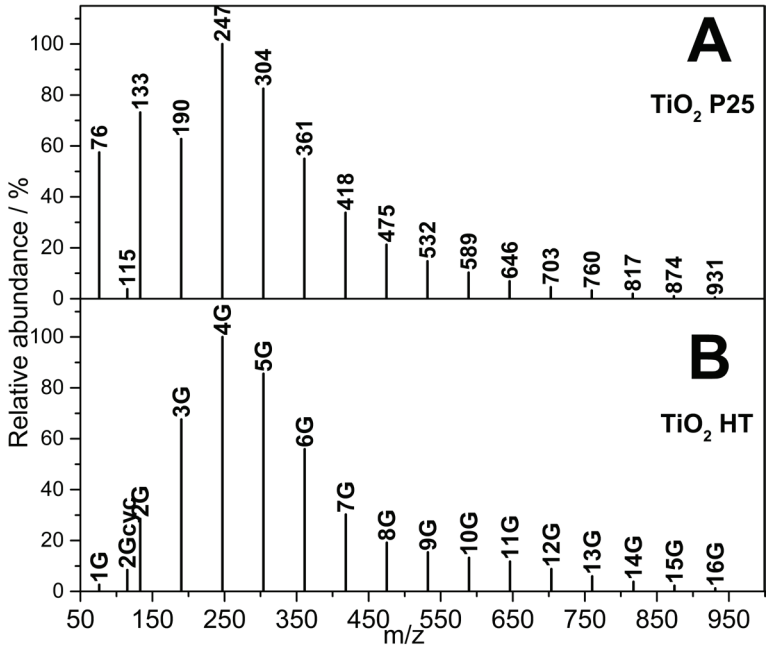

Figure 4. ESI-MS spectra of solutions resulting from washing (with pure water) of titania nanoparticles contacted with Gly vapors for 60 min. Panel A: TiO_2 P25; panel B: TiO_2 HT. Numbers on the bars in panel A are the m/z values (without decimal digits for the sake of clarity) of $(\text{-Gly-})_n$ peptides; labels on the bars in panel B are the number of terms in $(\text{-Gly-})_n$ peptides. The difference in m/z values between consecutive signals is 57, corresponding to a Gly peptide unit. Detection conditions resulted in the protonation of analyzed species (m/z values increased of one unit with respect to original analytes).

Difference in the relative amount of peptides shorter that 4-mer, as well as of the monomer, are present in the two cases. However, the established method and set up for the sublimation of amino acids and for the contact of their vapours with the nanoparticles does not allow, at present, a control of the reaction conditions fine enough to exclude other factors (different diffusion of amino acids molecules within the pellet of nanoparticles, small fluctuation of the temperature during sublimation) other than surface features played a role in determining the difference in relative amount of shorter oligomers and unreacted monomer.

Conclusion

The collection of data presented allows to conclude that the formation of peptide bonds from non-activated amino acids adsorbed on titania nanoparticles does not require surface sites on highly energetic surface terminations, but occurs on the most stable facets, which are also the most abundant ones. This conclusion might not be extended straightforwardly to other oxide catalysts with a significantly different chemical bond character, like silica, because the surface texture resulting from siloxane bridges and silanol groups might change the role of defective towards regular surface sites with respect to what here obtained for titania. Nevertheless, this finding appears to be relevant both for the elucidation of the catalytic role of nanosized minerals towards the formation of peptides in prebiotic era and for the possible technological exploitation of nanosized oxides as heterogeneous catalysts for the production of peptides. Difference in the catalytic activity of anatase TiO_2 nanoparticles toward non-activated amino acid condensation can be expected for nanoparticles with particular morphologies, resulting from preparation methods favoring the exposure of surface terminations different from the most stable {101} ones.

Experimental Details

Sublimation of amino acids

The cell with the treated TiO_2 is transferred into a nitrogen filled glovebox for the introduction of the amino acids. The amino acids powders are compressed as well into self-supported pellets (ca. 150 mg) and moved close to the TiO_2 pellet. The cell is then connected to a vacuum line for the subsequent sublimation process where the TiO_2/amino acid system is outgassed. The sublimation process is the same already described by Martra et al. [16] in their SI for the glycine amino acid. Briefly, the amino acid and the oxide pellets are placed close to each other within a section of the infrared cell, acting as a reactor, and heated up in static vacuum to the sublimation temperature of the amino acid. A liquid nitrogen trap is present during the whole sublimation process in order to remove generated water from the system. Typical sublimation steps can last from 20 to 60 minutes and can be repeated until the amino acid pellet is consumed. The very same process is also followed for the alanine sublimations.

Products extraction and Mass Spectrometry analysis

At the end of the spectroscopic measurements, the samples were removed from the cell, manually ground in an agate mortar and suspended in 0.5 mL of Milli-Q water (Millipore system). The suspension was shaken for 15 min by a Vortex mixer and then centrifuged for 5 min at 10k rpm. After removal of the supernatant, the solid was treated a second time with the same volume of water. The two aliquots of the aqueous solutions were then mixed, and analyzed by high-resolution mass spectrometry.

High-resolution mass spectrometry analyses of the washing solutions were performed using an LTQ Orbitrap mass spectrometer (Thermo Scientific) equipped with an atmospheric pressure interface and an electrospray ionization (ESI) source. The source voltage was set to 4.48 kV. The heated capillary temperature was maintained at 538 K. The tuning parameters adopted for the ESI source were: capillary voltage 0.02 V, tube lens 24,77 V; for ions optics: multipole 0 offset −4.28 V, lens 0 voltage −4.36 V, multipole 0 offset −4.28 V, lens 1 voltage −13.69 V, gate lens voltage −8.84 V, multipole 1 offset −18.69 V, front lens voltage −5.09 V. Mass accuracy of recorded ions (vs calculated) was ± 1 mmu (without internal calibration). Samples, added of 100 μL of a 0.1 M HCOOH aqueous solution, were delivered directly to the mass spectrometer via a Hamilton microliter syringe at constant flow (10 μL/min).

References

[1] S. L. Miller and J. L. Bada *Nature* **1988** (334) 609-611.
[2] J. P. Ferris, A. R. Hill, R. Liu and L. E. Orgel *Nature* **1996** (381) 59-61.
[3] V. R. Pattabiraman and J. W. Bode *Nature* **2011** (480) 471-479.
[4] M. Rodriguez-Garcia, A. J. Surman, G. J. T. Cooper, I. Suárez-Marina, Z. Hosni, M. P. Lee and L. Cronin *Nature* **2015** (6) 8385.
[5] S. W. Fox and K. Harada *J. Am. Chem. Soc.* **1960** (82) 3745-3751.
[6] J. D. Bernal *Proc. Phys. Soc., London, Sect. B* **1949** (62) 597-618.
[7] L. E. Orgel *Origins Life Evol. Biospheres* **1998** (28) 227-234.
[8] A. Rimola, D. Costa, M. Sodupe, J.-F. Lambert and P. Ugliengo *Chem. Rev.* **2013** (113) 4216-4313.
[9] M. Meng, L. Stievano and J.-F. Lambert *Langmuir* **2004** (20) 914-923.
[10] J. Bujdák and B. M. Rode *J. Mol. Evol.* **1997** (45) 457-466.
[11] P. Leyton, R. Saladino, C. Crestini, M. Campos-Vallette, C. Paipa, A. Berríos, S. Fuentes and R. A. Zárate *Amino Acids* **2012** (42) 2079-2088.
[12] S. Pantaleone, A. Rimola and M. Sodupe *J. Phys. Chem. C* **2017** (121) 14156-14165.
[13] J.-F. Lambert *Origins Life Evol. Biospheres* **2008** (38) 211-242.
[14] J. Bujdak and B. M. Rode *J. Mol. Evol.* **1996** (43) 326-333.
[15] G. Martra, C. Deiana, Y. Sakhno, I. Barberis, M. Fabbiani, M. Pazzi and M. Vincenti *Angew. Chem. Int. Ed.* **2014** (53) 4671-4674.
[16] H.-J. Freund *Faraday Discuss.* **1999** (114) 1-31.
[17] U. Aschauer, Y. He, H. Cheng, S.-C. Li, U. Diebold and A. Selloni *J. Phys. Chem. C* **2010** (114) 1278-1284.
[18] X.-Q. Gong, A. Selloni, M. Batzill and U. Diebold *Nat. Mater.* **2006** (5) 665-670.
[19] C. Deiana, E. Fois, G. Martra, S. Narbey, F. Pellegrino and G. Tabacchi *ChemPhysChem* **2016** (17) 1956-1960.
[20] C. Deiana, M. Minella, G. Tabacchi, V. Maurino, E. Fois and G. Martra *PCCP* **2013** (15) 307-315.
[21] K. I. Hadjiivanov and G. N. Vayssilov *Characterization of oxide surfaces and zeolites by carbon monoxide as an IR probe molecule* in Advances in Catalysis **2002** (Elsevier Academic Press Inc, San Diego)
[22] G. Martra *Appl. Catal. A-Gen.* **2000** (200) 275-285.
[23] C. Morterra *J. Chem. Soc., Faraday Trans. 1* **1988** (84) 1617-1637.
[24] K. Hadjiivanov, J. Lamotte and J.-C. Lavalley *Langmuir* **1997** (13) 3374-3381.
[25] C. Deiana, G. Tabacchi, V. Maurino, S. Coluccia, G. Martra and E. Fois *PCCP* **2013** (15) 13391-13399.

[26] C. Arrouvel, M. Digne, M. Breysse, H. Toulhoat and P. Raybaud *J. Catal.* **2004** (222) 152-166.
[27] C. Deiana, E. Fois, S. Coluccia and G. Martra *J. Phys. Chem. C* **2010** (114) 21531-21538.

Chapter Four

Amide bond formation on titania

The interaction of carboxyl groups with mineral surfaces is of key relevance in chemistry. Nevertheless, how formic acid adsorbs on the most abundant TiO_2-anatase facets is still controversial: whereas ab-initio structural optimizations predict molecular absorption, several experiments evidenced formic acid dissociation. In this chapter, by using IR spectroscopy and first principles molecular dynamics, evidence is provided of a fast equilibrium taking place, at the experimental room-temperature conditions, between formate and formic acid on anatase TiO_2 (101) facets. The microscopic process, a femtosecond-scale proton shuttling between the carboxyl group and the surface oxygen atoms, implies the coexistence of molecular formic acid and dissociated formate on anatase TiO_2 (101) under normal conditions. With this study, the aim is to sheds some light on the interactions of organic acids with titania and once more underlines the importance of the temperature variable in modeling approaches. Furthermore, these insights are a new starting point for the subsequent reaction of FA with MA.

Formic acid adsorption on TiO_2 (101)

Adsorption of organic molecules on TiO_2 lies at the basis of many applications in sustainable technologies. [1-9] Formic acid (HCOOH), as the simplest organic acid, is the choice candidate to explore how carboxylic groups interact with TiO_2 surfaces. This interaction governs both the anchoring of solar cell sensitizers [10-15] and the interfacial transfer of photogenerated reactive species, a key step in heterogeneous photocatalytic processes. [16, 17] Additionally, oxide surfaces activate the –COOH group towards amidation through a direct, atom-economical route under environmentally benign conditions. [18-25] In this context, "amide-bond formation avoiding poor atom-economy reagents" was voted by the American Chemical Society as the top priority towards more-sustainable reagents and methods. [23] Indeed, the most stable and abundant [24-26] {101} anatase surfaces [27] in TiO_2-based industrial catalysts [28] can trigger both the amidation reaction between formic acid and 1-pentanamine, [18] and the oligomerization of amino acids under possible primitive Earth conditions. [29] Understanding how these common, non-toxic mineral surfaces do succeed in activating the carboxylic group at mild

conditions would be a substantial asset for both sustainable and prebiotic chemistry. Unfortunately, not only the catalytic action of the anatase surface remains unexplained, but also the initial adsorption process is still far from being understood. First-principles modeling of HCOOH on clean, regular TiO_2 (101) surfaces predict that the most stable structure is non-dissociated formic acid in a monodentate adsorption geometry, *i.e.,* with the carbonyl group on top of a Ti-Lewis acid site, and the hydroxyl group hydrogen bonded to an adjacent surface oxygen (Brønsted base site). [24, 30] A bidentate structure deriving from dissociative adsorption is, however, only slightly less stable; [13] moreover, co-adsorption, solvation, surface curvature and protonation state may affect significantly the relative stability of the dissociated and undissociated configurations. [31-34] This holds true for acetic acid [35] and Ru(II)-sensitizers for anatase nanoparticles as well. [15] Experimental studies display an even more puzzling scenario. Infrared reflection absorption spectroscopy (IRRAS) data on anatase-TiO_2 single crystals indicate that gaseous HCOOH dissociates in monodentate formate on non-defective {101} facets. [36] The fate of the detached carboxyl proton is however unclear, as no surface OH stretching signal was detected in the IRRAS experiments. [36] Similar conclusions were drawn for acetic acid on anatase TiO_2 {101} by Scanning Tunneling Microscopy: molecular monodentate and dissociative bidentate were proposed as the most likely binding modes at low coverages, but no hydrogen atoms derived from carboxyl deprotonation were detected. [37] Also the general picture emerging from experiments is quite different from that predicted by modelling. Although it is well established that simple organic acids adsorb dissociatively on rutile TiO_2 (110), [38-45] there is still "conflicting experimental and theoretical evidence for the adsorption of carboxylic acids on the {101} surface of anatase". [33, 37]

Whereas the above-mentioned modeling studies are mainly energy minimizations - resulting in static, zero-temperature structures, infrared measurements are carried out at finite temperature, on samples heated by the IR beam. Since thermal effects are instrumental in modeling molecular behavior on oxide surfaces, including anatase TiO_2, [35, 45-51] here IR spectroscopy is used, geometry optimizations (0 K) and finite temperature (300 K) molecular dynamics simulations to solve the problem. The experimental and theoretical pictures of HCOOH-adsorption on anatase-TiO_2 are only in apparent contrast, and that "temperature" is the keyword that settles the issue and clarifies the fate of the detached proton.

IR experiments are performed to investigate the adsorption of either HCOOH or HCOOD, at different coverage, on TiO_2 P25 nanoparticles, which are known to catalyze the amidation reactions from formic acid and 1-pentanamine. [18] The adsorption of a first small dose of HCOOH (Figure 1, curve b, top panel) resulted in the appearance of two sets of signals in the 1650-1300 cm^{-1} range. The band centered at 1558 cm^{-1} can be attributed to the antisymmetric stretching mode of $–COO^-$ groups, with the symmetric partner one at 1412 cm^{-1} and 1364 cm^{-1}, each of them likely due to formate species with a different coordination to the surface. [18] In addition, the component at 1385 cm^{-1} is attributed to the O-C-H deformation mode of formates. [36, 52, 53] At higher frequency, the typical pattern in the 3000-2700 cm^{-1} range due to the CH stretching mode of formate appeared, whereas neither significant changes of the spectral pattern due to surface hydroxy groups occurred, nor new OH stretching signals resulting from the transfer of protons from adsorbed molecules and surface oxygen atoms were detected. This is in agreement with the finding by Xu et al., who did not observe any signal of the OH stretching mode resulting from dosing HCOOH on {101} anatase single crystal. [36]

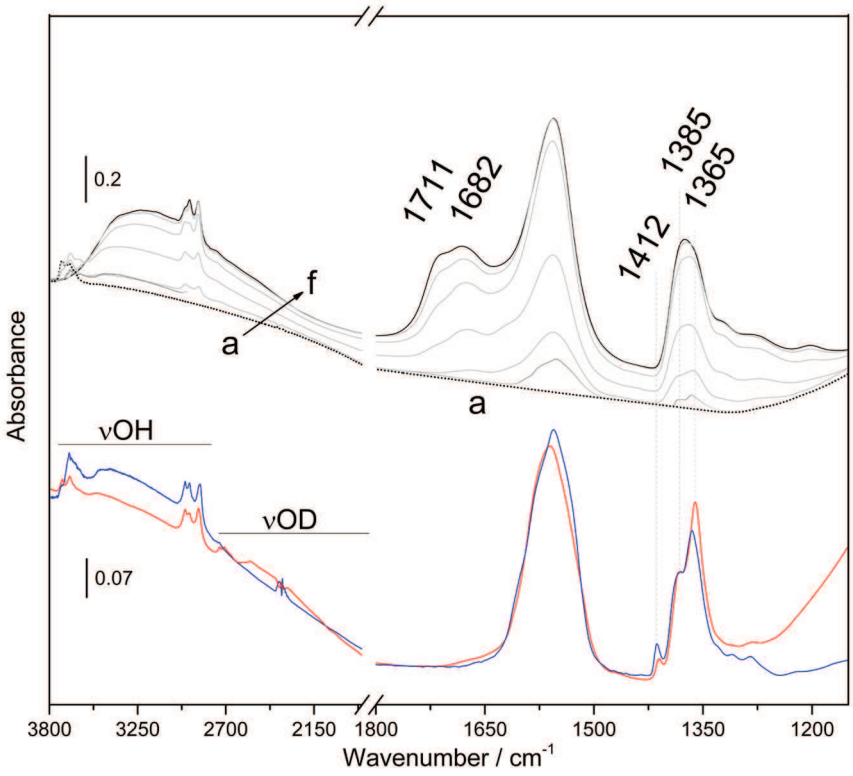

Figure 1. Top: IR spectra of TiO_2 nanoparticles pre-outgasses at 723 K (curve a) in contact with increasing formic acid doses (curves b - f). Bottom: Comparison of IR spectra obtained at small dosage of HCOOH (red line) and HCOOD (blue line).

By admitting further doses of formic acid (curves b – f), the bands due to formate species grew in intensity, but a new band appeared at 1682 cm^{-1} accompanied by a shoulder on the high frequency side progressively gaining in relative intensity by increasing the coverage and finally located at 1711 cm^{-1}. In terms of frequency groups, the first signal can be assigned to the νC=O of HCOOH molecularly adsorbed on the surface, whilst the second one is attributed to multilayers of formic acid adsorbed in a liquid-like form. in line with previous studies on TiO_2-P25 [32] and other TiO_2 nanoparticles. The –CH moiety of progressively added formic acid molecules contributed to the growth of the pattern in the 3000-2700 cm^{-1} range, which appeared overlapped to a very broad absorption, progressively increasing in intensity and spreading over the 3650-2000 cm^{-1} range. Such broad signal is due to the stretching mode of hydroxy groups involved in hydrogen bonding, belonging either to carboxylic groups or to surface Ti-OH indeed, the original νOH signals of the latter is downshifted and contributes to the broad absorption band. To obtain

additional insights on the possible deprotonation of formic acid molecules when adsorbed in very low amount on the TiO_2 surface (curve a), in a separate experiment, a very small dose of HCOOD was admitted on a TiO_2 sample pre-outgassed at 723 K. The spectrum obtained is shown in Figure 1 (bottom panel), compared with the equivalent one resulting from the adsorption of HCOOH. The two spectra exhibited only minor differences in the 1750-1300 cm^{-1} range, whereas a significant part of the original νOH spectra profile in the 3650-2700 cm^{-1} range was converted in a 2700-2100 cm^{-1} νOD pattern. This behavior indicates that deuterons originally belonging to HCOOD molecules were able to participate to a H/D exchange with surface hydroxy groups.

To identify on which anatase facet formic acid was adsorbed, [54] is analyzed the adsorption of CO on the samples. [46, 55, 56] Carbon monoxide - a probe molecule sensitive to different type of TiO_2 surface terminations [46, 51, 57] - was adsorbed at ca. 100 K on titania nanoparticles in their bare form (after outgassing at 723 K) and with adsorbed formate species. Results are depicted in Figure 2. The main peak at 2179 cm^{-1} due to CO on bare titania nanoparticles is due to probe molecules adsorbed on anatase {101}, while the weak signals at 2165 cm^{-1} and 2136 cm^{-1} are attributed to CO adsorbed on anatase {100} and/or {001} facets and physisorbed in a liquid-like form, respectively.[46] Noticeably, the peak at 2179 cm^{-1} appeared significantly decreased in intensity when CO was admitted on TiO_2 nanoparticles with pre-adsorbed HCOOH, clearly indicating that formate-like species were formed on {101} surfaces.

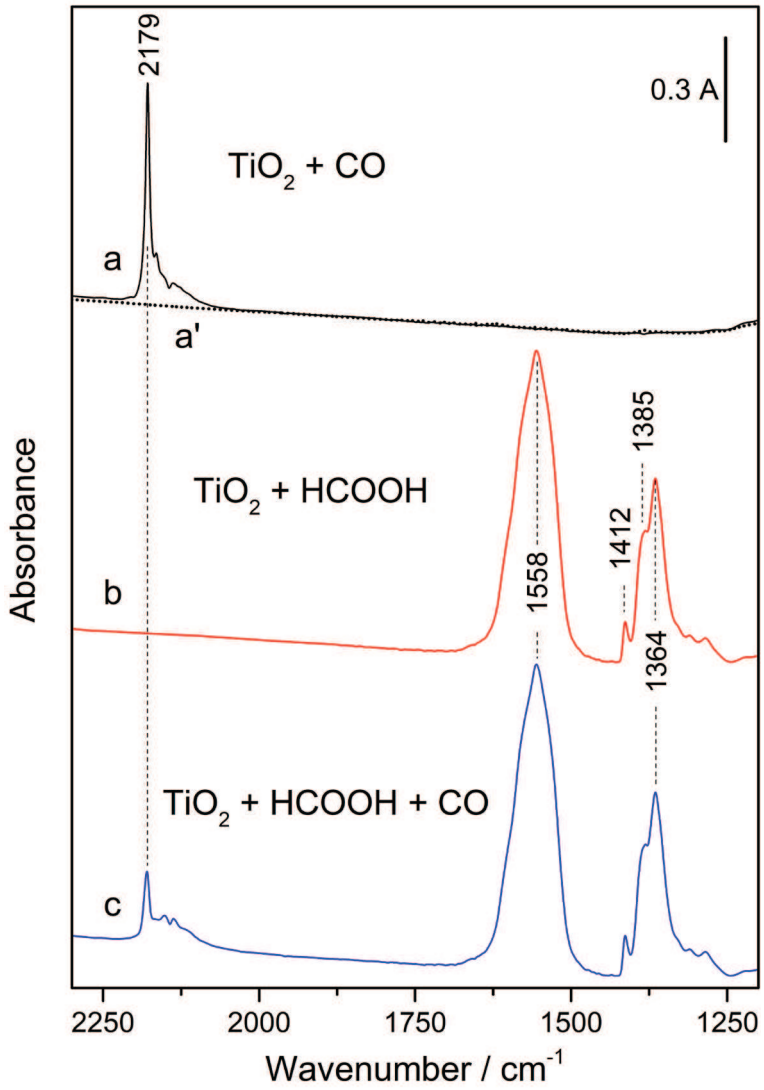

Figure 2. CO adsorption on HCOOH preadsorbed on activated TiO_2. 100 Torr CO adsorbed (curve a') on activated TiO_2 surface (curve a), HCOOH adsorbed on activated TiO_2 surface (curve b), 100 Torr CO contacted with preadsorbed formic acid (curve c) on TiO_2 surface.

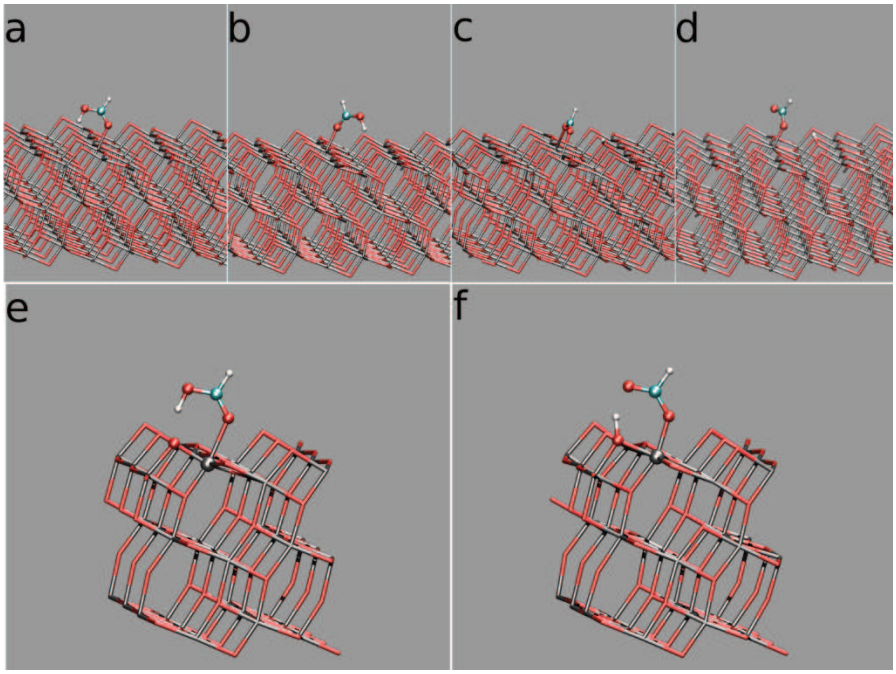

Figure 3. a-d: Optimized structures of HCOOH on anatase-TiO_2 (101). a: Mol0, b: Mol1, c: Dis2, d: Dis3. e,f: Snapshots from the 300 K trajectory of deuterated formic acid on anatase-TiO_2 (101). e: molecularly adsorbed DCOOD; f: dissociatively adsorbed DCOOD. Atom colors: red = O; gray = Ti; cyan = C; H/D = white.

Quite a different picture emerged from the geometry optimizations, which predicted a non-dissociated monodentate structure as the most stable adsorption geometry. Four different structures were found for the adsorption of HCOOH on our slab model: two molecularly adsorbed (Mol0, Mol1) and two dissociated (Dis2, Dis3), shown in Figure 3a-d. The two molecularly adsorbed structures, nearly degenerate, were the most stable ones, see Table 1. The dissociative bidentate structure (Dis2) was only slightly higher in energy than Mol0 and Mol1, and more stable than the dissociative monodentate geometry (Dis3), in agreement with previous modeling studies. [24, 30, 34, 58] Also in line with literature data, [24, 30, 58] is the binding energy for the calculated 0 K minimum energy structure.

Table 1. Relative energies (in eV) with respect to the most stable structure of HCOOH adsorbed on TiO_2-anatase (101) as a function of basis set cutoff (BSC, in Ry). The binding energy (in eV) is reported in parenthesis.

BSC (Ry)	Mol0	Mol1	Dis2	Dis3
80	0.0 (0.971)	0.011 (0.960)	0.042 (0.929)	0.598 (0.373)
90	0.0 (0.952)	0.008 (0.944)	0.030 (0.922)	0.576 (0.375)
100	0.0 (0.941)	0.010 (0.931)	0.033 (0.907)	0.576 (0.363)
120	0.0 (0.947)	0.010 (0.937)	0.034 (0.912)	0.577 (0.369)
140	0.0 (0.947)	0.008 (0.939)	0.031 (0.916)	0.575 (0.372)
160	0.0 (0.941)	0.008 (0.933)	0.034 (0.907)	0.575 (0.366)

On the other hand, the finite temperature simulations, performed either with DCOOD or HCOOH, reveal that the acid proton shuttles between a TiO_2 surface oxygen (O_{surf}) and the carboxylic oxygen O_{carb} (Figure 4a), indicating a fast equilibrium between formic acid and formate on the anatase (101) surface. The time evolution of the two C-O distances is particularly informative. Whereas the two C-O bond lengths should be different in a molecularly adsorbed system, with one C-O bond always shorter than the other one, here such a distinction is missing, as shown in Figure 4b. The fast interconversion between the dissociated and the non-dissociated DCOOD moiety (Figure 3e-f, and Figure 4a) might have consequences on the IR signal as well. The fingerprints of the spectroscopic behavior of the system might be obtained by linear response approaches using appropriate autocorrelation functions. The power spectra of the O_{carb}-D and O_{surf}-D bond stretching are shown in Figure 4c, along with the same quantity calculated for the O-D bond stretching of a gas-phase DCOOD molecule at 300 K. In the gas-phase spectrum, the O-D stretching frequency is that typical of a stable O-D bond, with an intense peak at ~2550 cm^{-1}. Such signal is missing in the spectra of both O_{surf}-D and O_{carb}-D bond stretching, confirming that neither O_{surf}-D nor O_{carb}-D are stable bonds. Thus, the carboxyl proton is actually shared between the formate and the surface moieties.

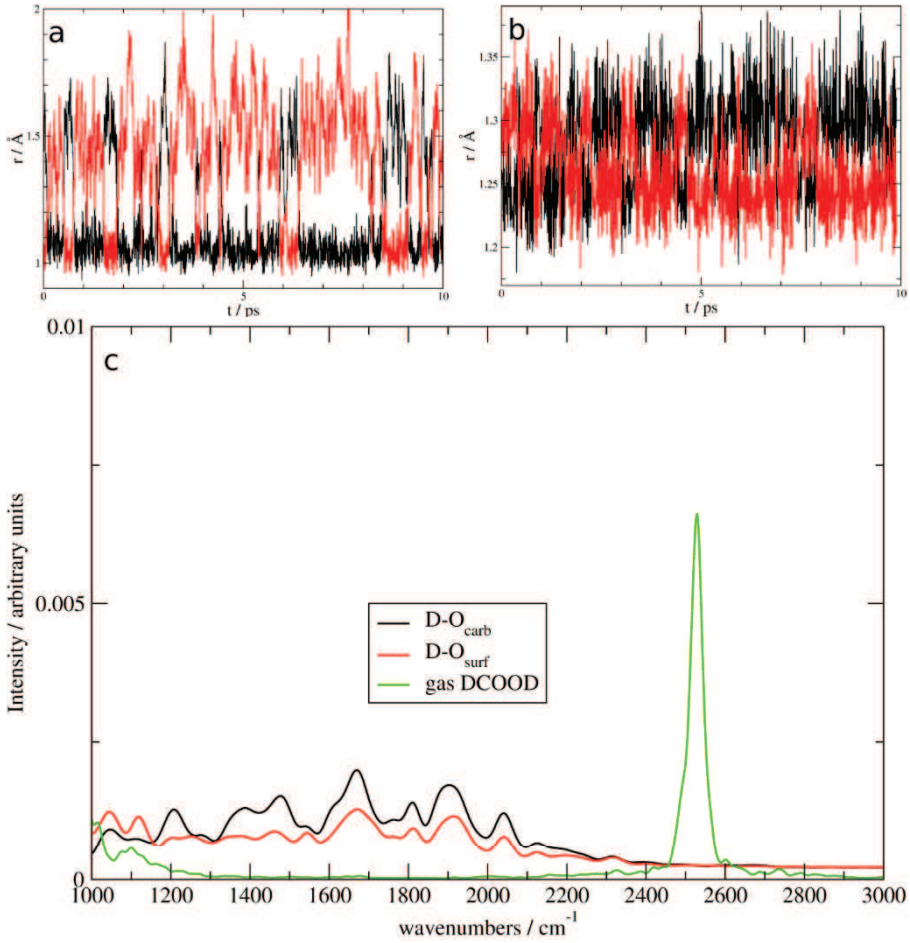

Figure 4. a): time evolution of the D-O distances relative to O_{carb} and O_{surf} (black and red lines, respectively). b): time evolution of the two C-O bond distances in adsorbed DCOOD. c): Power spectra from the autocorrelation of the O_{carb}-D bond stretching (black line), and of the O_{surf}-D bond stretching (red line), calculated from the simulation of DCOOD on TiO_2(101). The power spectrum calculated for the O-D bond stretching from a 300 K simulation of a DCOOD molecule in the gas phase is shown for comparison (green line).

In conclusion, the combined modeling-spectroscopic study showed that a fast equilibrium exists between formate and formic acid on top of anatase TiO_2 (101) facets, triggered by molecule-surface proton sharing at the femtosecond-scale. These results could explain why the signal of the OH stretching mode is missing in the IRRAS spectra of formic acid on anatase, and reconcile previous experimental studies - supporting the adsorption of HCOOH as monodentate formate, with static (0 K) computational data - suggesting molecularly adsorbed formic acid.

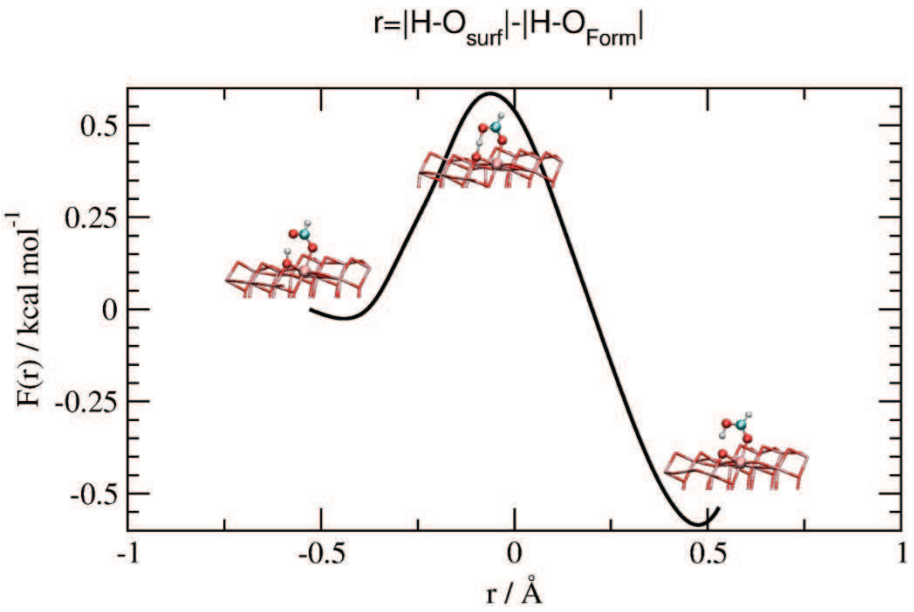

Figure 5. Free energy profile (FEP) of the FA fast equilibrium on TiO_2 (101) surface.

Besides solving this long-standing controversy, the "dynamically shared proton" picture sheds new light into the adsorption of carboxyl-containing moieties on titania, showcases the role of surface oxygen atoms and deepens our understanding into the behavior of organic acids on nanopowder TiO_2 samples. Additionally, the herein disclosed coexistence of molecular formic acid and dissociated formate provides a solid ground for unravelling the catalytic mechanism of direct amidation and peptide bond formation on anatase TiO_2 (101) surfaces.

The free energy profile for the fast proton shuttling was calculated at room temperature within the framework of the Bluemoon ensemble (BM) sampling technique. [59] Such a technique is a statistical perturbation approach with is able to sample "rare events" processes and moreover able to provide a Free Energy profile along a given "reaction coordinate". In this particular case, as reaction coordinated we have chosen the difference between the $O_{surf}H$ distance and the $O_{form}H$ one, $r=|O_{surf}H|-|O_{form}H|$. The r values are allowed to progressively decrease from 0.6Å to -0.6Å. Positive r values correspond to the un-dissociated formic acid molecularly adsorbed to (101) anatase, while r negative values correspond to dissociated formate, with the proton bonded to O_{surf}. The process has been divided in 15 steps (from +0.6Å to -0.6Å). For each step a molecular dynamics run was performed at 300 K, constraining r to the given value. Each molecular dynamic run was stopped when the mean constraint force was converged. The integral of minus

the mean forces provides, in the Bluemoon ensemble approach, the free energy profile for process along the given reaction coordinate. It should be noted, by inspecting Figure 5, that the molecularly adsorbed formic acid is slightly more stable than the dissociated one by ~0.5 kcal mol^{-1}. The free energy barrier is ~1.0 kcal mol^{-1}, and that the transition state is located at a slightly negative value of r (actually r=-0.1Å). The backward reaction, namely the transfer of the proton from O_{surf} to O_{form} has on the other hand a free energy barrier of 0.5 kcal mol^{-1}.

Formic acid and methylamine reaction on the titania surface

The free energy surface (FES) for the formation of the amide from HCOOH adsorbed on (101) anatase and Methyl amine from the gas phase was simulated by combining a First Principles Molecular Dynamics approach with the Metadynamics method. [60] This combined approach enables one to study reactive events that can be considered "rare events" on the timescale of Molecular dynamics simulations. It is a statistical perturbation approach where one defines a history dependent potential that, added to the true system potential, allows the system to bypass free energy wells so explore the free energy surface of the system as a function of given "collective variables" (CV). Such CV's are chosen in order to properly describe the chemical process under investigation. Herein, as CV's, are chosen the distance between the N atom of the amine and the C atom of the formic acid, and the coordination number of the O_{form} atom with the protons (Figure 6). These CV's would represent the formation of the amide C-N bond and the formation of the H_2O leaving group of the condensation reaction. The simulation was performed at 300 K. The modelled surface was a regular (101) anatase surface. The starting configuration consisted of two HCOOH adsorbed on the surface, while one gas phase CH_3NH_2 molecule (not adsorbed) and positioned at ~5 Å from one of the HCOOH carbon atom at ~5 Å from the anatase surface. With such a starting configuration, the system explored two free energy wells. One corresponding to a van der Waals complex between the adsorbed acid and the amine. A free energy minimum of ~40 kcal mol^{-1} corresponds to this well.

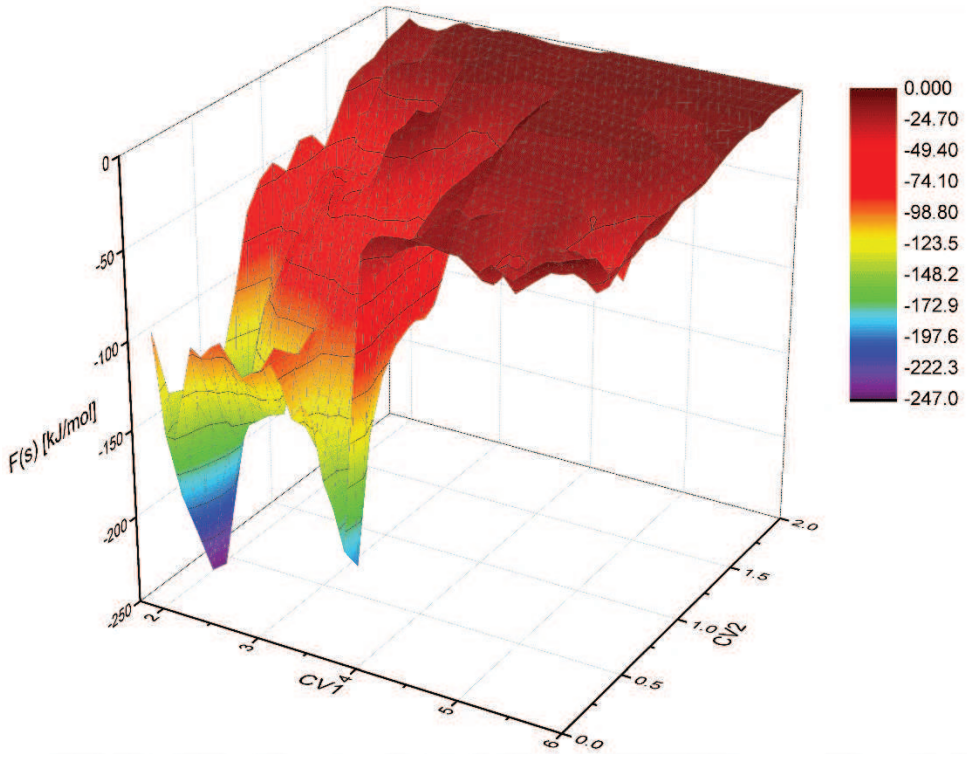

Figure 6. FES for the formation of the amide from HCOOH adsorbed on (101) anatase and CH_3NH_2 from the gas phase as simulated by combining First Principles Molecular Dynamics with Metadynamics. CV1 represents the C-N distance; CV2 represents the O_{form} coordination number.

A second and deeper free energy minimum (~60 kcal mol^{-1}) corresponds to the amide adsorbed on the surface and the formation of the condensation water molecule. In our simulation the system visited first the well corresponding to the van der Waals like complex (corresponding to a C-N distance oscillating around 2.8Å, and associated to CV1 in Figure 6). Such a minimum in the free energy surface is reached in a barrier less fashion.

The metadynamics then continued and the system escaped from the well and reached the second and free energy minimum where the condensation reaction occurred. The passage from the first to the second well is accomplished by overcoming a free energy barrier of~15 kcal mol^{-1}. Snapshots of relevant structures along the condensation path are represented in Figure 7.

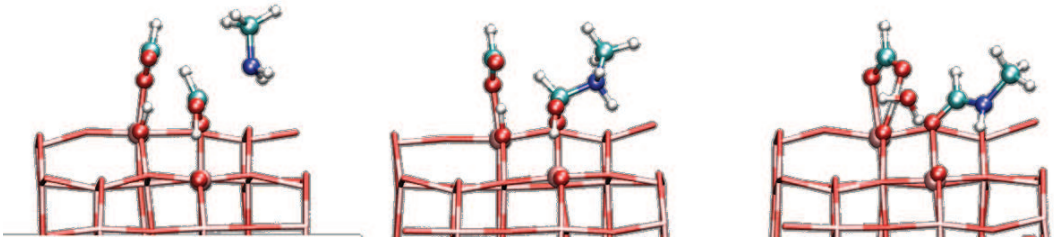

Figure 7. Left: representation of a structure from the first free energy potential well. Center: representation of a structure relative to the activated complex. Right: Structure relative to the final free energywell representing the adsorbed amide and the leaving water molecule.

Conclusions

The results of this chapter provided a model description of the formic acid/TiO_2 system. The computational simulations show a shuttling process of the proton of HCOOH between the molecule and the surface. This picture is also helpful for better understanding the further interplay of formic acid with methylamine in the formation of the amide bond on the surface of titania.

Experimental and Theoretical Methods

The commercial TiO_2 P25 (by Evonik) Degussa was used. This powder, (specific surface area of ca. 50 m^2/g, purity ≥ 99.5 wt%) contains ca. 80% anatase, 20% rutile by weight, but rutile nanoparticles contribute to only ca. 7% of the exposed surface.[50] Formic acid HCCOH was high-purity Sigma-Aldrich product, while HCOOD (99.90% D) was purchased from Euriso-top. The vapors of these chemicals were admitted onto the samples in the IR cell after several freeze-pump-thaw cycles. High purity CO (Praxair) was employed without any further purification, except liquid nitrogen trapping.

For IR spectroscopic measurements, the TiO_2 powder was pressed in form of self-supporting pellets ("optical thickness" ca. 10 mg/cm^2), and then placed in IR cells equipped with CaF_2 or KBr windows, depending if used for measurements at beam temperature (b.t., ca. 323 K) or at 100 K,[51] and a valve for connection to vacuum lines (residual pressure $1.0 \cdot 10^{-5}$ mbar) allowing thermal treatments and adsorption/desorption experiments to be carried out *in situ*. Samples were heated inside the cells under dynamic vacuum from room temperature to 723 K (ca. 5 K/min) and outgassed at this temperature for 1 h. To compensate for the reductive effect on TiO_2 produced by this dehydration/dihydroxylation treatment, 6 mbar of O_2 were finally admitted in the cell and kept in contact with the samples for 1 h at 723 K. The system was subsequently cooled to 473 K in O_2 and finally to room temperature under outgassing. The treated samples appeared perfectly white, as expected for stoichiometric TiO_2. The cell was then transferred in the IR instruments (Bruker Vector 22; detector: DTGS), without exposure of the sample to air, and connected to another vacuum line, for the in situ adsorption/desorption of HCOOH/HCOOD or CO, admitted on samples kept at b.t. or 100 K, respectively.

The adsorption of gas-phase HCOOH on anatase TiO_2(101) is modelled by both Density Functional Theory (DFT) structural optimizations and First-Principles Molecular Dynamics (FPMD) simulations.[67, 68] The adopted periodic slab ($Ti_{36}O_{72}$), formed by six Ti_6O_{12} layer (surface area: 10.349 × 11.355 $Å^2$), provides a good description of the adsorption of probe molecules on TiO_2(101) at both low- and high-coverage limits.[51, 56, 66] A vacuum region of 12 Å was adopted to minimize inter-slab interactions and the bottom $T1_6O_{12}$ atoms were held fixed. The PBE approximation to DFT[69] plane-wave basis sets and norm-conserving pseudopotentials were adopted.[70] The non-linear core correction scheme was employed for Ti (considered as Ti^{+4}).[71] For geometry optimization, different cutoff values were adopted to check

convergence with basis set truncation (Table 1). A maximum force of 0.0005 Hartree/Bohr was used as convergence criterion. Atomic coordinates are reported in the Supporting Information.

The room-temperature behavior of HCOOH on (101)-anatase was simulated at 300 K via FPMD.[67, 68] Two sets of simulations were performed, using cutoffs of 80 and 90 Ry respectively. Adsorption of either HCOOH or deuterated DCOOD was considered. Equations of motion were integrated with time step of 3 au and fictitious mass for electronic coefficients of 500 au. Data were collected for 10 ps elapsed time, after 5 ps equilibration. Such setup for FPMD simulations proved to be suitable for diverse complex organic-inorganic systems, including metal oxides, also containing Ti-sites.[51, 56, 66, 72-75] Whereas only the results obtained from FPMD with 90 Ry cutoff and DCOOD were discussed, all simulations provided very similar results. Power spectra were calculated from autocorrelation functions derived from the FPMD trajectories.

References

[1] A. G. Thomas and K. L. Syres *Chem. Soc. Rev.* **2012** (41) 4207–4217.
[2] M. Răileanu, M. Crişan, I. Niţoi, A. Ianculescu, P. Oancea, D. Crişan and L. Todan *Water, Air, & Soil Pollution* **2013** (224) 1548.
[3] R. Daghrir, P. Drogui and D. Robert *Industrial & Engineering Chemistry Research* **2013** (52) 3581–3599.
[4] I. S. Grover, R. C. Prajapat, S. Singh and B. Pal *Solar Energy* **2017** (144) 612-618.
[5] Y. Ma, X. Wang, Y. Jia, X. Chen, H. Han and C. Li *Chem. Rev.* **2014** (114) 9987-10043.
[6] M. Pastore, T. Etienne and F. De Angelis *Journal of Materials Chemistry C* **2016** (4) 4346-4373.
[7] A. Amacher, C. Y. Yi, J. B. Yang, M. P. Bircher, Y. C. Fu, M. Cascella, M. Gratzel, S. Decurtins and S. X. Liu *Chem. Commun.* **2014** (50) 6540-6542.
[8] A. J. Huckaba, A. Yella, P. Brogdon, J. S. Murphy, M. K. Nazeeruddin, M. Gratzel and J. H. Delcamp *Chem. Commun.* **2016** (52) 8424-8427.
[9] N. Manfredi, B. Cecconi, V. Calabrese, A. Minotti, F. Peri, R. Ruffo, M. Monai, I. Romero-Ocana, T. Montini, P. Fornasiero and A. Abbotto *Chem. Commun.* **2016** (52) 6977-6980.
[10] C. F. A. Negre, R. L. Milot, L. A. Martini, W. Ding, R. H. Crabtree, C. A. Schmuttenmaer and V. S. Batista *J. Phys. Chem. C* **2013** (117) 24462–24470.
[11] A. Assabane, Y. Ait Ichou, H. Tahiri, C. Guillard and J.-M. Herrmann *Applied Catalysis B: Environmental* **2000** (24) 71–87.
[12] G. Kim and W. Choi *Applied Catalysis B: Environmental* **2010** (100) 77–83.
[13] Y. Ji, B. Wang and Y. Luo *J. Phys. Chem. C* **2014** (118) 21457–21462.
[14] M. Nilsing, P. Persson and L. Ojamae *Chemical Physics Letters* **2005** (415) 375-380.
[15] F. Schiffmann, J. VandeVondele, J. Hutter, R. Wirz, A. Urakawa and A. Baiker *J. Phys. Chem. C* **2010** (114) 8398-8404.
[16] M. F. Atitar, R. Dillert and D. W. Bahnemann *J. Phys. Chem. C* **2017** (121) 4293-4303.
[17] F. Petronella, A. Truppi, C. Ingrosso, T. Placido, M. Striccoli, M. L. Curri, A. Agostiano and R. Comparelli *Catalysis Today* **2017** (281) 85-100.
[18] C. Deiana, Y. Sakhno, M. Fabbiani, M. Pazzi, M. Vincenti and G. Martra *ChemCatChem* **2013** (5) 2832-2834.
[19] J. W. Comerford, J. H. Clark, D. J. Macquarrie and S. W. Breeden *Chem. Commun.* **2009** 2562-2564.
[20] K. Komura, Y. Nakano and M. Koketsu *Green Chem.* **2011** (13) 828–831.

[21] C. L. Allen, A. R. Chhatwal and J. M. J. Williams *Chem. Commun.* **2012** (48) 666-668.
[22] M. Tamura, T. Tonomura, K.-i. Shimizu and A. Satsuma *Green Chem.* **2012** (14) 717–724.
[23] D. J. C. Constable, P. J. Dunn, J. D. Hayler, G. R. Humphrey, J. J. L. Leazer, R. J. Linderman, K. Lorenz, J. Manley, B. A. Pearlman, A. Wells, A. Zaks and T. Y. Zhang *Green Chem.* **2007** (9) 411-420.
[24] A. Vittadini, A. Selloni, F. P. Rotzinger and M. Grätzel *Journal of Physical Chemistry B* **2000** (104) 1300–1306.
[25] A. Tilocca and A. Selloni *Journal of Physical Chemistry B* **2004** (108) 4743-4751.
[26] X. Q. Gong, A. Selloni and A. Vittadini *Journal of Physical Chemistry B* **2006** (110) 2804-2811.
[27] C. Deiana, E. Fois, S. Coluccia and G. Martra *J. Phys. Chem. C* **2010** (114) 21531-21538.
[28] J. F. Porter, Y. G. Li and C. K. Chan *Journal of Materials Science* **1999** (34) 1523-1531.
[29] G. Martra, C. Deiana, Y. Sakhno, I. Barberis, M. Fabbiani, M. Pazzi and M. Vincenti *Angew. Chem. Int. Ed.* **2014** (53) 4671-4674.
[30] X.-Q. Gong and A. Selloni *J. Catal.* **2007** (249) 134–139.
[31] F. Nunzi and F. De Angelis *J. Phys. Chem. C* **2011** (115) 2179-2186.
[32] K. L. Miller, C. W. Lee, J. L. Falconer and J. W. Medlin *J. Catal.* **2010** (275) 294-299.
[33] G. Pacchioni *ACS Catal.* **2014** (4) 2874-2888.
[34] K. L. Miller, C. B. Musgrave, J. L. Falconer and J. W. Medlin *J. Phys. Chem. C* **2011** (115) 2738-2749.
[35] C. Spreafico, F. Schiffmann and J. VandeVondele *J. Phys. Chem. C* **2014** (118) 6251-6260.
[36] M. Xu, H. Noei, M. Buchholz, M. Muhler, C. Wöll and Y. Wang *Catalysis Today* **2012** (182) 12–15.
[37] D. C. Grinter, M. Nicotra and G. Thornton *J. Phys. Chem. C* **2012** (116) 11643-11651.
[38] H. Onishi and Y. Iwasawa *Chemical Physics Letters* **1994** (226) 111-114.
[39] U. Diebold *Surface Science Reports* **2003** (48) 53-229.
[40] L. Ojamae, C. Aulin, H. Pedersen and P. O. Kall *Journal of Colloid and Interface Science* **2006** (296) 71-78.
[41] P. R. McGill and H. Idriss *Surface Science* **2008** (602) 3688-3695.
[42] R. Lindsay, S. Tomic, A. Wander, M. Garcia-Mendez and G. Thornton *J. Phys. Chem. C* **2008** (112) 14154-14157.

[43] A. Mattsson, S. L. Hu, K. Hermansson and L. Osterlund *J. Chem. Phys.* **2014** (140) 12.
[44] H. Hussain, X. Torrelles, G. Cabailh, P. Rajput, R. Lindsay, O. Bikondoa, M. Tillotson, R. Grau-Crespo, J. Zegenhagen and G. Thornton *J. Phys. Chem. C* **2016** (120) 7586-7590.
[45] S. L. Hu, P. A. Bopp, L. Osterlund, P. Broqvist and K. Herrnansson *J. Phys. Chem. C* **2014** (118) 14876-14887.
[46] C. Deiana, M. Minella, G. Tabacchi, V. Maurino, E. Fois and G. Martra *PCCP* **2013** (15) 307-315.
[47] E. Fois, G. Tabacchi, D. Barreca, A. Gasparotto and E. Tondello *Angewandte Chemie-International Edition* **2010** (49) 1944-1948.
[48] G. Tabacchi, E. Fois, D. Barreca and A. Gasparotto *Physica Status Solidi a-Applications and Materials Science* **2014** (211) 251-259.
[49] L. Martinez-Suarez, N. Siemer, J. Frenzel and D. Marx *ACS Catal.* **2015** (5) 4201-4218.
[50] S. Y. Ma, L. M. Liu and S. Q. Wang *J. Phys. Chem. C* **2016** (120) 5398-5409.
[51] C. Deiana, G. Tabacchi, V. Maurino, S. Coluccia, G. Martra and E. Fois *PCCP* **2013** (15) 13391-13399.
[52] L.-F. Liao, W.-C. Wu, C.-Y. Chen and J.-L. Lin *Journal of Physical Chemistry B* **2001** (105) 7678–7685.
[53] K. Nakamoto *Infrared and Raman Spectra of Inorganic and Coordination Compounds* **1986** (John Wiley & Sons, New York).
[54] P. Borghetti, E. Meriggio, G. Rousse, G. Cabailh, R. Lazzari and J. Jupille *Journal of Physical Chemistry Letters* **2016** (7) 3223-3228.
[55] K. Hadjiivanov, J. Lamotte and J.-C. Lavalley *Langmuir* **1997** (13) 3374-3381.
[56] K. I. Hadjiivanov and G. N. Vayssilov *Characterization of oxide surfaces and zeolites by carbon monoxide as an IR probe molecule* in Advances in Catalysis, B. C. Gates and H. Knozinger Eds. **2002** (Elsevier Academic Press Inc, San Diego).
[57] C. Deiana, E. Fois, G. Martra, S. Narbey, F. Pellegrino and G. Tabacchi *ChemPhysChem* **2016** (17) 1956-1960.
[58] K. L. Miller, J. L. Falconer and J. W. Medlin *J. Catal.* **2011** (278) 321-328.
[59] G. Ciccotti, M. Ferrario, J. T. Hynes and R. Kapral *Chem. Phys.* **1989** (129) 241-251.
[60] A. Laio and M. Parrinello *Proc. Natl. Acad. Sci.* **2002** (99) 12562-12566.

Chapter Five

Solvent free synthesis of Ser-His from non-activated amino acids

Short homopeptides (up to 3-mer) of serine and histidine, as well as Ser-His and His-Ser hetero-dipeptides, are produced from the non-activated amino acids by using a facile chemical vapor deposition and TiO_2 nanoparticles as catalyst. The assessment of the formation of peptides is based on spectroscopic data such as *in situ* FT-IR and mass spectrometry. Evidence of the capability of Ser-His to promote hydrolysis of peptide bonds in hexaglycine is provided, contributing to the debate on the effectiveness of this dipeptide as an organocatalyst.

Peptide formation from Ser and His

Peptide synthesis interests several aspects of modern chemistry research, from the increasing employment of peptide-based pharmaceutics, [1, 2] the needs for green synthesis, [3, 4] to the implications in the prebiotic chemistry. [5] Catalytic methods represent a promising approach, in alternative to the well-established solid phase peptide synthesis (SPPS), [6, 7] for the possibility to avoid reagents activation steps and to carry out the reaction using mild conditions. [8] Heterogeneous catalysis has lately drawn attention and surface-catalyzed peptide bond formation is of particular interest in synthetic biochemistry and shows great potential in synthetizing different kinds of peptides. [9, 10] Taking inspiration from prebiotic chemistry possible scenarios, non-activated amino acids can be adsorbed as zwitterion from aqueous solution on different materials. Typically, oxides are good candidates as approximations to mineral surfaces and after the adsorption are heated for water removal, simulating wet and dry cycles that can occur in hydrothermal systems. [9, 11] Exploiting this method, short homopeptide of glycine, [10, 12] alanine, [9, 13] valine, [14] asparagine, [15] have been synthetized. Noteworthy, the most abundant product was diketopiperazine (DKP) when silica was used as catalyst towards glycine [12] and alanine. [9] The adsorption from aqueous solution of different amino acids was also investigated, mainly focusing on competitive aspects but, at the best of our knowledge, the subsequent possible reaction to form heteropeptides was not explored. On the other hand, chemical vapor deposition (CVD) represents an alternative approach where at first amino acids are sublimated in the presence of the catalyst, in a dry state. Non-ionic, non-activated amino acid molecules adsorb and react on the catalyst surface and the produced peptides are later washed away passing into solutions. Indeed, amino

acid polymerization via sublimation process was demonstrated to be an effective method to produce glycine oligomers up to 16 or 11 units long on titanium dioxide and silica, respectively, with DKP being a minor product. [16] This procedure can be potentially applied to other amino acids capable to sublimate at a temperature lower the decomposition one, a property exhibited by 14 of the 20 proteinogenic amino acids. [17] Moreover, heteropeptides can be obtained in principle by sublimating the amino acids of interest in the proper sequence. On this basis, here is reported a proof-of-principle study of the production of homo- and heteropeptides produced by sublimating serine (Ser) and histidine (His) on TiO_2 nanoparticles, exploiting the CVD method, carried out using a cell for *in situ* IR measurements in controlled atmosphere as the reactor, set up for the oligomerization of Gly. [16] The interest towards the possibility to prepare peptides containing Ser and His stems from the presence of these amino acids in the catalytic triad (together with Asp) found in many enzymes such as chymotrypsin, subtilisin and phospholipase A2. [18] Serine hydrolases comprise approximately 1% of the genes in the human proteome. [19] Short peptides can be considered minimalistic form of enzymes, for organic synthesis and prebiotic chemistry. [20] The catalytic activity of Ser-His dipeptide has been reported for the first time by the group of Zhao, [21, 22] showing different cases of hydrolytic activity towards proteins [23, 24] and nucleic acids. [25-27] Nevertheless, MacDonald et al. recently reported a different conclusion on the activity of Ser-His, assessing a non-statistical significance in the hydrolysis of sterically hindered esters and amides. [28] As a contribution to the debate, the hydrolytic activity of Ser-His produced by CVD is tested towards a simple, model oligopeptide, namely hexaglycine (6-Gly).

Methods: hydrolysis test

Aside the methods described in the dedicated section of this thesis, here is defined the protocol adopted to test the possible hydrolytic activity towards a small peptide.

0.5 mL of 10 ppm hexaglycine (6-Gly) solution is mixed with 0.5 mL (thus halving the 6-Gly concentration) of i) solution of His-Ser dimer purchased from Sigma-Aldrich, ii) washing solutions from adsorption of His-Ser sequence on TiO_2 experiment iii) washing solutions from adsorption of Ser-His sequence on TiO_2 experiments. The samples are stirred for 10 minutes with Vortex system and then incubated at 298 K for 12 hours. After incubation time, samples are analyzed by High-Resolution Mass Spectrometry (HR-MS). A solution of 6-Gly alone is incubated as well and analyzed as 6-Gly stability control test towards hydrolysis in water.

Formation of homo-peptides of Ser and His

The possible formation of homo-peptides of Ser and His along the catalytic CVD method is monitored by in-situ IR spectroscopy. The results are reported in
Figure 1, where curve a is the spectrum of bare titania, exhibiting only the typical pattern of weak bands in the range from 3750 to 3600 cm^{-1} due to surface hydroxy groups. [29] In the type of TiO_2 nanoparticles used, -OH groups occupy only a minor fraction of surface sites, thus is not surprising if their IR signals are perturbed in a limited extent by increasing the amount of adsorbed amino acid (aa).
Conversely, the important feature in the spectrum of bare TiO_2 is the absence of the band at ca. 1620 cm^{-1} due to the deformation mode (δ) of H_2O molecules, indicating the catalyst is fully dehydrated before the contact with aa. Passing to the systems resulting from the adsorption of aa on the catalyst, Ser is dosed on TiO_2 nanoparticles up to the attainment of a surface coverage of ~ 70% (
Figure 2) as estimated by the competitive CO_2 adsorption method (see the Materials and Methods section).

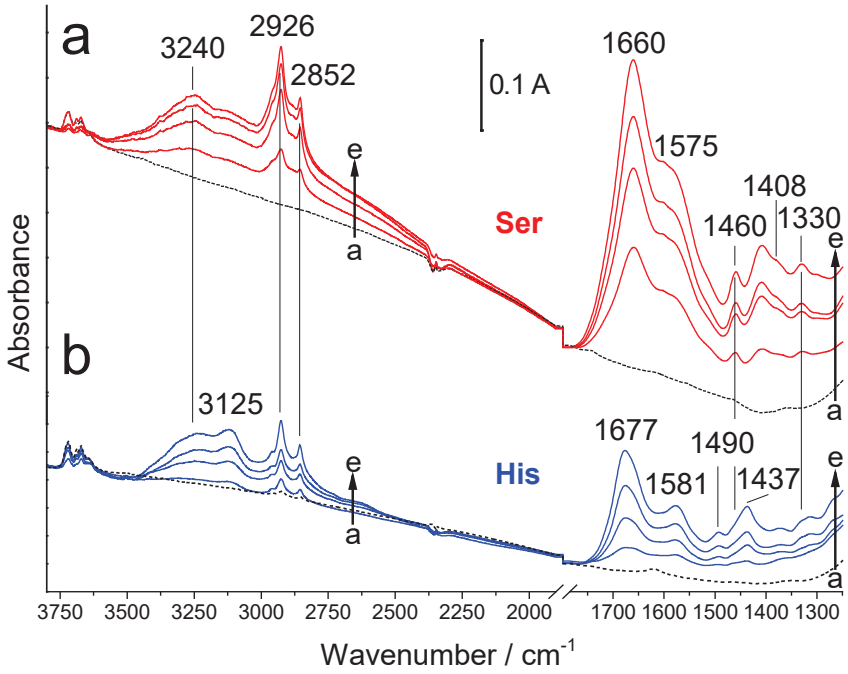

Figure 1. IR spectra resulting from the adsorption of Ser (section a) and His (section b) from vapour phase on TiO_2 P25. The intensity of the spectra is normalized with respect to the optical thickness (mg/cm^{-2}) of the self-supporting pellets used for the measurements. Curves a: TiO_2 P25 dried by outgassing at 723 K; curves b-e: after exposure to Ser or His vapours for, 30, 60, 90 and 120 min.

In the case of His, only a surface coverage of ~ 30% is achieved after the same time of contact with aa vapor, likely because the lower propensity of this a toward sublimation. The stepwise contact with Ser (section a) or His (section b) vapors resulted in the appearance and progressive growth of signals in the 1680-1620 cm^{-1} and 1560-1530 cm^{-1} ranges, which can be easily recognized as amide I and amide II bands, respectively, typical of peptide species. The weaker signal at 1330 cm^{-1} (that resisted H/D isotopic exchange, *vide infra*) might result from the deformation (δ) mode involving the C_α-H bond. [30] Noteworthy, these bands are already present after the adsorption of the first doses of amino acids, indicating that the formation of peptides is almost independent from the surface coverage. However, evidence of the role of TiO_2 as catalyst promoting aa condensation is obtained by comparison with a control test. The sublimation of each amino acid is carried out in the absence of the titanium dioxide pellet: the film formed by the amino acid condensed on the inner walls of the cell is dissolved in water and the resulting solutions are analyzed by HR-MS. Only Ser and His monomers are found (*vide infra*), indicating that the formation of peptides in vapor phase during aa sublimation, followed by their adsorption on TiO_2 nanoparticles, can be excluded.

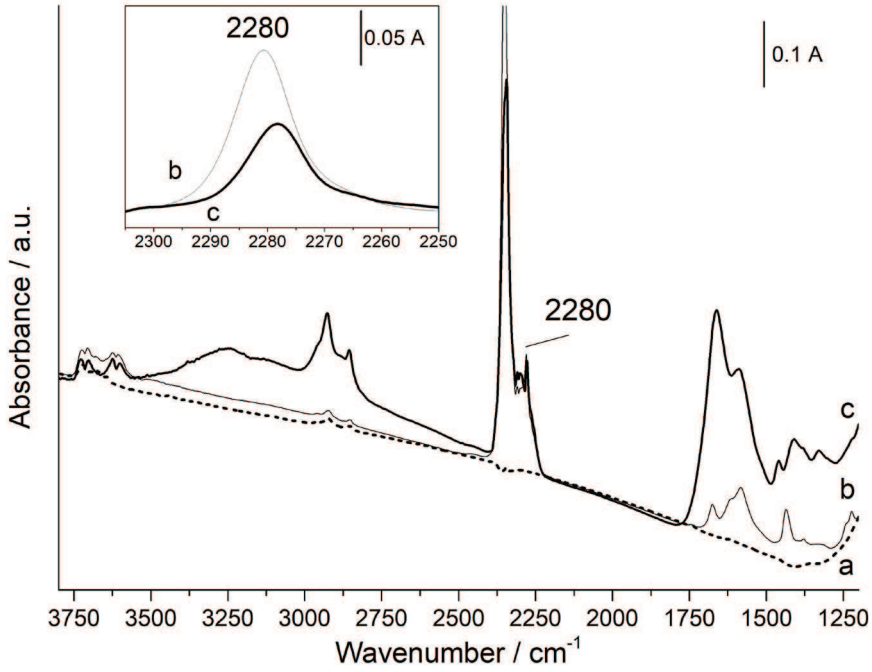

Figure 2. IR spectra of surface coverage evaluation with CO_2 mixture: a) bare TiO_2 surface after dehydration at 723 K; b) after contact with CO_2 mixture at 90 mbar c) after contact with CO_2 mixture at 90 mbar after 1 hour of Ser adsorption at 433 K. Inset: zoom of the 2305–2250 cm^{-1} range.

Focusing on IR data, other features common to Ser/TiO_2 and His/TiO_2 spectra is the broad band at 3240 cm^{-1}, assignable to the stretching mode (ν) of the N-H moiety of peptide bonds involved in weak H-bonding. [31] Two narrow bands at 2926 and 2852 cm^{-1} are due to the ν_{asym} and ν_{sym} -CH_2 groups present in both aa with the partner δCH_2 mode producing the signal at 1460 cm^{-1} (resolved band in the Ser/TiO_2 spectra, section a; high frequency shoulder of the signal at 1437 cm^{-1} in the His/TiO_2 spectra, section b). [32] Conversely, the main distinctive feature of the Ser/TiO_2 spectra (section a) is the broad band spread over the 3500-2250 cm^{-1} range, assignable to the νOH mode of H-bonded hydroxy group of the side chain of Ser, whilst νCH and νCN/δCH of the imidazole group of the His side chain are responsible of signals at 3125 and 1490 cm^{-1}, respectively, in the His/TiO_2 spectra (section b). [31] The ν_{sym} of COO^- groups might produce the signals at 1408 and 1423 cm^{-1} in Ser/TiO_2 and His/TiO_2 spectra, respectively, the ν_{sym} of COO^- likely contributing to the pattern in the 1650-1540 cm^{-1} range. [33]

The deprotonation of carboxylic groups (aa molecules in vapor phase are in a non-ionic form) could be accompanied by the protonation of -NH_2 moieties, as observed for the adsorption of Gly vapors on hydroxyapatite. [34] Thus, the

contribution of δ_{asym} and δ_{sym} -NH_3^+ modes in the 1650-1550 cm^{-1} range cannot be excluded, as well as of the partner νNH_3^+ modes to the range from 3200 to 2800 cm^{-1}. [33]

IR data provided strong suggestion for the formation of peptides, but do not contain information about the number of terms present in such possibly formed species. The catalyst pellets reacted with Ser or His are then washed with water, and the resulting aqueous solutions are analyzed by HR-MS. As a complementary investigation, the washed catalysts are recovered, dried and pelletized. These samples are then analyzed by IR spectroscopy in controlled atmosphere, to evaluate the relative amount of adsorbed species removed by washing. Since the absorption in the 1750-1500 cm^{-1} range is the targeted signal, the interference of the δH_2O band, expected at ~1620 cm^{-1}, due to water molecules left adsorbed on the catalyst surface after washing should be avoided. The solution adopted is an isotopic exchange by adsorption/desorption cycles of D_2O vapors before the collection of IR spectra. In order to carry out a consistent comparison of the state of the surface before and after the washing procedure, the catalyst samples reacted with aa are hydrated in the IR cell by adsorption/desorption of H_2O, and then undergo an isotopic exchange by adsorption/desorption of D_2O. IR spectra are collected after both steps, in order to monitor separately the effects of hydration and H/D exchange on aa-derived adsorbed species. The results are depicted in Figure 3, where curves in panels a/b and a'/b' are the spectra of Ser/TiO_2 and His/TiO_2 before/after washing, respectively. For both systems, the initial hydration resulted in an increase in intensity and a downshift of ~10 cm^{-1} of the band initially at 1660 cm^{-1}, for Ser/TiO_2, or 1677 cm^{-1}, for His/TiO_2, (panels a, a', curves a, b). This evolution is only partly due to the additional contribution of the δH_2O signal at ca. 1620 cm^{-1}, because is affected to a quite limited extent by the subsequent H/D exchange (panels a, a', curves c). Thus, the increase in intensity and downshift of the amide I band might be ascribed to a strengthening of H-bonding involving the C=O group of formed peptide species. Additional expected effects of the H/D exchange are a further downshift of the amide I band, and the fading of the amide II band, initially contributing to the signal over the 1600-1500 cm^{-1} range and then converted in a component of the complex spectral profile in the 1500-1350 cm^{-1} region. Moreover, the deformation modes of –NH_3^+ moieties are also downshifted by the conversion in –ND_3^+ groups, while the band at 1195 cm^{-1} appearing in the spectra after the treatment for isotopic exchange is due to the deformation mode of D_2O molecules left adsorbed on the catalyst surface after outgassing at b.t.

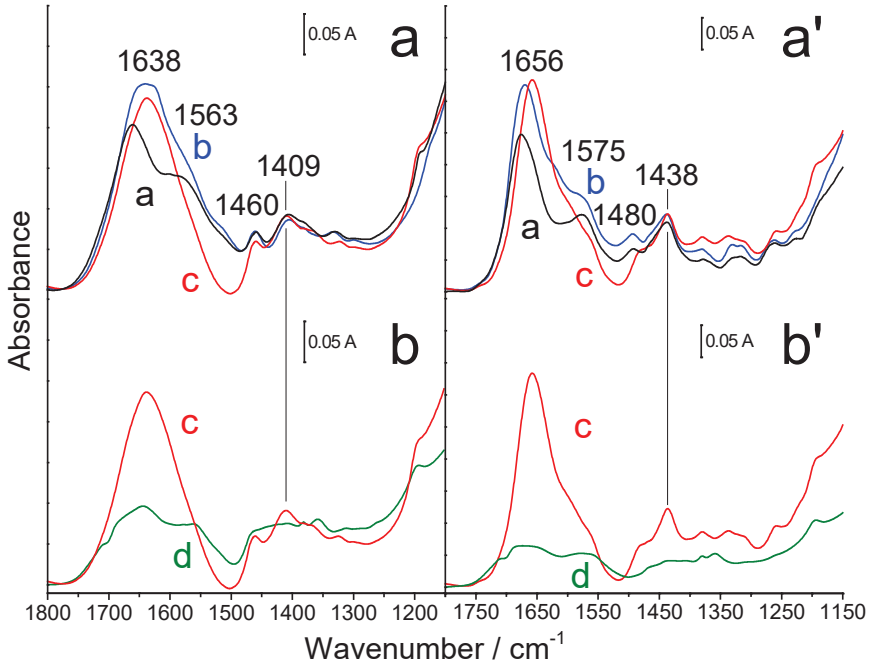

Figure 3. IR spectra comparing the signals from the sublimated Ser and His samples (panels a and a', respectively) with the ones after the washing procedure (panels b and b'). Curves a: 2 hours of Ser sublimation at 433 K; curve b: outgassed sample after subsequent contact with H_2O vapor at 20 mbar; curve c: outgassed sample after subsequent contact with D_2O vapor at 20 mbar; curve d: outgassed sample after contact with D_2O vapor at 20 mbar after washing procedure.

The spectral profiles of catalyst samples reacted with the aa, washed in H_2O and isotopically exchanged by contact with D_2O appear significantly decreased in intensity and changed in shape (panels b, b', curves d). On the basis of the ratio between the integrated intensity of the absorption in the 1700-1500 cm^{-1} range, the effectiveness of washing in removing aa derived species from the catalyst surface is evaluated to be ~65% and ~80% for Ser/TiO_2 and His/TiO_2, respectively.

As anticipated above, the solutions resulting from the washing procedure are analyzed by HR-MS. Two other samples are also analyzed, as "blanks". The first one is an aqueous solution of Ser, in order to assess the ESI analysis to be ineffective towards the formation of peptides, as conversely occurred in other ESI conditions. [35] The second is the film of Ser condensed on the inner wall of the IR cell, when the sublimation of aa is carried out in the absence of the catalyst, dissolved in water. In this case, the rationale is the assessment of the absence of peptide formation during sublimation, independently on the presence of titania nanoparticles.

The results are shown in Figure 4: in the two blank tests, only Ser in monomeric form is detected (panels a and b), whereas cyclic and linear (the most abundant) Ser

dipeptides, as well as Ser tripetide are present in the aqueous solutions resulting from washing the catalyst contacted with Ser vapors (panel c). Even though the cyclic dimer (diketopiperazine, $2S_{DKP}$) is present, signal at m/z=175, the detection of the linear dimer (2S), positioned at m/z=193, means that further monomer addition is possible. Indeed, the signal at m/z=280 is found for the Ser linear trimer (3S).

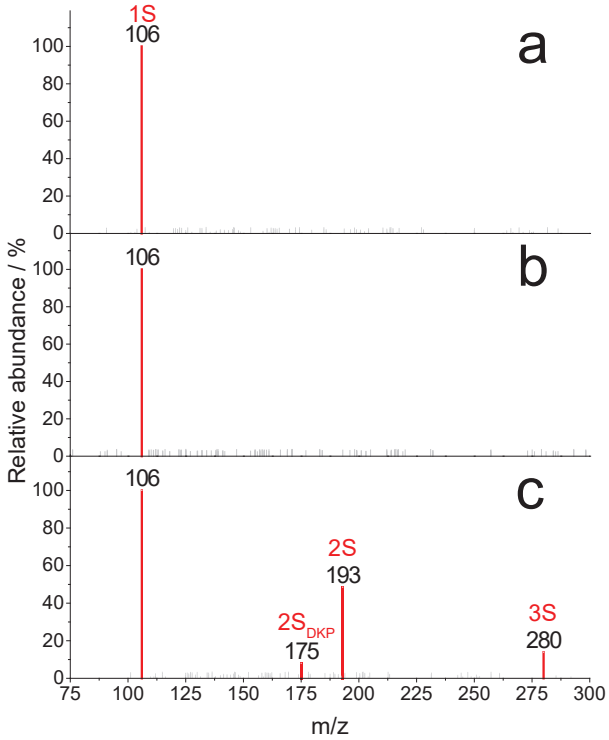

Figure 4. ESI-MS spectra of: a) Ser aqueous solution (10 ppm); b) Ser collected from the inner wall of the IR cell after sublimation at 433 K in the absence of the catalyst and dissolved in water; c) aqueous solution resulting from washing the catalyst contacted with Ser vapors for 2 hours at 433 K. Numbers on the bars are the m/z values, without decimal digits, for the sake of simplicity. Original HR-MS spectra with complete m/z values are reported in Appendix A.

The equivalent set of data for His is depicted in Figure 5. Also in this case, blank tests indicated that peptides are formed neither during the ESI analysis (panel a), nor in vapor phase during sublimation (panel b). However, when His is sublimated in the presence of the catalyst, cyclic ($2H_{DKP}$, m/z=275) and linear (2H, m/z=293) dipeptides and linear tripeptide (3H, m/z=430) are formed (panel c). In this case, the cyclic dimer seems to be favored, probably due to the influence of the bulkier side chain with respect to the Ser one.

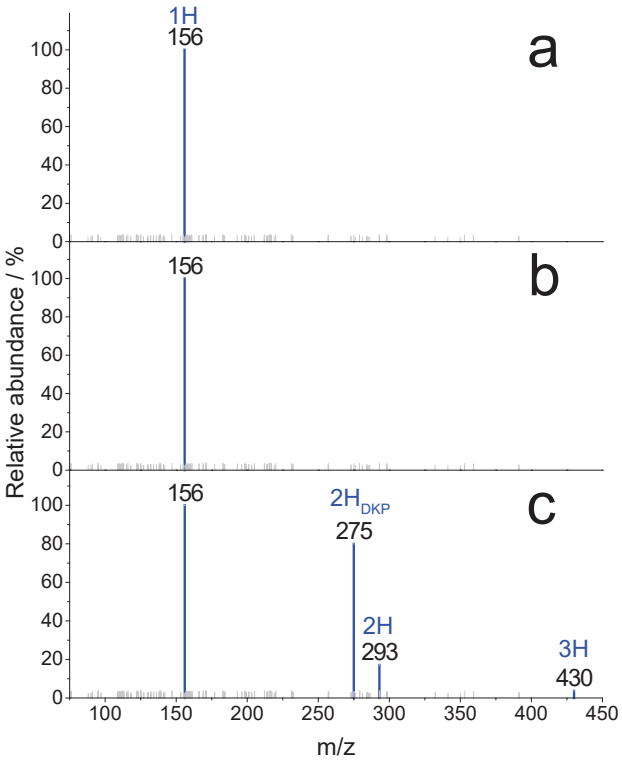

Figure 5. ESI-MS spectra of: a) His aqueous solution (10 ppm); b) His collected from the inner wall of the IR cell after sublimation at 473 K in the absence of the catalyst and dissolved in water; c) aqueous solution resulting from washing the catalyst contacted with His vapors for 2 hours at 473K. Numbers on the bars are the m/z values, without decimal digits, for the sake of simplicity. Original HR-MS spectra with complete m/z values are reported in Appendix A.

Using the same experimental procedure employed for the production of homopeptides, consecutive sublimations of Ser and His, and vice-versa (IR spectra in Appendix B), are carried out to obtain heteropeptides (see Materials and Method section).

Figure 6 shows the results of the HR-MS analysis of the final washing solutions. In both cases, homopeptides of Ser and His prevail by far, however, hetero dipeptides Ser-His or His-Ser (m/z = 243) Ser-Ser-His trimer (m/z = 330) are also present in a relative amount of ~ 10% and ~ 5%, respectively, in comparison with the most abundant species, that in both experiments is His in monomeric form (m/z= 156).

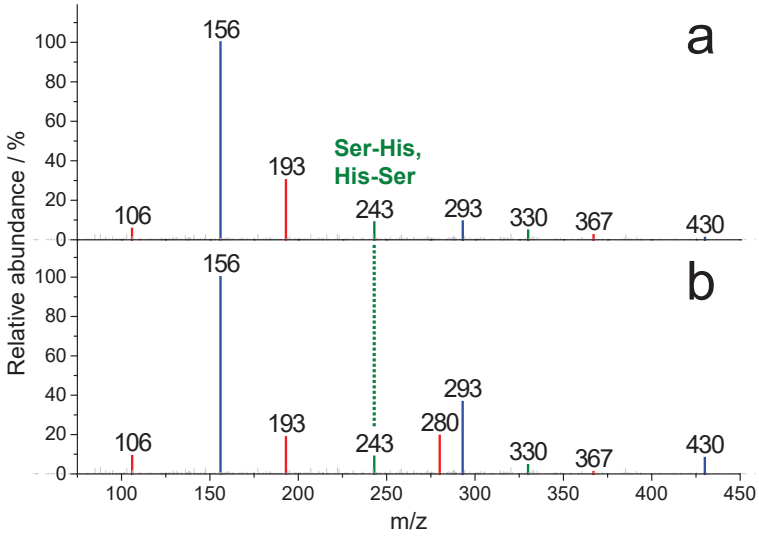

Figure 6. ESI-MS spectra of the aqueous solution resulting from washing the TiO_2 catalyst consecutively reacted with: a) Ser/His, or b) His/Ser. Color code: red, Ser monomer and homo-peptides (as in Fig. 3); blue, His monomer and homo-peptides (as in Fig. 4); green, Ser-His/His-Ser and Ser-Ser-His heteropeptides. Numbers on the bars are the m/z values, without decimal digits, for the sake of simplicity. Original HR-MS spectra with complete m/z values are reported in Appendix A.

Ser-His activity as peptide bond hydrolase towards hexaglycine

Using the procedure described in the Methods section of this chapter, the potential hydrolysis activity of Ser-His towards 6-Gly is tested. In Figure 7 the results obtained in two blank tests and using as organocatalyst the peptides mixtures obtained by washing pellets of TiO_2 catalyst contacted with Ser/His and His/Ser vapors are compared. The first blank sample is the starting solution of hexaglycine, that, as far as Gly-related ESI signals are concerned, produced only the signal m/z= 361 of 6-Gly, providing evidence of the stability of this oligopeptide towards self-hydrolysis in the adopted condition (panel a). In a second blank test, 6-Gly is incubated in solution with commercial His-Ser peptide (m/z= 243): again, no evidence of any hydrolysis of hexaglycine is found (panel b). In the two cases of 6-Gly incubated with the solutions of catalytically produced peptides (panels c, d), in addition to the signals hexaglycine, Ser and His in monomeric form (m/z =106 and 156, respectively), Ser-based homopeptides (m/z= 193, 2-Ser; 367, 3-Ser), His-based homopeptides (m/z= 293, 2-His; 430, 3-His), and Ser-His and His-Ser heteropeptides (m/z= 243) are found. Moreover, the signal due to glycine in monomeric form (m/z= 76) is detected. Hence, a hydrolysis of 6-Gly apparently occurred, but two contradictory scenarios seem to be present. Data in panel c deals with the system where the heteropeptide expected to have been produced is His-Ser, found ineffective towards 6-Gly hydrolysis in the relevant bank test (panel

b), whilst data in panel d, dealing with the system where the heteropeptide expected to have been produced is Ser-His, appear in agreement with the hydrolysis activity proposed for this peptide. [23-25]

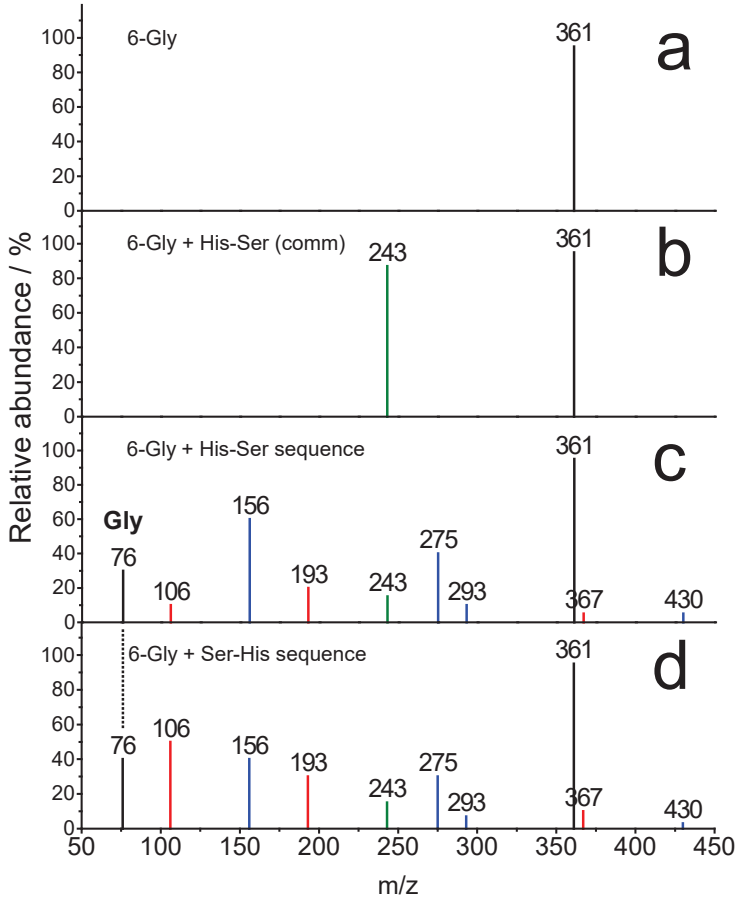

Figure 7. ESI-MS spectra of: a) 10 ppm of 6-Gly solution a such, then mixed in a 1:1 ratio in vol with b) a 10 ppm commercial His-Ser solution; c) washing solution from adsorption of His-Ser sequence on TiO_2; d) washing solution from adsorption of Ser-His sequence on TiO_2. Numbers on the bars are the m/z values, without decimal digits, for the sake of simplicity. Original HR-MS spectra with complete m/z values are reported in Appendix A.

A possible rationalization is as follows: when Ser and His (or vice-versa) are consecutively adsorbed on the catalyst, the carboxylic group of both aa monomers are activated by the interaction with the surface. It can then react with the amino group of any other neighbor aa, resulting in the formation of both Ser-His and His-Ser peptides (other than in the formation of homopeptides). Finally, the discussion of the hydrolytic mechanism of 6-Gly is outside the scope of this report. Nevertheless, it can be noticed that the presence at the end of the incubation of both unreacted hexamer and of product Gly in monomeric form as the only hydrolysis

product suggests that once the hydrolysis of a peptide bond occurred, the subsequent hydrolysis of the shorter peptides produced might be quite fast.

Conclusions

The collection of results reported and commented above allows to conclude that short homopeptides of Ser and His (up to 3-terms), Ser-His and His-Ser heteropeptides can be produced by adsorbing vapors of these amino acids on TiO_2 nanoparticles. The pros of the method adopted for the synthesis of these peptides are the absence of chemical activation of amino acids and the absence of solvent. However, the main con is the (still) lack of selectivity. In particular, in the formation of hetero-dipeptides, the attainment of the desired sequence is not guaranteed be the admission of reactants in the correct sequential order. Furthermore, a contribution to the debate on the hydrolase activity of Ser-His is provided, in terms of evidence of activity in promoting the hydrolysis of hexaglycine. The origin of discrepancy with the absence of any significant hydrolytic activity reported by MacDonald et al. [28] can be the absence of significant electronic and steric effect of H atoms as lateral chain in the oligopeptide used in this work. On the other hand, it will be interesting to investigate if the hydrolytic activity of Ser-His towards bio-macromolecules reported by the group of Zhao [23, 25] shows any selectivity towards peculiar positions along the polymeric sequence.

Experimental Details

Titanium dioxide thermal treatment

The titanium dioxide powder was compressed into a self-supporting pellet (*optical thickness* ca. 10 mg/cm^2) and thermally treated in vacuum (residual pressure $1.0 \cdot 10^{-5}$ mbar) to remove previously adsorbed molecules and water. The samples were heated inside the cell under dynamic vacuum from room temperature to 723 K (ca. 5 K/min) and outgassed at this temperature for 1 hour. To compensate for the reductive effect on TiO_2 produced by this dehydration/dehydroxylation treatment, 6 mbar of O_2 were admitted in the cell, and kept in contact with the samples for 1 hour at 723 K. The system was subsequently let to cool down to 473 K in O_2 and finally outgassed until reached room temperature. The treated samples appeared perfectly white, as expected for stoichiometric TiO_2.

Sublimation of amino acids

The cell with the treated TiO_2 is transferred into a nitrogen filled glovebox for the introduction of the amino acids. The amino acids powders are compressed as well into self-supported pellets (ca. 150 mg) and moved close to the TiO_2 pellet. The cell is then connected to a vacuum line for the subsequent sublimation process where the TiO_2/amino acid system is outgassed. The sublimation process is the same already described by Martra et al. [16] in their SI for the glycine amino acid. Briefly, the amino acid and the oxide pellets are placed close to each other within a section of the infrared cell, acting as a reactor, and heated up in static vacuum to the sublimation temperature of the amino acid. A liquid nitrogen trap is present during the whole sublimation process in order to remove generated water from the system. Typical sublimation steps can last from 20 to 60 minutes and can be repeated until the amino acid pellet is consumed. Ser is adsorbed at 433 K, while His sublimations are carried out at 473 K. For the hetero-peptides experiments, after the first amino acid is sublimated, the cell is moved into a nitrogen filled glovebox and the amino acid pellet is replaced with the other one, then the sublimation of the second amino acid is carried out. For these experiments, each amino acid sublimation lasts 1 hour.

CO_2 coverage evaluation

In order to monitor the degree of coverage of the titanium dioxide surface by amino acids molecules, linearly adsorbed CO_2 was employed as probe molecule. A mixture of $^{12}CO_2$ and $^{13}CO_2$ was specifically prepared in ration of 9:1 and the infrared signal of the isotopically labelled molecule was monitored. After each experimental step, oxide thermal treatment and sublimation steps, CO_2 mixture at 50 mbar is dosed in the cell with the previously outgassed samples and left in contact for 10 minutes after which an IR spectrum is collected. The system is then outgassed for 20 minutes

to remove CO_2 pressure. Some carbonates and bicarbonates are formed during this analysis for the reaction of the linearly adsorbed CO_2 with the basic sites of titanium dioxide: beside being a minor component, these species are removed within the temperature ramping of the subsequent sublimation step. We found this method to be effective with Ser, while in the case of His, probably due to the basicity of the side chain, the procedure could not be reliable. For this latter amino acid, coverage estimations were made comparing the optical density of the titanium dioxide pellet with one used in a serine experiment and correlate those values to obtain the percentage of surface coverage.

Infrared measurements

The whole experimental work is monitored by means of *in situ* IR spectroscopy. The spectra were collected at beam temperature (ca. 323 K) with a resolution of 4 cm^{-1}, averaging 100 scans to attain a good signal-to-noise ratio, in a Bruker Vector 22 equipped with a LaDTGS detector.

Products extraction and Mass Spectrometry analysis

At the end of the spectroscopic measurements, the samples were removed from the cell, manually ground in an agate mortar and suspended in 0.5 mL of Milli-Q water (Millipore system). The suspension was shaken for 15 min by a Vortex mixer and then centrifuged for 5 min at 10k rpm. After removal of the supernatant, the solid was treated a second time with the same volume of water. The two aliquots of the aqueous solutions were then mixed, and analyzed by high-resolution mass spectrometry. The washed samples were dried under flowing nitrogen, pelletized and inserted into the IR cell for the subsequent measurements, that were carried out after outgassing at b.t and admission/outgassing of D_2O at 20 mbar, until invariance of the spectra.

High-resolution mass spectrometry analyses of the washing solutions were performed using an LTQ Orbitrap mass spectrometer (Thermo Scientific) equipped with an atmospheric pressure interface and an electrospray ionization (ESI) source. The source voltage was set to 4.48 kV. The heated capillary temperature was maintained at 538 K. The tuning parameters adopted for the ESI source were: capillary voltage 0.02 V, tube lens 24,77 V; for ions optics: multipole 0 offset −4.28 V, lens 0 voltage −4.36 V, multipole 0 offset −4.28 V, lens 1 voltage −13.69 V, gate lens voltage −8.84 V, multipole 1 offset −18.69 V, front lens voltage −5.09 V. Mass accuracy of recorded ions (vs calculated) was ± 1 mmu (without internal calibration). Samples, added of 100 μL of a 0.1 M HCOOH aqueous solution, were delivered directly to the mass spectrometer via a Hamilton microliter syringe at constant flow (10 μL/min).

References

[1]. T. Uhlig, T. Kyprianou, F. G. Martinelli, C. A. Oppici, D. Heiligers, D. Hills, X. R. Calvo and P. Verhaert *EuPA Open Proteomics* **2014** (4) 58-69.
[2]. K. Fosgerau and T. Hoffmann *Drug Discovery Today* **2015** (20) 122-128.
[3]. V. R. Pattabiraman and J. W. Bode *Nature* **2011** (480) 471-479.
[4]. M. Rodriguez-Garcia, A. J. Surman, G. J. T. Cooper, I. Suárez-Marina, Z. Hosni, M. P. Lee and L. Cronin *Nature* **2015** (6) 8385.
[5]. J.-F. Lambert *Origins Life Evol. Biospheres* **2008** (38) 211-242.
[6]. A. R. Mitchell *Pept. Sci.* **2008** (90) 175-184.
[7]. J. M. Collins, K. A. Porter, S. K. Singh and G. S. Vanier *Org. Lett.* **2014** (16) 940-943.
[8]. T. M. El Dine, J. Rouden and J. Blanchet *Chem. Commun.* **2015** (51) 16084-16087.
[9]. C. Guo, J. S. Jordan, J. L. Yarger and G. P. Holland *ACS Appl. Mater. Interfaces* **2017** (9) 17653-17661.
[10]. T. Georgelin, M. Akouche, M. Jaber, Y. Sakhno, L. Matheron, F. Fournier, C. Méthivier, G. Martra and J.-F. Lambert *Eur. J. Inorg. Chem.* **2017** (2017) 198-211.
[11]. E.-i. Imai, H. Honda, K. Hatori and K. Matsuno *Origins Life Evol. Biospheres* **1999** (29) 249-259.
[12]. M. Meng, L. Stievano and J.-F. Lambert *Langmuir* **2004** (20) 914-923.
[13]. U. Shanker, B. Bhushan, G. Bhattacharjee and Kamaluddin *Origins Life Evol. Biospheres* **2012** (42) 31-45.
[14]. Y. Furukawa, T. Otake, T. Ishiguro, H. Nakazawa and T. Kakegawa *Origins Life Evol. Biospheres* **2012** (42) 519-531.
[15]. T. Munegumi and N. Tanikawa *Origins Life Evol. Biospheres* **2017**
[16]. G. Martra, C. Deiana, Y. Sakhno, I. Barberis, M. Fabbiani, M. Pazzi and M. Vincenti *Angew. Chem. Int. Ed.* **2014** (53) 4671-4674.
[17]. D. Gross and G. Grodsky *J. Am. Chem. Soc.* **1955** (77) 1678-1680.
[18]. O. D. Ekici, M. Paetzel and R. E. Dalbey *Protein Sci.* **2008** (17) 2023-2037.
[19]. G. M. Simon and B. F. Cravatt *J. Biol. Chem.* **2010** (285) 11051-11055.
[20]. K. L. Duncan and R. V. Ulijn *Biocatalysis* **2015** (1) 67.
[21]. S. Hatfield, Y. Li, Y. Zhao, R. Wan, M. McMills, J. Li and X. Chen *FASEB J* **2000** (14) A1323-A1323.
[22]. Y. S. Li, Y. F. Zhao, S. Hatfield, R. Wan, Q. Zhu, X. H. Li, M. McMills, Y. Ma, J. Li, K. L. Brown, C. He, F. Liu and X. Z. Chen *Bioorg. Med. Chem.* **2000** (8) 2675-2680.
[23]. J. Chen, R. Wan, H. Liu, C. M. Cheng and Y. F. Zhao *Lett. Pept. Sci.* **2000** (7) 325-329.
[24]. H. L. Du, Y. T. Wang, L. F. Yang, W. X. Luo, N. S. Xia and Y. F. Zhao *Lett. Pept. Sci.* **2002** (9) 5-10.

[25]. Y. Ma, X. Chen, M. Sun, R. Wan, C. Zhu, Y. Li and Y. Zhao *Amino Acids* **2008** (35) 251-256.
[26]. M. Sun, Y. Ma, S. H. Ji, H. N. Liu and Y. F. Zhao *Bioorg. Med. Chem. Lett.* **2004** (14) 3711-3714.
[27]. P. Y. Chen, Y. Liu, X. Gao, N. S. Xu, J. Niu, S. Y. Liu and Y. F. Zhao *Phosphorus Sulfur Silicon Relat. Elem.* **2011** (186) 933-935.
[28]. M. J. MacDonald, L. D. Lavis, D. Hilvert and S. H. Gellman *Org. Lett.* **2016** (18) 3518-3521.
[29]. C. Deiana, E. Fois, S. Coluccia and G. Martra *J. Phys. Chem. C* **2010** (114) 21531-21538.
[30]. P. I. Haris and D. Chapman *Biopolymers* **1995** (37) 251-263.
[31]. K. Hasegawa, T.-a. Ono and T. Noguchi *J. Phys. Chem. B* **2000** (104) 4253-4265.
[32]. N. B. Colthup, L. H. Daly and S. E. Wiberley *Chapter 5 - Methyl and Methylene Groups* in Introduction to Infrared and Raman Spectroscopy (Third Edition) **1990** (Academic Press, San Diego)
[33]. L. J. Bellamy and S. Krimm *The infrared spectra of complex molecules* in Journal of Polymer Science: Polymer Letters Edition **1975** (John Wiley & Sons, Inc., New York)
[34]. A. Rimola, Y. Sakhno, L. Bertinetti, M. Lelli, G. Martra and P. Ugliengo *J Phys Chem Lett* **2011** (2) 1390-1394.
[35]. P. Yang, R. Xu, S. C. Nanita and R. G. Cooks *J. Am. Chem. Soc.* **2006** (128) 17074-17086.

Appendix A

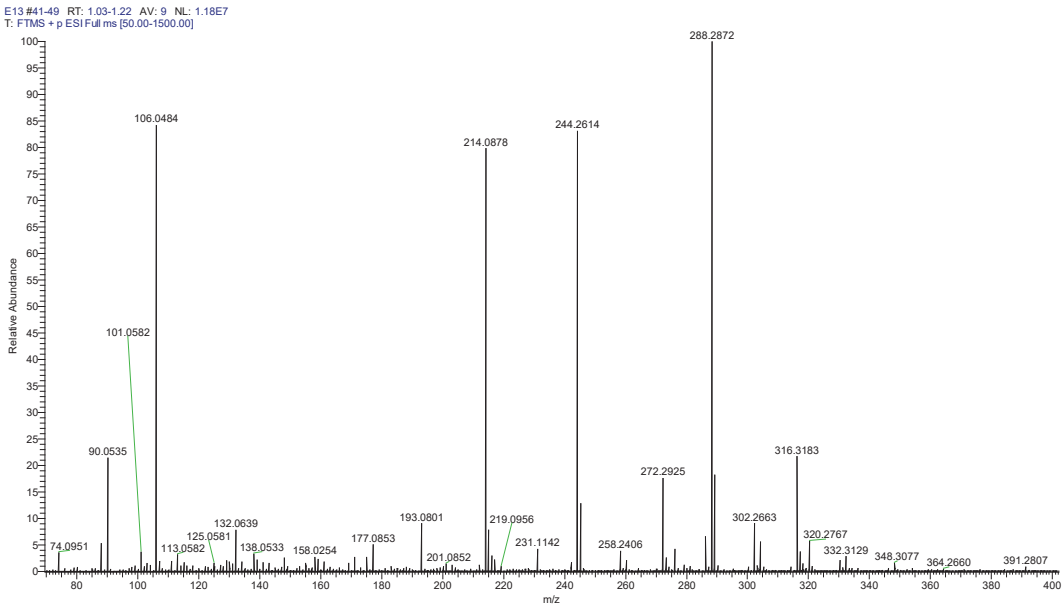

Figure 8. HR-MS spectrum of washing solutions of 2 hours Serine sublimation on TiO_2.

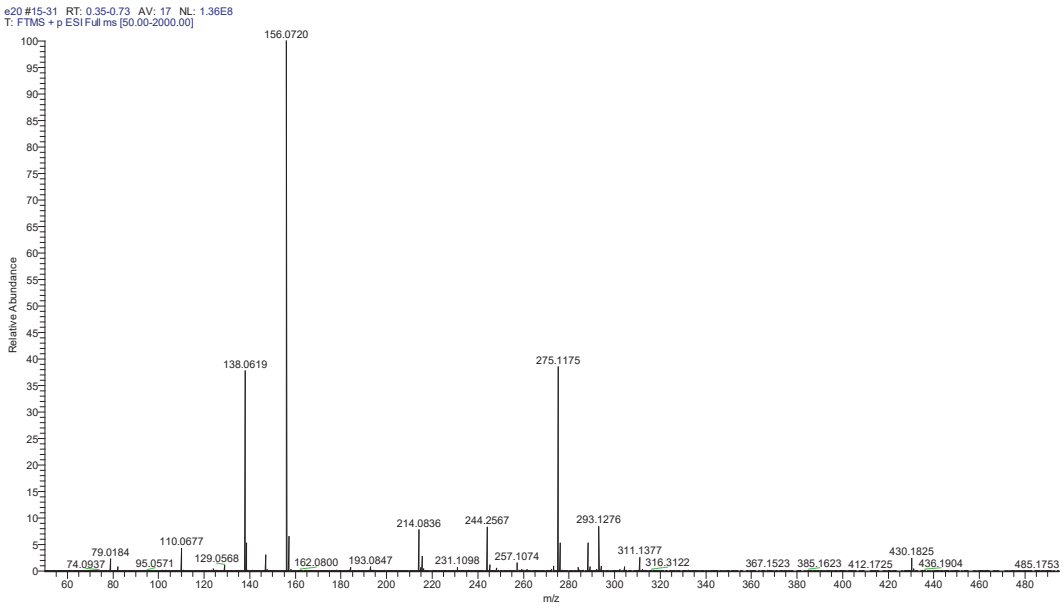

Figure 9. HR-MS spectrum of washing solutions of 2 hours Histidine sublimation on TiO_2.

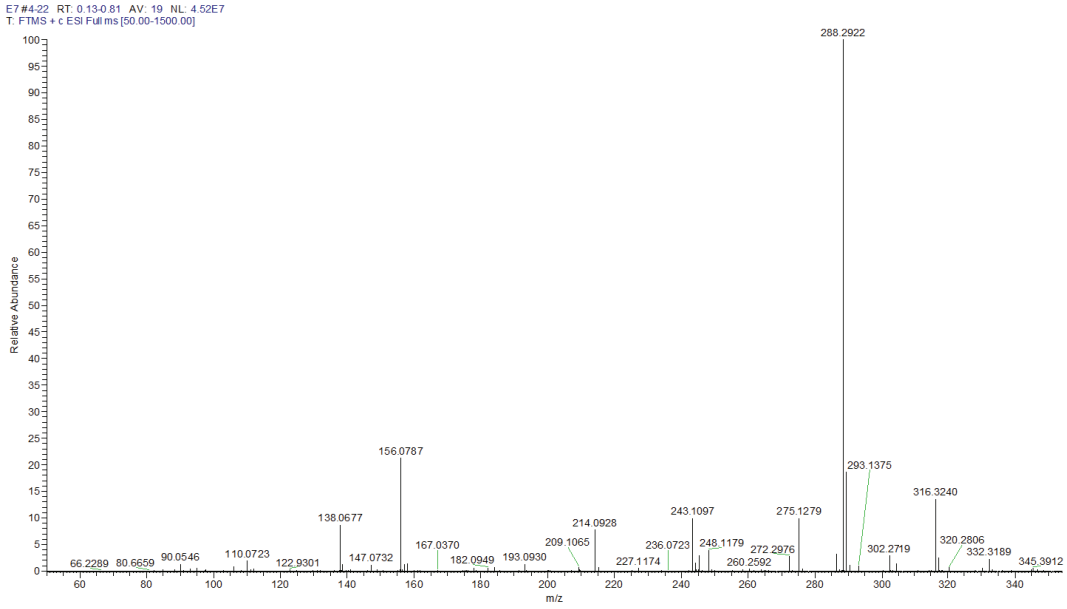

Figure 10. HR-MS spectrum of washing solution of Ser-His sublimation sequence on TiO_2.

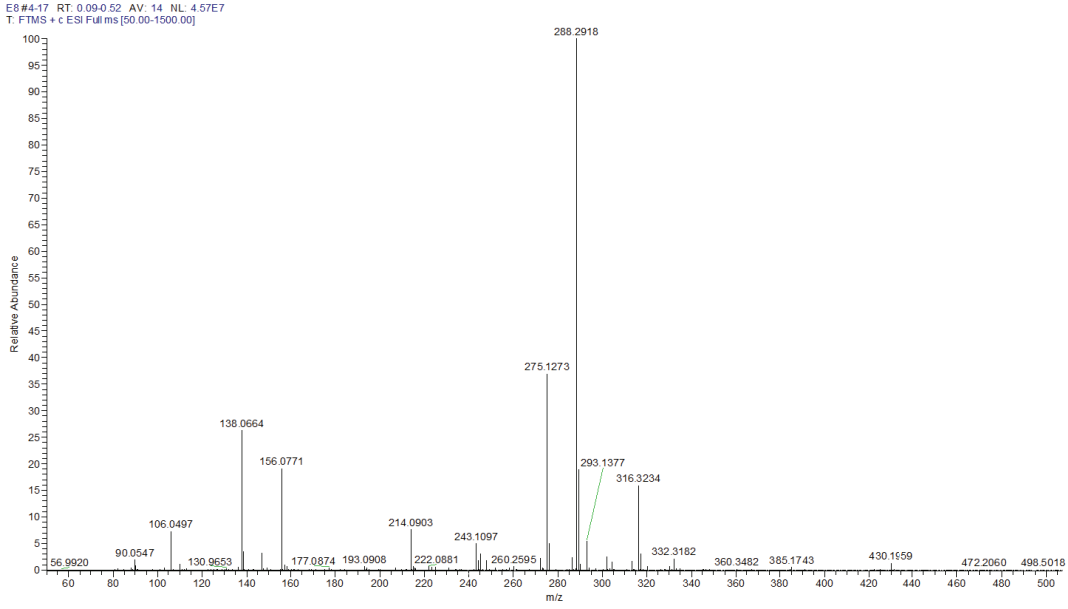

Figure 11. HR-MS spectrum of washing solution of His-Ser sublimation sequence on TiO_2.

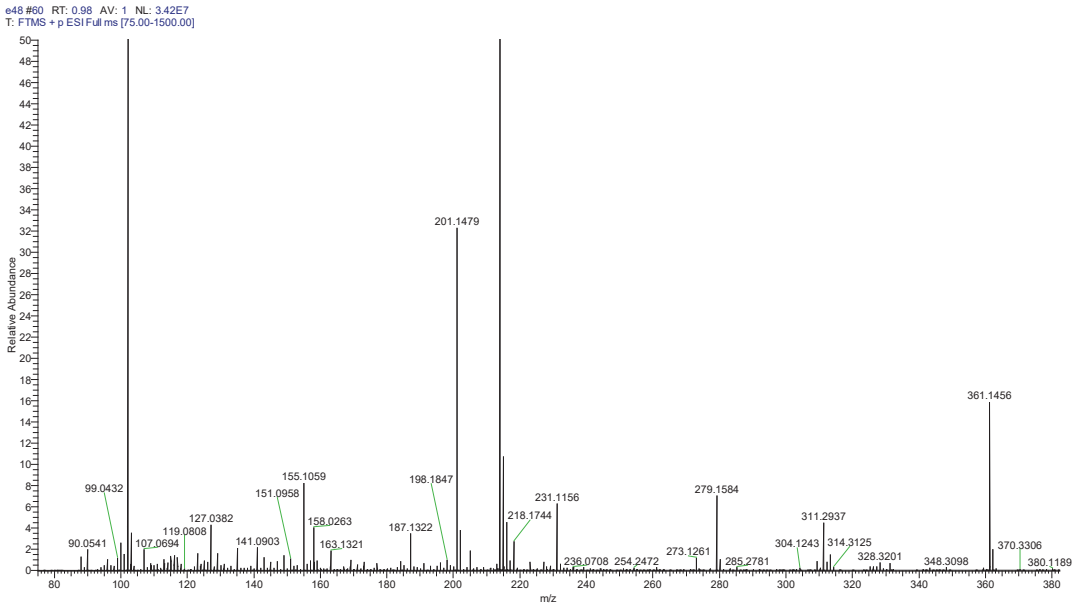

Figure 12. HR-MS spectrum of 10 ppm hexaglycine solution, incubated for 12 hours.

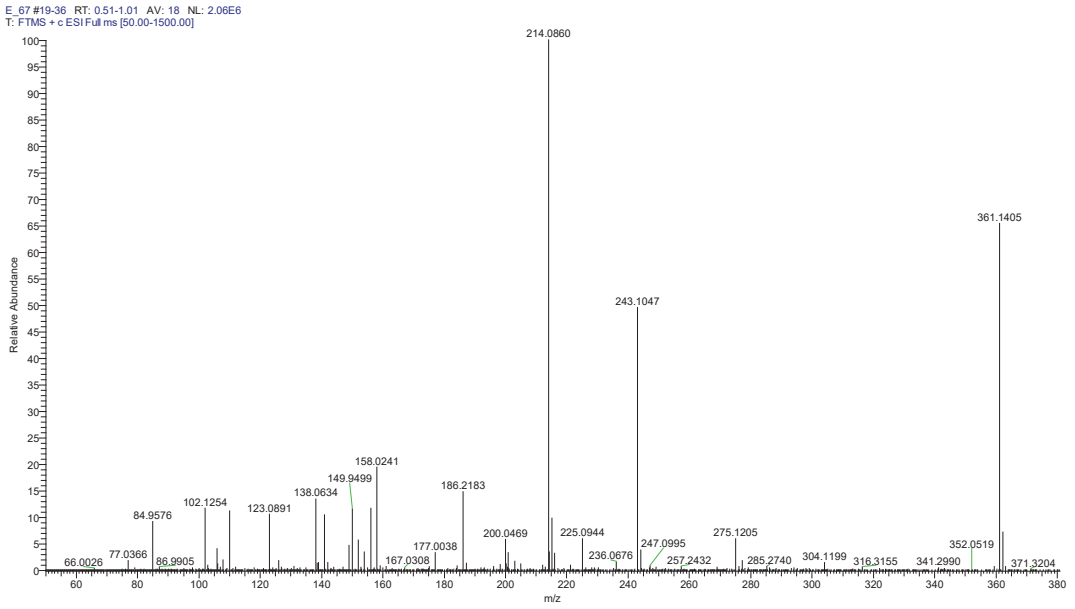

Figure 13. HR-MS spectrum of 10 ppm hexaglycine solution, incubated for 12 hours with 10 ppm of the commercially available His-Ser dimer.

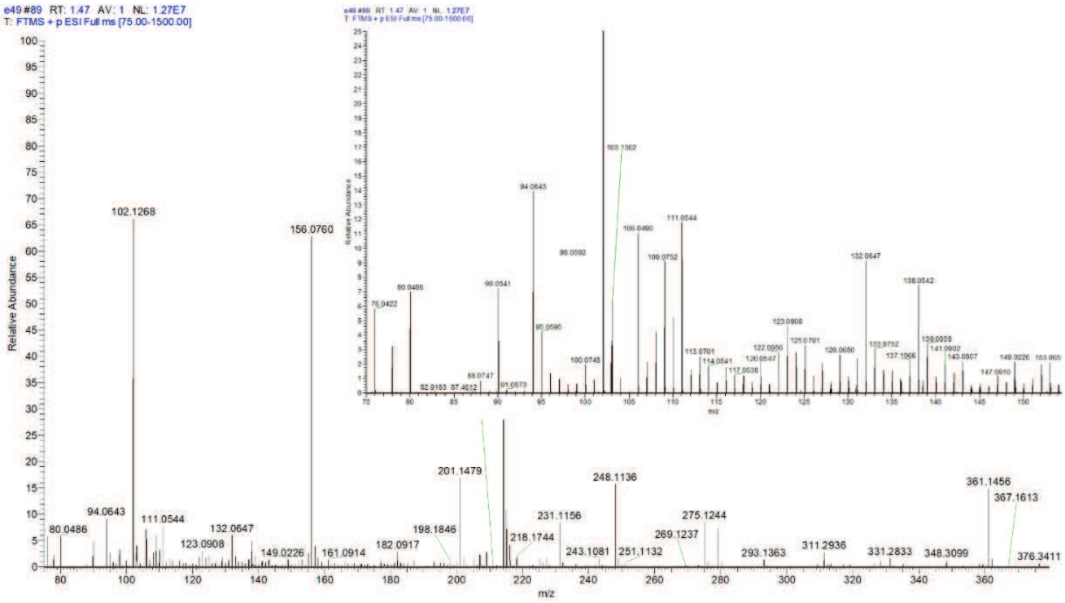

Figure 14. HR-MS spectrum of 10 ppm hexaglycine solution, incubated for 12 hours with washing solution from Ser-His sublimation sequence on TiO_2. Inset: zoomed view in the 75-150 m/z range.

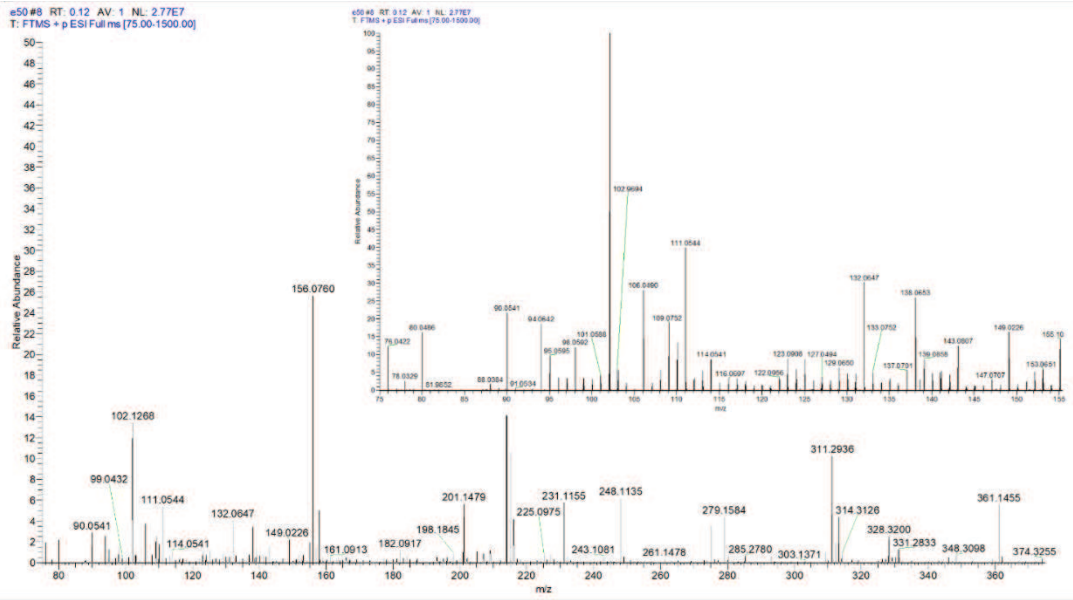

Figure 15. HR-MS spectrum of 10 ppm hexaglycine solution, incubated for 12 hours with washing solution from His-Ser sublimation sequence on TiO_2. Inset: zoomed view in the 75-150 m/z range.

Appendix B

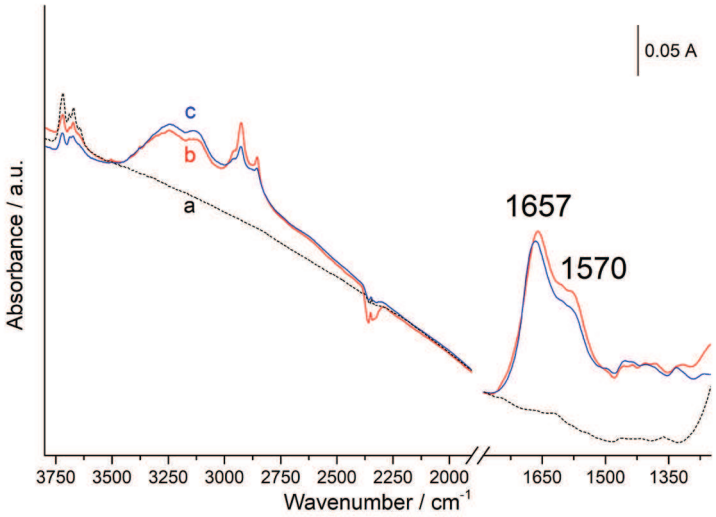

Figure 16. IR spectra of heteropeptides experiments. Curve a) bare TiO_2 surface after dehydration at 723 K; curve b) after 1 hour Ser sublimation at 433 K and 1 hour His sublimation at 473 K; curve c) after 1 hour His sublimation at 473 K and 1 hour Ser sublimation at 433 K.

Chapter Six

Zeolite composite materials for technological applications

The scientific work is carried out in the frame of a new-born project concerning the employment of zeolite materials for applications in sensing devices and fine chemistry: Zapping (www.zapping-prin.it). This opportunity meets the natural progression of my PhD project, where zeolites represent a natural crystalline microporous alumino silicates with periodic arrangements of cages and channels that could have played an important role in the concentration of amino acids and nucleic acids in a prebiotic era serving as "primitive cells". [1] All the work shown in this chapter was carried out under the supervision of Dr. Ing. Di Renzo at Institut Charles Gerhardt of Montpellier during the 6 month abroad period.

Project Generals

Beyond their traditional applications as shape-selective catalysts, selective absorbers and cation exchangers, zeolites - thanks to their structure and chemistry - can be considered as small chemical laboratories, where reactions can be obtained and promoted. High pressure is an ideal tool for implementing chemical reactions, induced by purely mechanical methods tuning the intermolecular/interatomic distances and leading to a rearrangement of chemical bonds. ZAPPING project aims to merge the potentialities of high-pressure technologies with microporous materials properties, to induce and control chemical reactions proved effective in driving the formation of arrays with desired dimensionality. ZAPPING is a challenging interdisciplinary project in which the synergy of the competences of scientists coming from different material science areas (mineralogy, chemistry, physics, computational physical-chemistry, chemical-engineering) will be exploited to gain knowledge on the organization of confined supramolecular nano-systems. Within the ZAPPING project, is exploited the porous template effectiveness of zeolites in inducing the aggregation and oligomerization/polymerization along preferential directions, not easily achievable under bulk, nor confined conditions. This will allow the development of functional materials with enhanced functionalities, such as confined polymers with low dimensionality, to be integrated in devices (i.e. gas sensing devices). Two main systems will be targeted, both based on the exploitation of host zeolites: i) alkynes + zeolite: to promote the polymerization of hydrocarbons to give conductive polymers. [2] These composite materials will be exploited for environmental purposes, integrating them in gas

sensors sensitive to air pollutant like sulphur dioxide, carbon monoxide, nitrogen dioxide, and volatile organic compounds; ii) non-activated amino acids + zeolite: to induce the condensation of amino acids by a solvent-free, "green" peptide synthesis. In fact, the formation of amide/peptide bonds in sustainable conditions represents a challenge in the field of the synthesis of fine chemicals in an "atom economy regime", and will open the way on new synthesis strategies. Moreover, the investigated process could provide insights useful for shading light on amino acids polymerization under abiotic conditions, which is a still open issue in prebiotic chemistry.

Zeolites System Requirements

The first task that has to be addressed is the choose of zeolites that needed to meet the project requirements. Among the many possibilities that the framework panorama offers, a set of selection criteria was applied in order to obtain the wanted properties. The zeolite affinity for water will be the main criterion driving the choice. In fact, the attitude of hydrophobic frameworks in repelling water molecules will reduce the main practical problem of the gas sensors, connected to the ambient moisture. On the other hand, the condensation reaction forming amide/peptide bonds releases water, and hence it should be favoured by the presence of hydrophilic sinks able to remove the water molecules from the sites where the reaction occurs. Specific framework types are selected according to the following specific needs: i) the dimensions of the pores must accommodate the molecules of interest. For the smallest alkynes (acetylene) channels have an optimal diameter not larger than 5 Å, for both the largest alkynes and amino acids (such as Gly, Ala, Ser, His) the channel diameters should be about 6-7 Å; ii) to promote the synthesis of isolated 1D polymer chains and to favour the coaxing of the amino acids to obtain condensation, the framework must have a mono-dimensional channel system; iii) in the case of sensor devices, a residual porosity should be maintained after polymerization / condensation to allow the gas transit; iv) for peptide formation, the zeolite must provide the water sinks needed for successful amide condensation. While the first two requirements can be fulfilled by several high-silica zeolite networks, the third and fourth requirements demand peculiar zeolite frameworks. Effective gas circulation in sensing composites requires two monodimensional non-intersecting, but communicating, parallel channels with different diameters, one larger channel for the condensation reaction and one smaller for gas/water diffusion. The contact between the two channels will be ensured by sufficiently large windows between them. Albeit some phosphate-based networks fulfil this requirement, their stability in working conditions is unsatisfactory and hence the

MOZ-type zeolite, properly de-aluminated, is the election framework. In order to explore a further possibility, also the LTF framework is considered in the synthesis workflow for its similarity with the MOZ one. For the synthesis of peptides, MOR-type zeolites feature a linear 6 Å channel suitable for amino acids condensation and side pockets in which appropriate cations are effective water scavengers. Both natural Ca-MOR and synthetic Na-MOR are potentially appropriate for this application.

Frameworks Overlook

LTF and MOZ share the same [001] projection of the framework (*xy* plane), however, the up-down orientations of tetrahedra and therefore their connectivity is different along the z axis. Figure 1 shows a schematic representation of LTF (a and b) and MOZ (a and c) frameworks structures.

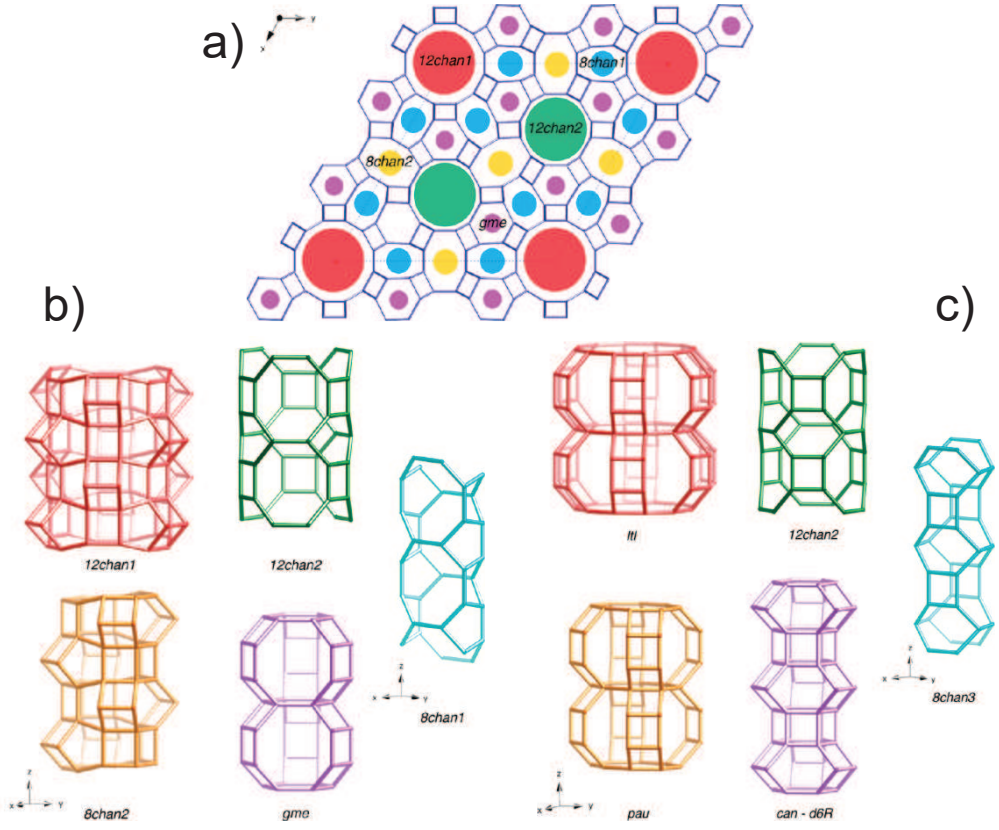

Figure 1. Schematic representation of LFT and MOZ frameworks. a) [001] projection on the *xy* plane of the common structure structure; b) LTF and c) MOZ developments along the xz and yz planes.

Colour coding of the [001] projected structure corresponds to the structures along the z axis. Bridging oxygen atoms omitted for the sake of clarity. [3]

In MOZ, two different 12-ring channels (*12chan1* and *12chan2* in Figure 1) are parallel to *z* axis which are connected differently. The two-dimensional 8-ring channels, intersecting the 12-ring channels, are perpendicular to the *z* axis and run along three symmetrically equivalent directions.

The MOR-type material presents the framework shown in Figure 2.

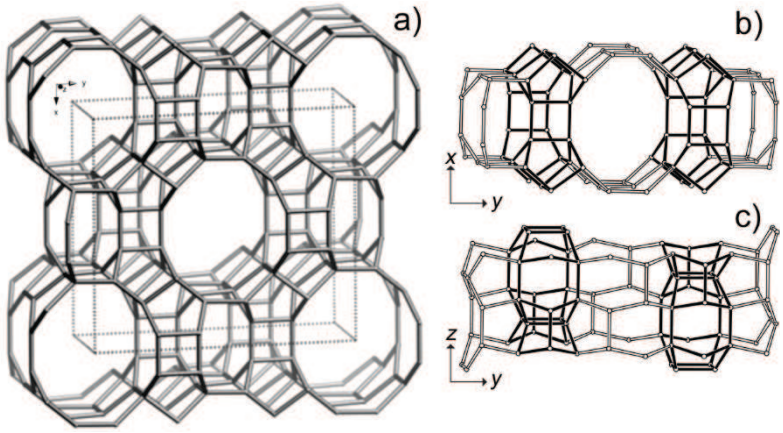

Figure 2. Schematic representation of MOR framework. a) [001] projection on the *xy* plane of the structure; 8-Ring channels and 12-ring channels, linked along *y* axis through interconnecting cavities (in bold) that are part of the wall of the sinusoidal channel parallel to *y*, b) viewed along *z* axis and c) along *x* axis.

In MOR there are sinusoidal channels (with limiting 8-ring windows) parallel to *y* axis that intersect with one-dimensional 8- and 12-ring channels parallel to the *z* axis. The side channels interconnections form the so called "pockets" which are exploited in the amino acids polymerization as water scavenger.

Zeolites Synthesis

Typically, zeolite synthesis is carried out under hydro(solvo)thermal conditions where the reaction takes place within a sealed container (autoclave) that can reach high temperatures and pressures.
The general recipe for a zeolite is made of three reagents: a Si source, which is usually bare silica power or in a colloidal solution; an Al source that can be either aluminium metal or a soluble salt; and a structure-directing agent (SDA) depending on the type of framework wanted, is an hydrated cation or an organic compound. The approach consisted in following the original patented recipe for LZ-135 (LTF) by Marcus [4] and ZSM-10 (MOZ) by Ciric [5] and slightly changing the parameters of the preparation. Mixing all regents generates a gel that can be aged from 12 to 72 hours and then crystallized in the autoclave for several days. In the case of the MOR-type framework, a commercially synthetized material is chosen and it is used for post synthesis treatments (discussed in the next section).

Materials and Methods

LZ-135: sodium hydroxide and sodium aluminate were dissolved in an approximately equivalent weight of water and stirred until the solution is clear. This solution was mixed within a 100 mL stainless steel autoclave together with Ludox-HS 35% w/w colloidal silica source and hand-stirred for 20 minutes. To the resulted thin gel was added the templating agent solution made of tetraethylammonium bromide (TEA-Br) and tetramethylammonium bromide (TMA-Br) salts dissolved in the remainder of the water. The final gel was stirred until homogeneous (about 5 minutes) and then sealed to be crystallized at the indicated times (t) and temperatures (T). The molar ratios of the primary LTF gel are reported in Table 1.

Table 1. Molar ratios and synthesis conditions for the LZ-135 synthesis. Samples are sorted by increasing crystallization time.

Sample name	Na	TMA	TEA	Al	Si	H_2O	Si/Al	OH/Si	T / °C	t / h
MFA13	0.90	0.71	1.00	0.50	1.00	31.40	2.00	0.40	100	7
MFA14	0.80	0.71	1.00	0.45	1.00	31.40	2.22	0.35	100	7
MFA8	0.37	0.20	0.30	0.18	1.00	21.68	5.46	0.19	100	13

ZSM-10: aluminium grains were slowly dissolved in a magnetically stirred KOH solution under mild heating. After 3.5 hours, the solution is cooled down to room temperature and the dimethyl-1,4-diazabicyclo-2,2,2-octane (dm-DABCO) is added. Meanwhile, a solution of silica (Aerosil 200) was prepared dissolving the powder in a KOH solution with a proportional water amount, hand-stirred to form

a gel and then added to the first solution. The mixture was stirred until homogenous and successively sealed in the autoclave for the aging time and later crystallization at the indicated times (t) and temperatures (T). The molar ratios of the primary MOZ gel are reported in Table 2.

Table 2. Molar ratios and synthesis conditions for the ZSM-10 synthesis. Sample are sorted by increasing crystallization time. Time is reported in days of ageing + days of crystallization at T (°C).

Sample name	K+	dmDABCO	Al	Si	H2O	Si/Al	OH/Si	T	time
MFA11	0.61	0.15	0.13	1.00	23.39	7.48	0.47	100	2 + 7
MFA32	0.53	0.08	0.13	1.00	23.38	7.48	0.39	100	1 + 11
MFA21	0.61	0.15	0.13	1.00	23.39	7.48	0.47	80	3 + 41

Dm-DABCO-I_2 was synthesised from DABCO by methylation with CH_3-I carried out under reflux for 3 hours in methanol following the procedure by Wempe et al. [6] DABCO-I_2 powder was placed in a balloon with methanol under stirring at room temperature, when completely solubilized the iodo-methane was added drop by drop and then the reaction was carried out at 110 °C under reflux for 3 hours where the initial colourless solution slowly becomes light-yellowish and precipitate appeared almost instantly. After the reaction completion, the balloon was ice-cooled and then vacuum filtered, washing the product three times with small volume of ethyl acetate. The wet white powder was collected and the remaining solvent was evaporated in a rota-vapour system and subsequently dried in vacuum for storage.

The *aging process* is carried out at room temperature, while for the crystallization the autoclave is moved into an oven. When the synthesis is over, the products are vacuum filtrated and dried at room temperature or at 80°C inside a ventilated oven.

Powder X-ray diffraction (XRPD) patterns were collected on a Bruker AXS D8 diffractometer, with Bragg-Brentano geometry and equipped with a Bruker Lynx Eye detector, using a Cu Kα (λ = 1.54184 Å) as X-ray source. The data were recorded in the 4 - 50 (2θ) to identify the products peaks using an angular step size of 0.0197° and a counting time of 0.2 s per step.
Morphological characterization of the most interesting samples was performed using a Hitachi S-4800 I Scanning Electron Microscope (SEM).

Discussion

For the sake of clarity, in this section are reported and discussed the most interesting samples out of the total number of synthesis (more than fifty preparations over the whole time span).

The LZ-135 preparations led to a complex XRPD pattern, resulting from the combinations of different contributions mainly assignable to Na P zeolite, sodalite (SOD), mazite (MAZ) and a small amount of LZ-135 (Figure 3). From top to bottom the XRD patterns show the constant presence of the compact phase SOD, while only MFA8 (top) possess hints of a MAZ type of framework. Moving from MFA13 to MFA14 (middle and bottom) the samples show the presence of a NaP zeolite phase and the LZ-135 pattern begins to arise. Despite finding the signals of the wanted structure, these syntheses were not satisfying enough to produce a material actually employable for the final study. In this sense, the synthesis conditions need to be improved to obtain a usable material.

Different is the case of the MOZ framework. Figure 6 collects the results of the ZSM-10 syntheses, which actually produced, in all three case shown here, the wanted material. From top to bottom, the ZSM-10 pattern grows even though the material appears to be nanocrystalline. Further morphological analysis shown in Figure 7 confirm what observed in the XRD patterns, displaying in all three cases, sub-micrometric aggregates with further nanostructuration.

This is a promising material and the next efforts will be devoted in the production of bigger crystals that can be studied also with the DAC and IR techniques.

Figure 3. XRPD patterns of LZ-135 samples. Top: MFA8 synthesis compared to LZ-135, MAZ and SOD frameworks. Middle: MFA13 synthesis compared to NaP zeolite, LZ-135 and SOD frameworks. Bottom: MFA14 synthesis compared to NaP zeolite, LZ-135 and SOD frameworks.

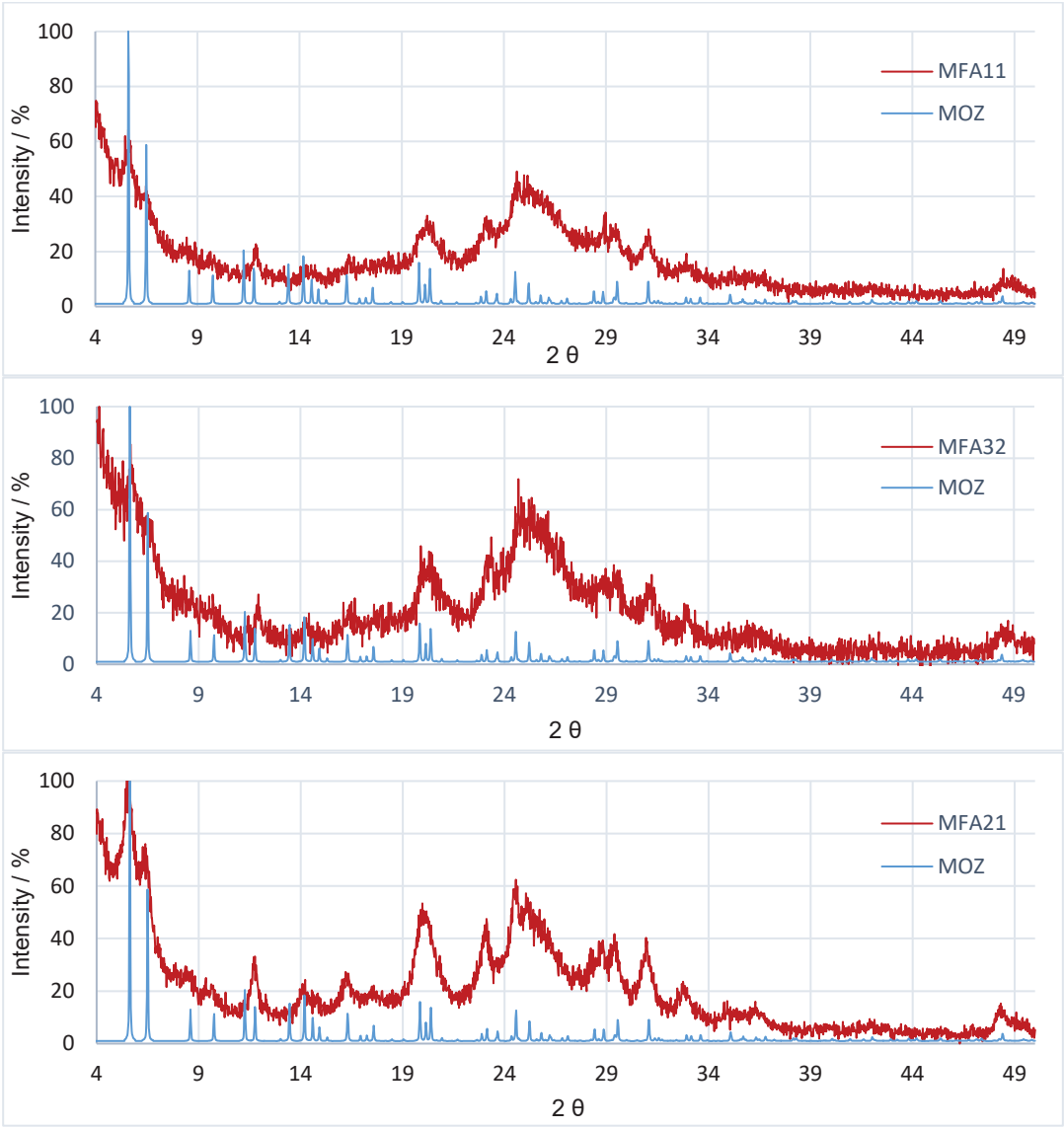

Figure 4. XRPD patterns of ZSM-10 synthesis. Top: MFA11. Middle: MFA32. Bottom: MFA21. The samples are compared with the MOZ framework.

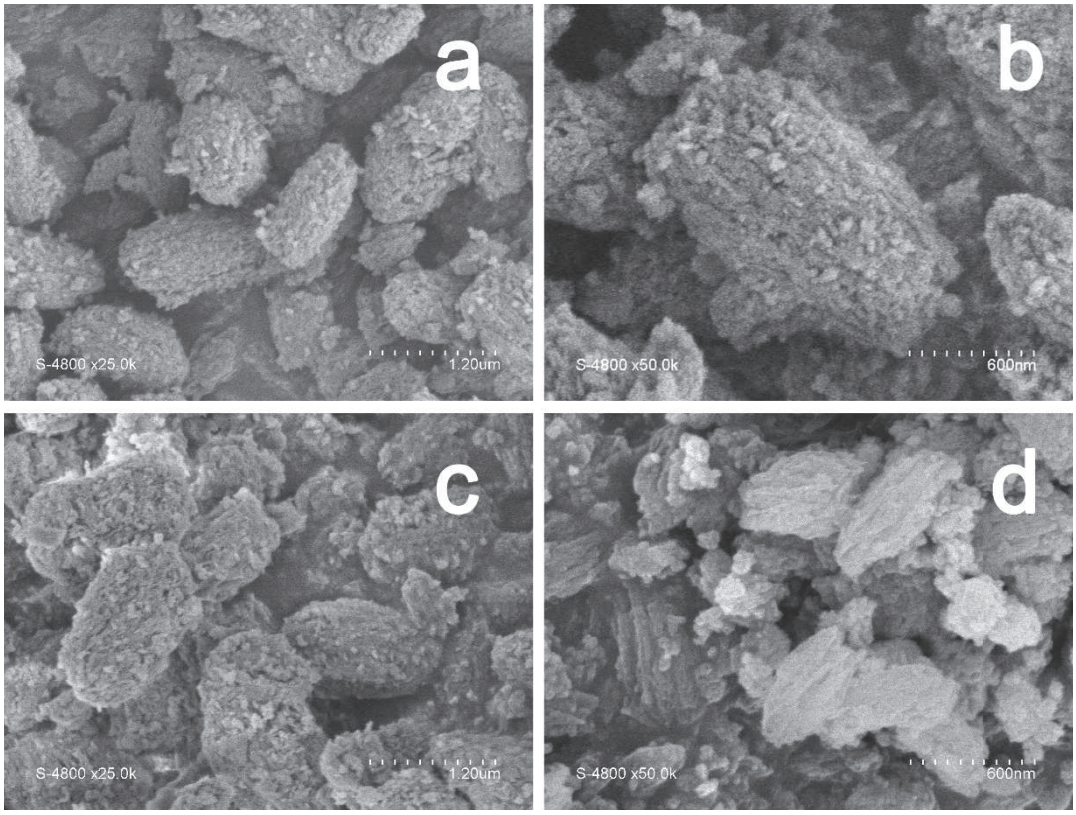

Figure 5. SEM images representative of a, b) MFA21; c) MFA32 and d) MFA11 samples.

References

[1] Anizelli P. R., Baú J. P. T., Gomes F. P., da Costa A. C. S., Carneiro C. E. A., Zaia C. T. B. V. and Zaia D. A. M. *Origins Life Evol. Biospheres* **2015** (45) 289-306.
[2] Santoro M., Gorelli F. A., Bini R., Haines J. and van der Lee A. *Nat. Commun.* **2013** (4) 1557.
[3] McCusker L. B., Baerlocher C., Wilson S. T. and Broach R. W. *J. Phys. Chem. C* **2009** (113) 9838-9844.
[4] Marcus B. K. and Lok B. M. *Zeolite LZ-135 and process for preparing same*. 4,857,288, U. S. P. Office **1989**.
[5] Ciric J. *Crystalline Zeolite ZSM-10*. 3,692,470, U. S. P. Office **1972**.
[6] Wempe M. F. *J. Mol. Struct.* **2001** (562) 63-78.

General conclusion

At the end of my three years research path, devoted to the investigation of the catalytic formation of C-N bonds between organic molecules at the surface of silica and titania nanoparticles, I can propose my work contributed to the elucidation of the following scientific aspects:

- the amide bond formation from non-activated carboxylic groups and amino moieties occurs at the surface of silica via a hybrid catalytic site, specifically formed on silanols pairs ca. 5 Å apart. These pairs are present at the surface of amorphous silica and may be easily formed also at the surface of α-quartz materials;

- the occurrence of amino acids oligomerization at the surface of both crystalline and amorphous silica confirms that this latter can be effectively considered as a model material for the investigation of reactions of organic molecules at the surface of minerals in prebiotic scenarios;

- the catalytic formation of long peptide oligomers at the surface of anatase titania particles does not requires surface sites with peculiar coordinative, and then electronic, states but occurs on sites exposed by the most stable (101) surfaces, which are typically the most abundant, thus favouring the probability of the occurrence of this reaction;

- when considering the interaction between carboxylic groups and titania anatase (101) surfaces at ambient temperature, a new aspect can be considered: the absorption is neither fully molecular or dissociative, but the proton shuttles between the surface and the organic moiety;

- in the case of the amide bond formation from carboxylic acids and amines at the titania anatase (101) surface, a Eley-Rideal mechanism, rather than a Langmuir-Hinshelwood one, might be considered;

- the absorption of amino acids via chemical vapour deposition on titania nanoparticles can be exploited also for forming hetero-peptides. The production of Ser-His dipeptide allowed to contribute to the debate about the effective lytic activity of this dimer: the results obtained provide evidence of this activity at least towards a very simple oligopeptide;

- the formation of the zeolite MOZ framework is typically a looser in the competition towards the production of other types of microporous crystalline structures. Its way to the success should pass through the maintenance of a quite low temperature, accepting the consequent slow-down of the process kinetics.

Publications and submitted manuscripts

Published

- M. Fabbiani, M. Pazzi, M. Vincenti, G. Tabacchi, E. Fois, G. Martra
"Does the abiotic formation of oligoperptides on TiO2 nanoparticles requires special catalytic sites? Apparently not"
J. Nanosci. Nanotechnol. 2018 doi: 10.1166/jnn.2018.15385

- M. Fabbiani, E. Rebba, M. Pazzi, M. Vincenti, E. Fois, G. Martra
"Solvent free synthesis of Ser-His dipeptide from non-activated amino acids and its potential function as organocatalyst"
Res. Chem. Intermed. 2017 doi: 10.1007/s11164-017-3198-7

Submitted

- M. Fabbiani, C. Deiana, G. Martra, G. Tabacchi and E. Fois
"Temperature dependency of Brønsted basicity of TiO2 anatase {101} surfaces revealed by formic acid adsorption", submitted to J. Phys. Chem.

- M. Fabbiani, A. Rimola, M. Sodupe, P. Ugliengo and G. Martra
"How does silica catalyse the amide bond formation? Role of hybrid sites based on specific surface silanol pairs", submitted to ACS Catalysis.

Book edited

M. Fabbiani, L. Mino, C. Negri (editors)
"NANOSCIENCE meets METROLOGY: Synthesis, Characterization, Testing and Applications of Validated Nanoparticles" Book of Abstracts © 2016 (Politeko Ed.–Torino) ISBN: 978-88-87380-60-6